

# Development of 3D two-photon acousto-optical measurement methods for neuroscience studies

PhD thesis

Szalay Gergely

Semmelweis University  
Szentágothai János Doctoral School



Supervisor: Dr. Rózsa Balázs, M.D., Ph.D.

Official reviewers: Dr. Szabadics János, Ph.D.  
Dr. Kis Petik Katalin, Ph.D.

Head of the Final Ex. Committee: Dr. Kellermayer Miklós, M.D., DSc  
Members of the Final Ex. Committee: Dr. Tretter László, M.D., DSc  
Dr. Ulbert István, M.D., DSc

Budapest  
2018

# 1 CONTENT

---

|          |   |           |
|----------|---|-----------|
| <b>1</b> | <b>CONTENT</b> .....  | <b>2</b>  |
| <b>2</b> | <b>ABBREVIATIONS</b> .....                                  | <b>5</b>  |
| <b>3</b> | <b>INTRODUCTION</b> .....                                   | <b>6</b>  |
| 3.1      | WHY DO WE NEED TO MEASURE NEURONAL ACTIVITY IN 3D? .....    | 6         |
| 3.1.1    | <i>Detecting activity with light</i> .....                  | 6         |
| 3.1.2    | <i>Two-photon excitation</i> .....                          | 7         |
| 3.2      | 3D ACOUSTO-OPTICAL MICROSCOPY .....                         | 10        |
| 3.2.1    | <i>Acousto-optical deflection</i> .....                     | 10        |
| 3.2.2    | <i>Acousto-optical focusing</i> .....                       | 11        |
| 3.2.3    | <i>3D scanning configurations</i> .....                     | 11        |
| 3.2.4    | <i>The 3D-AO microscope</i> .....                           | 13        |
| 3.3      | NOVEL GENETIC TOOLS FOR DETECTING $Ca^{2+}$ IN NEURONS..... | 14        |
| 3.3.1    | <i>GCaMP6 sensor</i> .....                                  | 14        |
| 3.3.2    | <i>Increased imaging depth with GCaMP6</i> .....            | 15        |
| 3.4      | RANDOM-ACCESS 3D ACOUSTO-OPTICAL SCANNING .....             | 17        |
| 3.4.1    | <i>In vivo demonstration of 3D imaging</i> .....            | 19        |
| 3.4.2    | <i>Movement artifacts</i> .....                             | 20        |
| <b>4</b> | <b>AIMS</b> .....   | <b>22</b> |
| <b>5</b> | <b>METHODS</b> .....  | <b>25</b> |
| 5.1.1    | <i>Mice</i> .....   | 25        |
| 5.1.2    | <i>Slice preparation and electrophysiology</i> .....        | 25        |
| 5.1.3    | <i>Intrinsic imaging</i> .....                              | 26        |
| 5.1.4    | <i>AAV vector injection</i> .....                           | 27        |
| 5.1.5    | <i>Surgical procedure</i> .....                             | 27        |
| 5.1.6    | <i>Visual stimulation</i> .....                             | 28        |
| 5.1.7    | <i>Virtual reality environment</i> .....                    | 29        |
| 5.1.8    | <i>In vivo electrophysiology</i> .....                      | 30        |
| 5.1.9    | <i>Data processing</i> .....                                | 30        |
| <b>6</b> | <b>RESULTS</b> .....  | <b>31</b> |
| 6.1      | THE NEW AO SCANNING SYSTEM .....                            | 31        |
| 6.2      | DISPERSION COMPENSATION.....                                | 36        |
| 6.2.1    | <i>Material dispersion compensation</i> .....               | 36        |

|          |   |            |
|----------|---|------------|
| 6.2.2    | <i>Calculating material dispersion introduced by the optical pathway</i>                              | 37         |
| 6.2.3    | <i>Determining prism compressor axis lengths</i>  | 39         |
| 6.2.4    | <i>Angular dispersion compensation</i>  | 43         |
| 6.3      | INCREASED TRANSMITTANCE EFFICACY AND SCANNING VOLUME AT LONG WAVELENGTHS                              | 46         |
| 6.4      | CONTINUOUS 3D TRAJECTORY SCANNING WITH AO DEFLECTORS  | 51         |
| 6.4.1    | <i>Moving the focal spot in 2D</i>  | 53         |
| 6.4.2    | <i>Moving the focal spot in 3D</i>  | 56         |
| 6.4.3    | <i>Fast 3D DRIFT AO microscopy</i>  | 59         |
| 6.5      | CORRECTION FOR THE MOTION INSTABILITIES   | 64         |
| 6.5.1    | <i>Beam stabilization</i>   | 64         |
| 6.5.2    | <i>Automatic drift compensation algorithm</i>   | 65         |
| 6.5.3    | <i>Offline motion correction using AO DRIFT scanning</i>  | 68         |
| 6.6      | SCANNING METHODS FOR MOTION CORRECTION  | 69         |
| 6.6.1    | <i>3D ribbon scanning to compensate in vivo motion artifacts</i>                                      | 69         |
| 6.6.2    | <i>Recording of spiny dendritic segments with multiple 3D ribbon scanning</i>                         | 70         |
| 6.6.3    | <i>Multi-layer, multi-frame imaging of neuronal networks: chessboard scanning</i>                     | 74         |
| 6.6.4    | <i>Multi-layer, multi-frame imaging of long neuronal processes</i>                                    | 75         |
| 6.6.5    | <i>Volume scanning with snake scanning and multi-cube</i>   | 78         |
| 6.6.6    | <i>Multi-3D line scanning</i>   | 81         |
| 6.6.7    | <i>Advantage of the different scanning modes</i>  | 82         |
| 6.6.8    | <i>Motion correction in 3D</i>  | 83         |
| 6.6.9    | <i>Simulation of the quality increment with drift scanning</i>  | 86         |
| 6.6.10   | <i>Validation of the fast 3D motion-detection method and recording brain movement</i>                 | 91         |
| 6.6.11   | <i>Single action potential measurement</i>  | 94         |
| 6.7      | RANDOM EQUIVALENT-TIME SAMPLING, SELECTION OF THE FLUORESCENT DYE                                     | 98         |
| 6.7.1    | <i>Spatial distance estimate corresponding to the highest temporal resolution in bAP measurements</i> | 101        |
| 6.7.2    | <i>Theoretical calculation of the maximal temporal resolution</i>                                     | 103        |
| <b>7</b> | <b>CONCLUSION</b>   | <b>106</b> |
| 7.1      | BENEFITS OF THE NEW 3D METHODS IN NEUROSCIENCE  | 107        |
| 7.2      | IMAGING BRAIN ACTIVITY DURING MOTION  | 108        |
| 7.3      | COMPENSATION OF MOVEMENT OF THE BRAIN   | 109        |
| 7.4      | SIMULTANEOUS 3D IMAGING OF APICAL AND BASAL DENDRITIC ARBOR   | 110        |
| 7.5      | DEEP IMAGING  | 110        |

|  |            |
|--|------------|
| CREDIT ASSIGNMENT .....                                  | 112        |
| <b>8 SUMMARY .....</b>                                   | <b>113</b> |
| <b>9 ÖSZEFoglalás .....</b>                              | <b>114</b> |
| <b>10 REFERENCES .....</b>                               | <b>115</b> |
| <b>11 REFERENCES BY THE AUTHOR.....</b>                  | <b>119</b> |
| <i>11.1.1 Publications connected to the Thesis .....</i> | <i>119</i> |
| <i>11.1.2 Other publications .....</i>                   | <i>119</i> |
| <b>12 ACKNOWLEDGEMENT .....</b>                          | <b>121</b> |

---

## 2 ABBREVIATIONS

---

3D – three dimensions

AAV – adeno-associated virus

ACSF – artificial cerebral fluid

AO – acousto-optics

AOD – acousto-optical deflector

AOM – acousto-optical modulator

AP – action potential

bAP – backpropagation action potential

CA1 - Region I of hippocampus proper

CW – continuous wave

EPSP – excitatory postsynaptic potential

FWHM – full width at half maximum

GCaMP - the fusion protein containing the calmodulin-binding domain from the myosin light chain kinase also called M13 peptide, the circularly permuted green fluorescent protein, and the calmodulin

GECI – genetically encoded calcium indicator

GDD – group delay dispersion

GFP – Green Fluorescent Protein

IPSP – inhibitory postsynaptic potential

LOTOS – low-power temporal oversampling

MRT - magnetic resonance tomography

NA – numerical aperture

OGB-1 – Oregon Green Bapta-1

OGR - Orvosi Géntechnológiai Részleg (KOKI)

PET - positron emission tomography

PMT – photomultiplier tube

PSF – point spread function

RF – radio frequency

ROI – region of interest

SD – standard deviation

SEM – standard error of mean

SNR – signal to noise ratio

TeO<sub>2</sub> – tellur-dioxide

TOD – third order dispersion

V1 – visual cortex 1

VR – virtual reality

VIP – vasoactive intestinal protein

## 3 INTRODUCTION

---

### *3.1 Why do we need to measure neuronal activity in 3D?*

To better understand neuronal computation fast readout of information flow and processing is essential since action potentials, dendritic integration, subthreshold EPSP and IPSP events all happen at the millisecond timescale. Moreover, neuronal diversity, layer specificity of information processing, area-wise specialization of neuronal mechanism, internally generated patterns, and dynamic network properties all suggest that fast recording is required not only from a single plane or point, but also at a level of large neuronal populations situated in large 3D volume<sup>1,2,3</sup>. In addition, coding and computation within neuronal networks are generated not only by the somatic integration domains, but also by highly non-linear dendritic integration centers, which in most cases remain hidden from somatic recordings<sup>4,5,6,7</sup>. Therefore, to get better insight in the details of these functions we need to simultaneously read out neural activity both at the population and single-cell levels, with sufficient spatial (in the  $\mu\text{m}$  range) and temporal (at the millisecond scale) resolution.

#### **3.1.1 Detecting activity with light**

Light microscopy has an important role in biological research since it unfolds the possibility to simultaneously investigate neuronal activity and morphology from living tissue with high spatial resolution, resolving not only cells and cells' firing rate, but also subcellular compartment and subthreshold activity. However, the optical resolution is limited by the wavelength of the emitted light (according to Abbe's rule) and does not rival that of electron microscopy, but the scope of electron microscopy is limited when observing living specimens<sup>8</sup>. Other vital imaging technologies, such as MRT (magnetic resonance tomography), PET (positron emission tomography) or X-rays, can neither resolve subcellular structures nor can provide the exquisite molecular selectivity that would allow single molecules to be detected with billions of others in the background<sup>9,10</sup>.

During the past decade several new optical methods have been developed for fast readout of neuronal network activity in 3D. For example, it is possible to record 3D structures using spatial light modulators<sup>11</sup>, liquid lenses<sup>12</sup>, acousto-optical (AO)

deflectors<sup>13,2,14</sup>, temporal multiplexing<sup>15</sup>, axicon or planar illumination-based imaging<sup>16</sup>, fast z-scanning based on an axially moving mirror<sup>17</sup>, piezo actuators<sup>2,18</sup>, simultaneous multi-view light sheet microscopy<sup>19</sup>, two-photon light sheet microscopy<sup>20</sup>, optical fibers addressed by AO deflectors<sup>21</sup>, light field microscopy<sup>22</sup>, phase-locked ultrasound lens<sup>23</sup>, or phase mask combined with holographic illumination<sup>24</sup>.

Light microscopy inside living tissues is hampered by the degradation of resolution and contrast, caused by absorption and light scattering, which appear in a varying degree in every tissue, due to refractive index inhomogeneity. The deeper we image in the tissue, images become more degraded and high-resolution imaging eventually becomes impossible. A major step towards overcoming this problem was the invention of confocal microscopy<sup>25,26</sup>. In a confocal microscope, the illumination light is focused on a diffraction-limited spot, and this excites the sample along two cones close to the aimed focal point. Then, using the same objective, the emitted signal photons are focused onto a detector pinhole that rejects all light emitted outside of the focus spot.

### **3.1.2 Two-photon excitation**

The main drawback of confocal microscopy is its wasteful use of both excitation and emission. On one hand, absorption occurs throughout the specimen, but information is obtained only from a small sub-volume around the focal point. On the other hand, light that is scattered by the tissue, even if it is emitted from the focal point, is also rejected by the pinhole: this means that tissue scattering has a significant impact on the signal-to-noise ratio (SNR) of the images. This is particularly a major problem for *in vivo* fluorescence microscopy, where the limiting factors are usually either photochemical destruction of the fluorophore (photobleaching) or photodynamic damage to the specimen (photodamage)<sup>35</sup>. In confocal microscopy, only ballistic photons that are not scattered on their path out of the tissue contribute to the signal, while scattered photons, often the majority, are rejected by the detector aperture, limiting depth penetration of the technology to about 50-80  $\mu\text{m}$  in brain tissue. Excitation needs to be increased in order to compensate for this signal loss, which further intensifies photobleaching and photodamage<sup>35</sup>. These problems are common to many other, so-called single photon excitation technologies, among them the spinning-disc confocal<sup>27</sup> and light sheet

microscope technologies<sup>19</sup>. Theoretically, these problems can be handled by the use of laser scanning microscopy in combination with two-photon excitation<sup>19,28</sup>.

The concept of two-photon excitation is based on the idea that two photons of low energy can be combined in the same quantum event, resulting in the emission of a fluorescence photon at a higher energy than either one of the two excitatory photons. The probability of such absorption is extremely low, its cross section is proportional to the square of the photon flux, making it possible to counterbalance this low initial cross section by using extremely high photon fluxes. Multi-photon absorption is often called nonlinear because the absorption rate is dependent on a higher-than-first-power light intensity. Such high fluxes are only present in the focus of a high numerical aperture lens illuminated by a strong, pulsed near-infrared laser. The possibility of absorbing more than one photon during a single quantum event had been predicted more than 80 years ago by Maria Goeppert-Mayer<sup>29</sup>, but it was confirmed experimentally only after the invention of mode-locked lasers with a pulse duration below 1 ps and repetition rates of about 100 MHz. This made two-photon laser scanning microscopy feasible in practice<sup>30</sup>.

Mode-locking a Ti:sapphire laser, for example, boosts the two-photon excitation rate by 100,000-fold, compared to continuous-wave (CW) laser operation with the same average power (since its light pulses or packages present only in the 100,000th part of the whole imaging time). This quadratic dependence of the absorption rate on the light intensity gives two-photon microscopy its optical sectioning property because fluorescence is only generated in the vicinity of the geometrical focus where the light intensity is high. While scanning the laser focus in both lateral directions (x and y), fluorescence excitation is limited to the focal plane. No detector pinhole is necessary since – in most cases – no fluorescence is generated outside the focal volume, and all fluorescence photons, whether leaving the sample on scattered or ballistic trajectories, constitute useful signal.

The combination of low phototoxicity is enabled by the single point excitation and the efficient use of fluorescence – even scattered photons can be detected – which makes single-point two-photon microscopy a unique tool for observing function deep within tissue, even resolving structures deeper than one millimeter in brain tissue<sup>31,32,33</sup>. Its main drawback, however, its lower acquisition speed when compared to camera-based

approaches where, instead of the ‘single-channel’, or single point photomultipliers (PMTs), information can potentially be collected from millions of camera pixels simultaneously.

From the technologies listed above only a handful can provide single-point multi-photon excitation in three dimensions that allows whole-field detection of the scattered fluorescence photons required for deep brain imaging<sup>31</sup>. Furthermore, among the available 3D scanning solutions for multi-photon microscopy, only 3D AO scanning is capable of performing 3D random-access point scanning<sup>2,14,34</sup> to increase the measurement speed and signal collection efficiency by several orders of magnitude in comparison to classical raster scanning. This is because the pre-selected regions of interest (ROIs) can be precisely and rapidly targeted without wasting measurement time on unnecessary background areas whereas 3D AO technology enables freely “jump” the focus of the laser between these ROIs within microseconds.

### 3.2 3D acousto-optical microscopy

The 3D acousto-optical (3D-AO) microscopes, presented in the literature, possess different optical design and different performance, with their advantages and limitations. However, every design is based on the same physical principles, on the acousto-optical effect generated in reciprocal crystal.

The phrase “acousto-optic” refers to the field of optics that studies the interaction between sound and light waves. In the field of fluorescent imaging we use acousto-optical devices to diffract laser beams through ultrasonic gratings. The acousto-optical effect is based on a periodic change of the refractive index in a high refractive index medium (usually tellurium dioxide,  $\text{TeO}_2$ ) which is the result of the sound wave induced pressure fluctuation in the crystal. This grating diffracts the light beam just like a normal optical grating, but here the gradient can be rapidly adjusted by changing the driving signal.<sup>35</sup>

#### 3.2.1 Acousto-optical deflection

Acousto-optical deflectors (AODs) control the optical beam spatially, they use ultrasonic waves to diffract the laser beam depending on the acoustic frequency. If we introduce a sine wave at the piezoelectric driver, it will generate an optical deflection in the acousto-optic medium according to the following equation:<sup>35</sup>

$$\Delta\theta_d = \frac{\lambda}{v} \Delta f \quad (\text{Equation 1})$$

where  $\lambda$  is the wavelength of the optical beam,  $v$  is the velocity of the acoustic wave, and  $\Delta f$  is the change in the sound frequency (**Figure 1**).

In practice, AODs or acousto-optical modulators (AOMs) are used. AOMs modulate only the amplitude of the sound waves, while AODs are able to adjust both the amplitude and frequency.

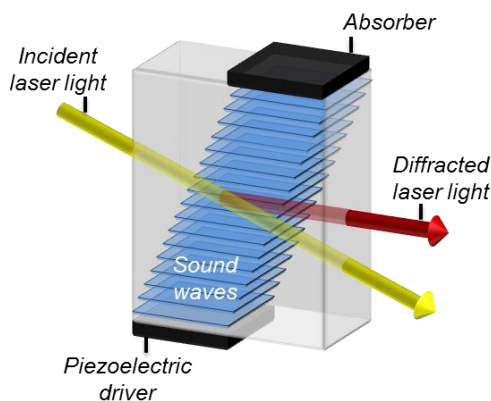


**Figure 1. Operating principle of acousto-optical deflectors.** A piezoelectric driver elicits radio frequency (RF) sound waves due to the externally applied sinusoidal voltage. Sound enters and traverses through the diffracting ( $\text{TeO}_2$ ) medium while interacting with light throughout the aperture. Light is diffracted on the sound wave's refractive index changes as on a steady optical grating providing diffracted light beams whose angle is dependent on the sound wave's frequency.

### 3.2.2 Acousto-optical focusing

Besides deflection, AODs can also be used for fast focal plane shifting<sup>2,14,34,36</sup>. If the frequency of the acoustic wave that fills up the crystal is changing linearly in time, (thus the frequency is chirp), then at a given point in the crystal the optical gradient increases as a function of time, so different portions of the optical beam are deflected in different directions (**Figure 2**). Thus focusing or defocusing effect occurs, depending on the frequency slope (sweep rate) of the chirped acoustic wave. The focal length of an acousto-optical lens ( $F$ ) can be calculated from the sweep rate as<sup>36</sup>:

$$F = \frac{v^2 T_{scan}}{2\lambda \Delta f} \quad (\text{Equation 2})$$

where  $\lambda$  is the optical wavelength of the beam,  $v$  is the velocity of the acoustic wave,  $\Delta f$  is the change of the sound frequency, and  $T_{scan}$  is the modulation rate of the sound frequency<sup>36</sup>.

To keep a stable focal distance, the frequency gradient should be preserved in the crystal. The frequency should therefore be continuously increased (or decreased) at the piezoelectric driver to preserve the focal distance. This will result in a lateral drift of the focal-point, which can be easily compensated by introducing a second acousto-optical deflector with a counter-propagating acousto-optical wave into the optical pathway<sup>36</sup>.

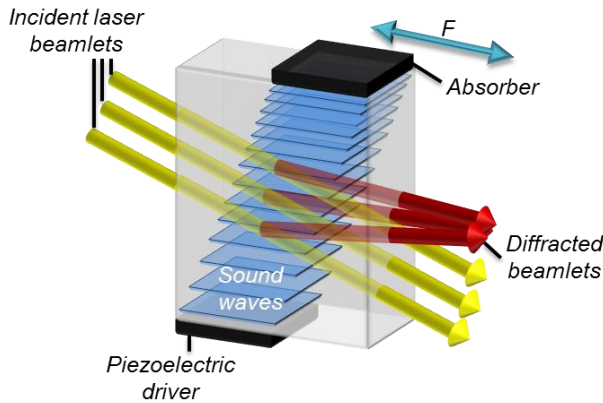


**Figure 2. Acousto-optical focusing.** AO deflector arrangement similar to **Figure 1**, but here the sound frequency is changing, resulting in a varying grating size along the propagation axis. As a consequence, different parts of the laser beam are diffracted with varying angles creating a focus point whose position can be changed by the parameters of the sound applied to the deflector. Red and yellow lines indicate diffracted and incident laser beams and  $F$  denotes focal distance.

### 3.2.3 3D scanning configurations

Combining four of these crystals can form a 3D focusing system. We need two orthogonal deflectors for X and Y scanning, a third one for Z focusing, and we need a

forth one to compensate for the drift caused by the Z focusing crystal. The four deflectors can be organized to a focusing system at several configurations (**Figure 3**).

We have designed the detailed optical model of these configurations to find the combinations of active and passive optical elements in the scanning light-path of the microscope, which would provide the maximal exploitation of the apertures of all lenses at different X, Y and Z scanning positions, and therefore result in the smallest PSF in the largest possible scanning range.

The model suggested a new design concept. The largest scanning volume can be reached by grouping the deflectors into two functionally distinct groups which are coupled by one afocal projection (**Figure 4**).

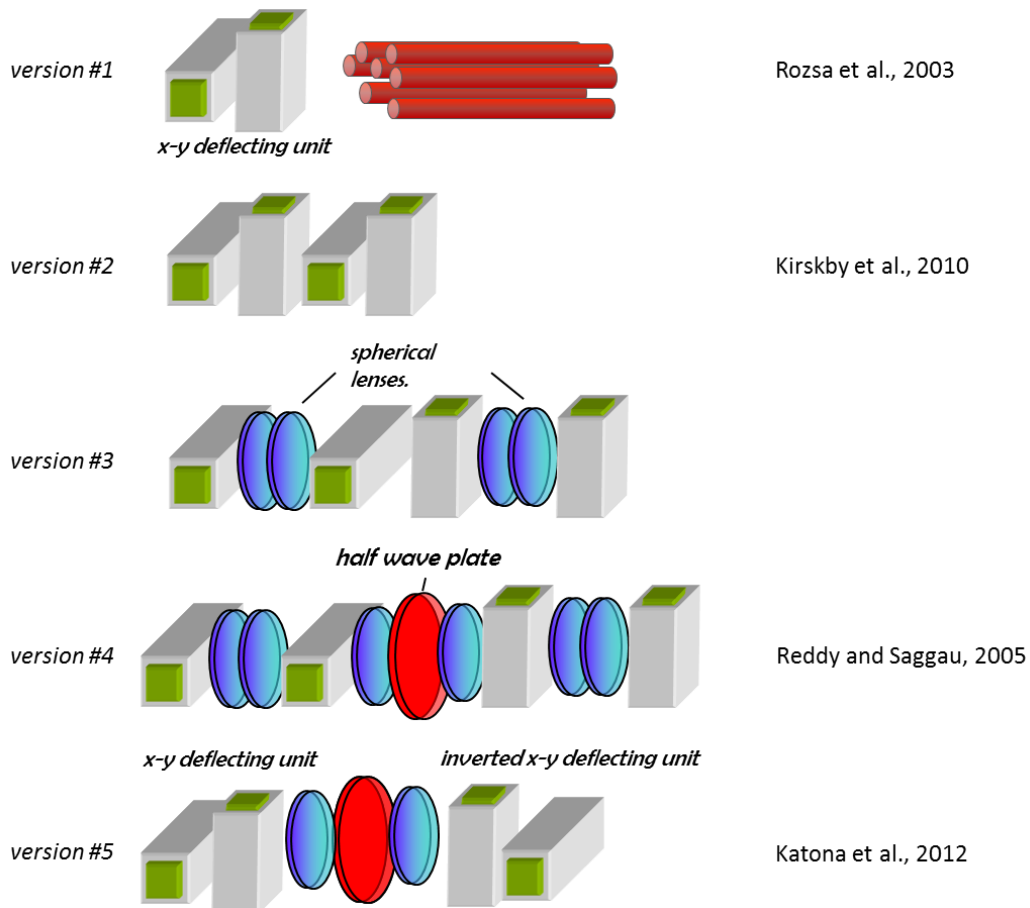


**Figure 3. Different 3D AO scanning arrangements.** Version #1 uses optical fibers to position the excitation beam in 3D<sup>21</sup>, however it has been difficult to implement this version due to the requirement of many mechanical devices positioning the fibers. Versions #2-5 were analyzed by modeling and Version #5 was found the most beneficial to implement<sup>2</sup>. Version #2<sup>14,37</sup> and Version #4<sup>13,34,38,39</sup> have been described by other laboratories and have recently been used for functional measurements<sup>13,34</sup> but – according to our expectation from optical modeling – they have lower specifications than our solution.

### 3.2.4 The 3D-AO microscope

**Figure 4** shows the schematic of the earlier version of the 3D-AO microscope used in our lab (see more details in Katona et al. 2012). Briefly, laser pulses were provided by a femtosecond laser source. The beam was extended to 15 mm by a Galilean telescope in order to fill the large aperture of the acousto-optical deflectors. Z-focusing and lateral scanning were achieved by two separate pairs of acousto-optical deflectors which were coupled by two achromatic lenses ( $f = 200$  mm). Finally, the light was coupled to an upright two-photon microscope (Femto2D, Femtonics Ltd.) using a telecentric relay consisting of an  $f = 250$  mm and a  $f = 210$  mm lens (Thorlabs). The excitation was delivered to the sample, and the fluorescent signal was collected, using an Olympus 20 $\times$ , NA 1.0 objective and then separated using a dichroic mirror (700dcxru, Chroma Technology). The separated fluorescence was delivered to GaAsP photomultipliers fixed on the objective arm, short focal distance lenses were used the focus to light to the detectors surface. During *in vitro* measurements the fluorescence photons propagating opposite to the objective were also captured by similar photomultipliers mounted below the condenser lens in order to enhance the collection efficiency of the scattered photons.

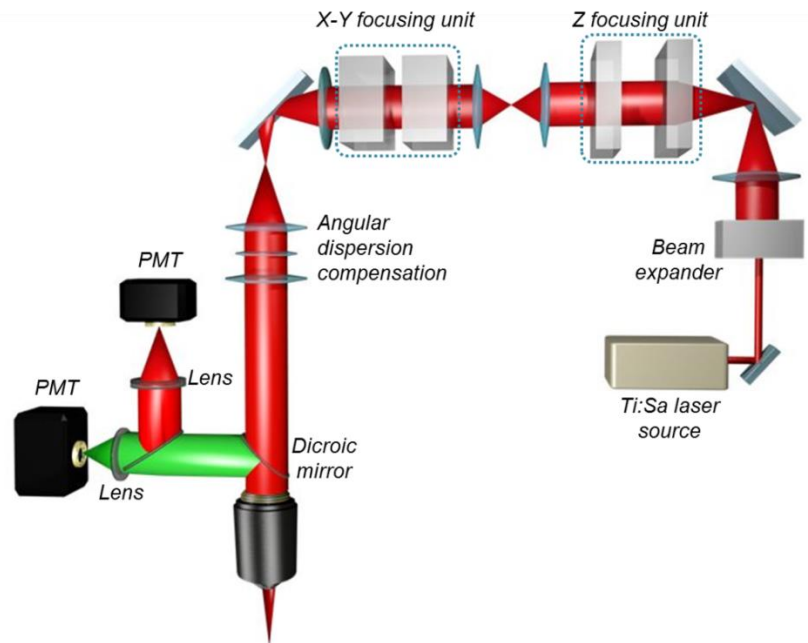


**Figure 4. Simplified optical path of the 3D-AO microscope** – The first pair of acousto-optical crystals were used for X,Y scanning while the second pair for Z-focusing. Angular dispersion was compensated for better optical resolution through the whole field of view. Described in more detail in Katona et al. 2012; Szalay et al. 2016.

### 3.3 *Novel genetic tools for detecting Ca<sup>2+</sup> in neurons*

#### 3.3.1 **GCaMP6 sensor**

Besides a fast and reliable scanning method the other pillar of functional anatomy is an adequate labeling technique which makes biological activity visible for fluorescent microscopy. Regenerative neuronal events are coupled with the flux of several ions, including sodium, potassium, calcium and in some cases chloride or other ions. However the absolute concentration is larger for sodium or potassium the relative change is much larger, in the order of magnitude, for calcium. Therefore in the literature activity sensitive dyes, almost exclusively, are designed to be coupled with calcium concentration change. That is why intracellular calcium indicators will indicate activity, and calcium concentration increase with increase of excitable molecule. This change can be followed for example with two-photon microscopy, but also with other techniques.

Fluorescent calcium sensors can be synthetic dyes or protein based molecules. Using structure-based mutagenesis and neuron-based screening a new family of ultrasensitive protein calcium sensors (GCaMP6) was developed that outperformed other sensors in cultured neurons, zebrafish, flies and also in mice *in vivo*<sup>40</sup>. With GCaMP6 sensor, under ideal circumstances, even detection of single action potentials in neuronal somata or in individual dendritic segments<sup>15</sup> is feasible from layer 2/3 pyramidal neurons of the mouse visual cortex. Thus this sensor provides new insight into the organization and dynamics of neural circuits over multiple spatial and temporal scales<sup>40</sup>.

According to Chen et. al 2013, supported by our own experience (**Figure 5**), the GCaMP sensor have maintained signal levels compared to bulk loaded AM dies. Beside this maintained signal level, GCaMP6 labeling has several other advantages:

- (i) Labeling is more stable over long timescales. Since uptake and clearance of synthetic dies occur on a much faster time scale, over hours, baseline fluorescence level can change over a long measurement day. Therefore, it is impossible to perform several days or weeks long measurements with this die, while viral labeling can be stable even for months, without no or modest change in the baseline fluorescence level<sup>41</sup>. This allows longer experimental

protocols, raising the possibility to combine this measurement with behavioral protocols.

- (ii) With the combination of different promoters, it allows simultaneous measurement of spines and somata from several cells<sup>40</sup>.
- (iii) Most importantly, since it is a genetic method we can selectively label different cell types.
- (iv) Allows deeper imaging from the tissue.

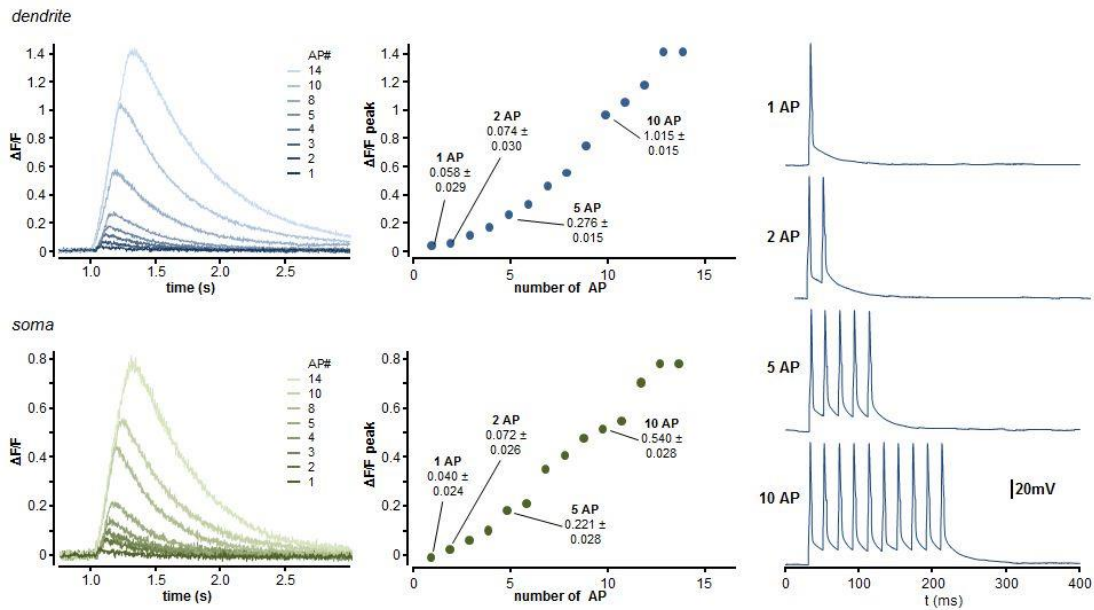


**Figure 5. Calcium responses from GCaMP6f labeled animals.**  $Ca^{2+}$  responses are measured from whole cell patch clamped CA1 pyramidal cell in vitro. Cells were labeled with GCaMP6f with AAV viral injections. bAPs were induced by voltage injections through the patch pipette. Fluorescent signal measured on the somata or on a 50-100  $\mu$ m segment of the apical dendrite. (Right) Measured fluorescent transients for 1, 2, 3, 4, 5, 8, 10 and 14 action potentials shown as  $\Delta F$  over  $F$ . (Middle) Average maximums from the transients in the Left. (Right) Representative electrophysiology data, shown for 1, 2, 5 and 10 action potentials. For all measurements AP frequency was 20Hz.

### 3.3.2 Increased imaging depth with GCaMP6

Deep imaging within the tissue can help us to measure larger portion of the neuronal network under investigation. The increased scanning depth is resulted by the fact that this genetically encoded calcium indicator can be emitted at longer wavelength compared to the previously used most popular synthetic dyes (850-960 nm for GCaMP family compared to 780-850 nm for synthetic dies such as OGB-1, Fluo-4 or Fluo-5F). This difference enables measuring deeper from the tissue, as imaging depth during two-

photon measurements determined is mainly by the emission spectra. This is the result of the absorption properties of living tissue, since during two-photon imaging excitation wavelength falls to the near infrared range, where biological tissue is mostly transparent; however, emission spectra falls in the visible range, thus much more influenced by re-absorption, diffusion and scattering caused by the tissue.

**Figure 6** shows the wavelength dependent imaging depth where I pulled data from all measurement I performed in vivo during this work. Imaging depth was defined as the Z-range of the imaging point during the experiment. Obviously, this representation does not take several parameters into account, such as surgery quality, cranial window size, number of blood vessels in the imaging field, optical resolution, dye concentration, which can all influence imaging depth during two-photon imaging. Still the tendency shown on **Figure 6** supports the idea that by developing dyes with longer wavelength can help image deeper in the tissue. This idea is also demonstrated by three-photon imaging where the emission wavelength is even longer (in the 1500 nm range) and can reach imaging depth of 1200  $\mu\text{m}$ <sup>42</sup>.

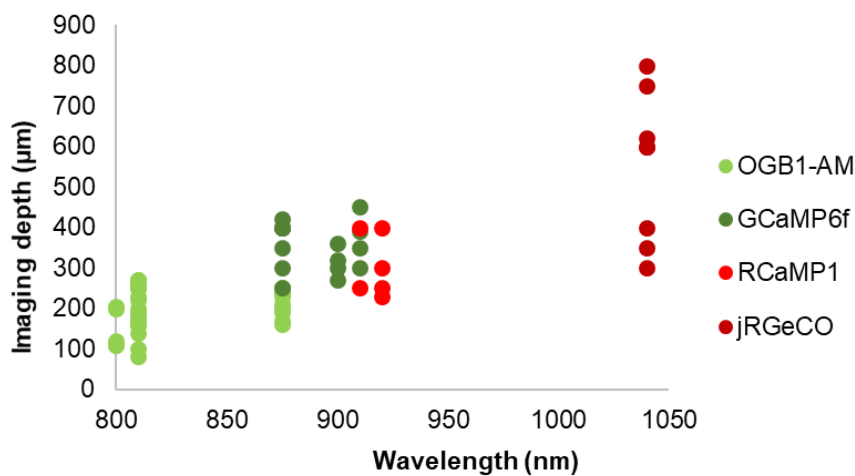


**Figure 6. Wavelength dependent imaging depth.** Data is pulled from all in vivo measurements I have performed during the work for this thesis. Each data point indicates a single measurement. The imaging depth indicated the Z-range of measurement points during the given experiment. I only include those measurements where the imaging data was used for the analysis of a given biological project, thus the one which are “good enough” for biological measurement, to minimize the effect of the surgery, bone regrown or other non-correlated parameters. Light green points show OGB-AM, dark green GCaMP6f, light red RCaMP1 while dark red jRGECO measurements.

### 3.4 Radom-access 3D acousto-optical scanning

To demonstrate imaging performance of 3D point scanning I have imaged backpropagating action potential (bAP) at several dendritic sites. I patch-clamped a CA1 pyramidal cells in whole-cell mode in an acute hippocampal mouse brain slices and filled the cells with the green fluorescent  $\text{Ca}^{2+}$  sensor Fluo-5F and the red fluorescent marker Alexa594. On the example presented on **Figure 7** propagating activity was measured at seventy-seven 3D locations of a single hippocampal neuron.

The objective was positioned at a depth such that the center of the region of interest was in focus. The objective was fixed at this position and a reference  $z$ -stack of images was acquired using 3D AO scanning only (**Figure 7**), then measurement points were selected along the dendritic tree. The cell was held in current-clamp mode and an AP was evoked by somatic current injection while near-simultaneously measuring dendritic  $\text{Ca}^{2+}$  signals associated with the bAPs by repetitively scanning the selected 3D coordinates with 29.76 kHz. When sample drift occurred, I've repositioned single points or the entire group manually.

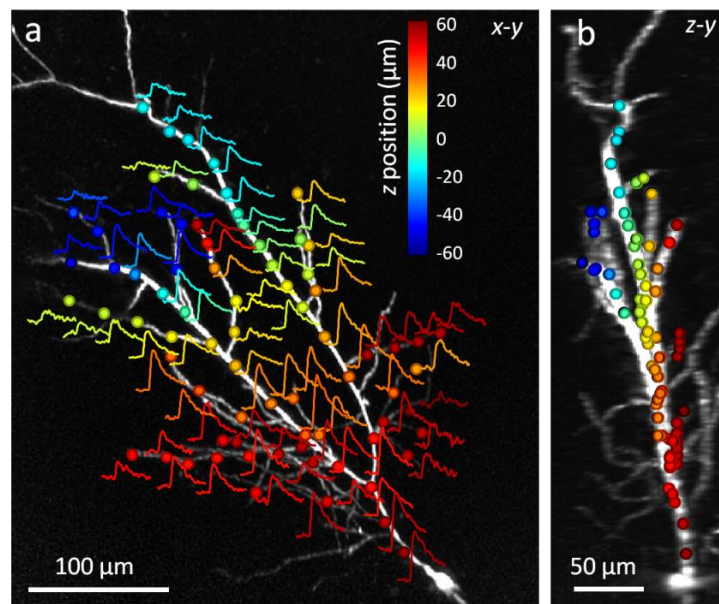


**Figure 7. Three-dimensional measurement of bAPs.** (a) Maximum intensity  $z$ -projection of the dendritic arbor of a CA1 pyramidal cell imaged with 3D AO scanning. Circles represent the 77 pre-selected measurement locations for 3D random access point scanning. Overlaid curves show  $\text{Ca}^{2+}$  transients recorded near-simultaneously in each location induced by a single bAP (each average of five traces). The repetition rate of the measurement was 29.76 kHz (0.39 kHz speed in each location). The  $z$  coordinates of the measurement locations are color-coded. (b) Maximum intensity side projection of the cell with the measurement locations shown in a.

Since the acute brain slices were 300  $\mu\text{m}$  thick, only a fraction of the total AO  $z$ -scanning range was used. To test random-access 3D AO scanning for a larger  $z$ -range I have record bAP-induced  $\text{Ca}^{2+}$  transients while moved the objective focal plane mechanically from + 562  $\mu\text{m}$  to - 546  $\mu\text{m}$  away from the  $z$ -center and used AO  $z$ -focusing to refocus the recorded dendritic tree (**Figure 8**). Independent of the AO  $z$ -settings, single bAPs could be resolved in  $\text{Ca}^{2+}$  transients induced by a train of three APs. Similarly, single bAPs could be followed in a 760  $\mu\text{m}$  lateral scanning range (**Figure 8b**). Thus a total of 1190  $\mu\text{m}$  AO  $z$ -focusing range and a 760  $\mu\text{m}$  AO lateral scanning range is shown with the 20 $\times$  objective where single APs can be resolved with SNR over 2. In summary, resolution of single AP-induced transients is possible in a near-cubic-millimeter scanning volume during in vitro conditions.

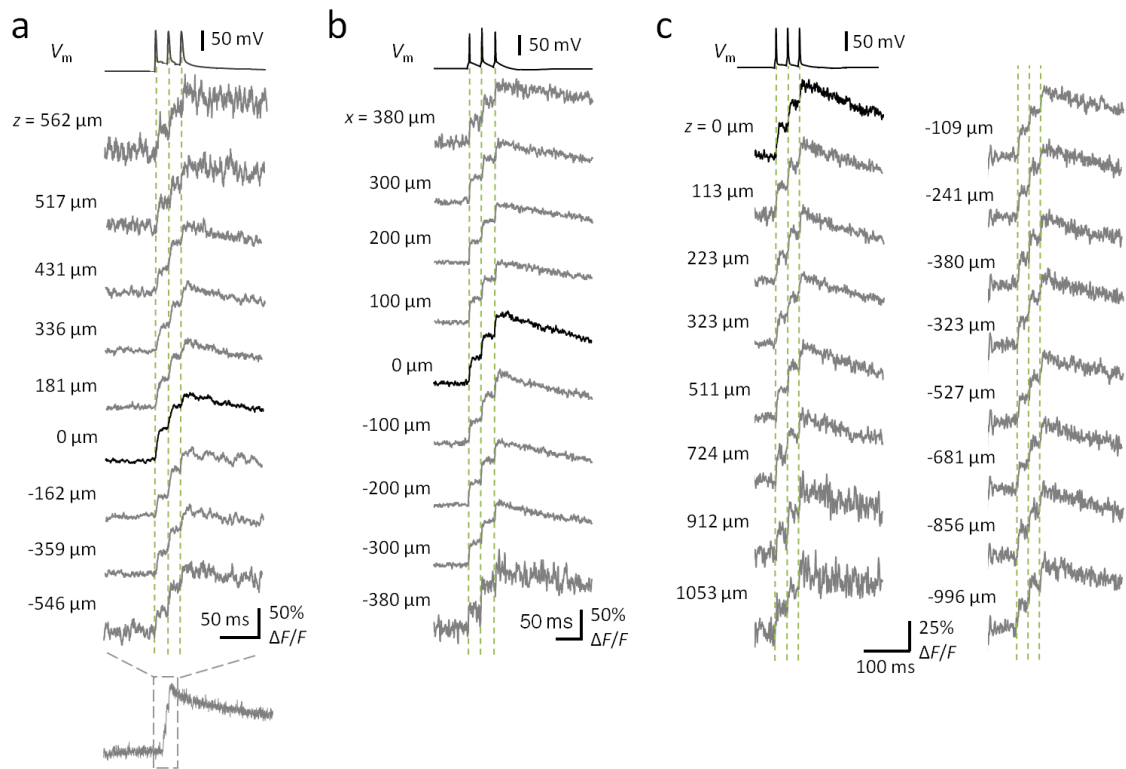


**Figure 8. Resolving bAPs at the sides of the FOV.** (a) Single traces of three bAP-induced dendritic  $\text{Ca}^{2+}$  transients measured at the same dendritic point at different AO  $z$ -focusing settings. To keep the image sharp, the AO  $z$ -focusing was compensated by mechanical refocusing of the objective. Note the preserved single AP resolution even at the lower and upper limits of the scanning range. Corresponding somatic voltage traces ( $V_m$ ) are shown on the top (b) The same as in c, but transients were recorded while shifting the dendrite along the  $x$  axis. (c) The same as in a, but single traces were recorded using the 16 $\times$  objective. Note that the AO  $z$ -focusing range with single AP detection level exceeds 2000  $\mu\text{m}$  (for in vitro conditions and in transparent sample).

### 3.4.1 In vivo demonstration of 3D imaging

To demonstrate 3D imaging also at *in vivo* circumstances, I've recorded  $\text{Ca}^{2+}$  responses from a population of individual neurons in the visual cortex of adult anesthetized mice. I've injected a mixture of OGB-1-AM to monitor changes in intracellular  $\text{Ca}^{2+}$  concentrations, and sulforhodamine-101 (SR-101)<sup>43</sup>, to selectively label glial cells (**Figure 9**). The red fluorescence of SR-101 allowed differentiation between neurons and glial cells (green and red). The maximal power of our laser (3.5 W at the laser output and  $\sim 180\text{mW}$  after the objective) limited the depth of the *in vivo* recording to a maximum of 500  $\mu\text{m}$  from the surface of the cortex (the total imaging volume was  $400\times 400\times 500\ \mu\text{m}$ ).

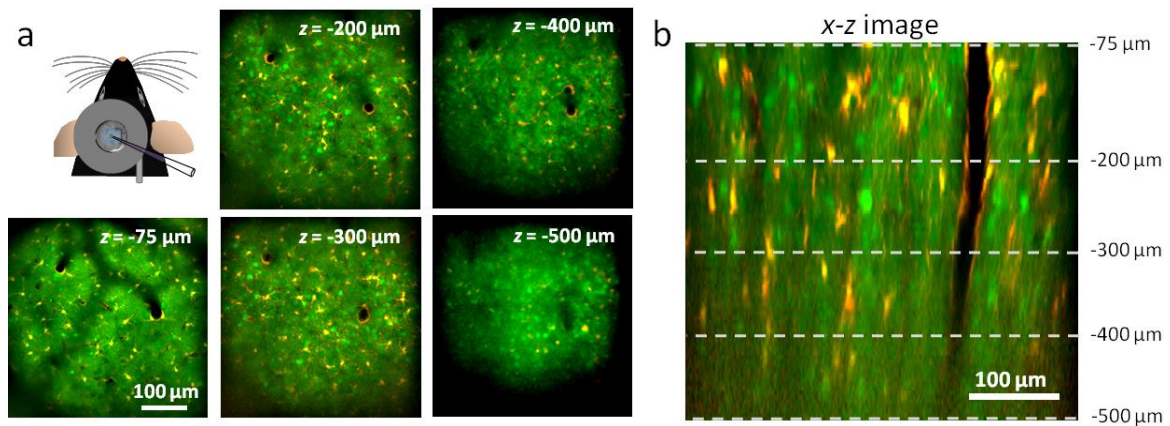


**Figure 9. In vivo image stacks of the neuronal population.** (a) Representative background-corrected images taken at different depths from the surface of the brain showing neurons (green) and glial cells (red and yellow). (upper left) Sketch of *in vivo* experimental arrangement. Staining by bolus loading (OGB-1-AM and SR-101) in mouse V1. (b) x-z slice taken from the middle of the stack volume. Dotted lines correspond to the planes in a.

Next, we recorded a reference  $z$ -stack and, either by using an automated algorithm, or manually, we identified the neuron and glial cell bodies. In the simple case when OGB1-AM and SR-101 dyes are bolus loaded into the animal, cells can be categorized according to their dye content measured by fluorescence, which is possible on multiple channels. In this case neuronal cells can be detected from their elevated green fluorescence and decreased red fluorescence. Centers of each neuronal cell body were used for random-access activity imaging (**Figure 10b**).

After the selection of the cell bodies, we recorded the activity of each neuron by scanning at 80 Hz and plotted the recorded raw and point-by-point background-

corrected and normalized fluorescence data in real-time, each row showing the activity of a single cell (**Figure 10c**). Responses of neurons could be resolved with high SNR (**Figure 10d**). The stability of long-term recording was monitored using the baseline fluorescence.

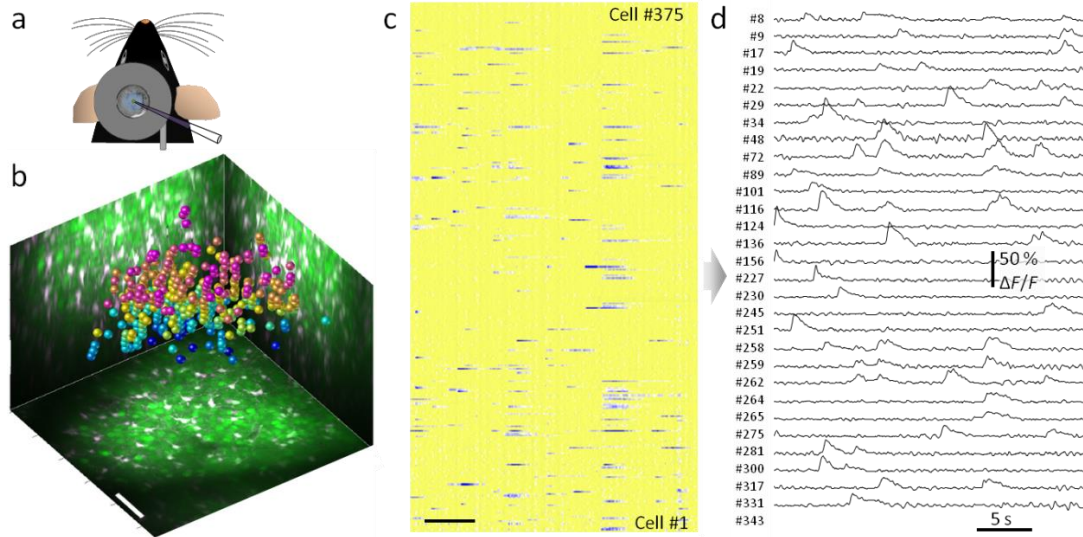


**Figure 10. Spontaneous neuronal network activity in vivo.** (a) Sketch of in vivo experimental arrangement. (b) Maximal intensity side- and z-projection image of the entire z-stack ( $280 \times 280 \times 230 \mu m^3$ ; bolus loading with OGB-1-AM and SR-101). Spheres represent 375 autodetected neuronal locations color coded by depth. Scale bars,  $50 \mu m$ . (c) Parallel 3D recording of spontaneous  $Ca^{2+}$  responses from the 375 locations. Rows, single cells measured in random-access scanning mode. Scale bar, 5 s. (d) Examples of  $Ca^{2+}$  transients showing active neurons in c.

### 3.4.2 Movement artifacts

Despite the evident benefits of the 3D point scanning, when we want to extend the scope of this scanning technique to behaving animal models, to measure a single point per neuronal structure will not be sufficient. Fluorescence information could be completely lost during motion in behaving animals when using the point scanning method (**Figure 11**).

To overcome this limitation we need to extend single scanning points to surface or volume elements in order to preserve the surrounding fluorescence information for motion artifact elimination.

The size of the surrounding area and temporal resolution of the measurement are working against each other, the proper extent is defined by the properties of the given

measurement. However measuring every point in the 3D volume needed for sufficient motion correction would increase temporal resolution to the second range, which not allows fast calcium measurement for burst or single action potential detection. This issue can be address by arbitrary 2D planes distributed in the 3D space, 3D AO technology is a great tool for the realization. The details of this method will be explained through this thesis.

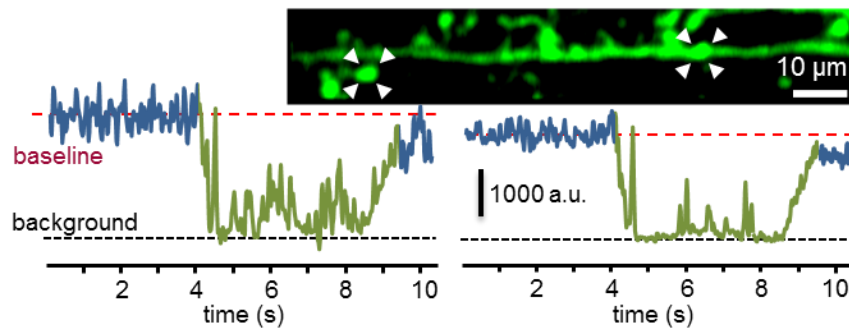


**Figure 11. Fluorescence information can be completely lost when using point-by-point scanning in the moving brain of behaving animals.** Exemplified dendritic and spine transients were recorded using 3D random-access point scanning during motion (green) and rest (blue) from one dendritic and one spine ROI, indicated with white triangles in the inset. Note that fluorescence information can reach the background level in a running period, indicating that single points are not sufficient to monitor activity in behaving animals.

## 4 AIMS

---

Despite the evident benefits of 3D random-access AO microscopy, the method faces some limitations when we would like to perform long term measurements from awake, behaving animals, where long term stability and redundancy for motion artefact have key importance. The aim of my work was to outline and address these emerging problems and design novel techniques and measurement strategies which provide stable and reliable image quality for behavioral studies during everyday use.

These issues to handle are the following:

- 1) **Dispersion compensation** – Acousto-optical crystals are composed of high refractive index material thus introducing large material dispersion. Short light pulses (around 100 fs for Ti:Sa lasers) traveling in high refractive index material are elongated significantly, that reduces two-photon efficiency. In our system with 72 000 fs<sup>2</sup> group delay dispersion (GDD) this effect would produce picosecond long pulses completely diminishing our two-photon signal during *in vivo* measurements. To compensate for this artifact, first we created the detailed optical model of the system containing all the optical elements and calculated the exact material dispersion produced by these components. Then we designed and built a four-prism compressor that fully aborts this error. Besides material dispersion AO crystals also introduce large angular dispersion caused by the spherical inhomogeneity of the AO crystals and other optical elements, which would produce position dependent elongation of the point spread function (PSF). At the edges of the imaging field the extent of this effect can be so large that, on one hand, resolution degrades so even somata cannot be resolved; on the other hand, laser intensity distributed in a larger focal volume would dramatically reduce quantum efficiency. To compensate for this, the exact properties of the angular dispersion were determined again from the optical model, and then fully compensated with a special lens introduced in the optical pathway.
- 2) **Increasing transmittance at longer wavelengths** – With the introduction of new genetic dies and sensors in neuroscience (for example GFP or genetically encoded calcium indicators, such as GCaMP6) the use of longer wavelengths became essential to effectively excite these molecules. Acousto-optical cells are highly

sensitive to the wavelength and this proportion is inverse. Since we are using four of these crystals in the optical pathway, the transmitted intensity drops dramatically when increasing wavelength. Changing the wavelength from 800 nm to 875 nm, without any additional compensation, would cause the transmittance to drop from 10% to around 1.5%, that is, even with the modern 2-3W femtosecond laser allowing only around 40mW imaging power, which is insufficient for *in vivo* measurement deep in the tissue. To overcome this limitation, we applied several optical and electronical developments in the microscope design, to achieve at least as high transmittance as previously with the shorter wavelength.

- 3) **AO Drift scanning** - Sampling rate is limited by the optical aperture of AO deflectors, which must be filled by an acoustic wave to address a given scanning point. In our system, with relatively large crystal length during 3D point-by-point scanning the switching time is relatively long (about 20-33  $\mu$ s), which limits either the measurement speed or the number of ROIs. If we are measuring from a behaving animals, therefore have to measure multiple points per cell or dendritic segment, to produce data for motion correction, with random access point scanning mode the sampling rate would drop to the 1-2 Hz range, which is insufficient to resolve fast  $\text{Ca}^{2+}$  events.

To resolve this problem we introduce a new scanning method, 3D DRIFT scanning, which increase the scanning rate 3-70 fold depending on the measurement paradigm.

- 4) **Motion artefact compensation** - It has been shown that neuronal signaling could be completely different in awake and behaving animals<sup>44,45,46</sup>. Nevertheless fluorescence data are lost or contaminated with large amplitude movement artifacts during *in vivo* recordings in behaving animals, this occurs because the actual location of the recorded ROIs is continuously changing during the measurements due to tissue movement caused by heartbeats, blood flow in nearby vessels, respiration, and physical motion<sup>47</sup>. This results in fluorescence artifacts because of the spatial inhomogeneity in the baseline fluorescence signal and in relative fluorescence changes. In addition, the amplitudes of motion-induced transients can even be larger than the ones induced by one or a few action potentials detected by genetically encoded calcium indicators (GECIs)<sup>40</sup>.

Therefore it is difficult to separate post-hoc the genuine fluorescence changes associated with neural activity from the artifacts caused by brain movement. To overcome this problem we used 3D DRIFT AO scanning, extending the pre-selected individual scanning points to small 3D lines, surfaces, or volume elements to cover not only the pre-selected ROIs but also the neighboring background areas or volume elements while maintaining the data sampling rate.

Volume or area images acquired with the methods developed allow motion artifact correction on a fine spatial scale and, hence, the *in vivo* measurement of fine structures in behaving animals. In this way, we can preserve fluorescence information from the pre-selected ROIs during 3D measurements even in the brain of behaving animals, while maintaining the 20-400 Hz sampling rate that is necessary to resolve neural activity at the individual ROIs.

Another source of artifact caused by mechanical instability is the waggle of the beam itself caused by the instability of the optical elements. Reliable microscope stability in the daily routine is a very important factor. Since the optical path of the acousto-optical microscope is more than 6 meters long and containing more than a hundred optical elements, most of them sensitive of temperature and humidity fluctuation, active stabilization of the beam was necessary. This was realized with the combination of quadrant detectors and motorized mirrors.

- 5) **Increased temporal resolution** – If we are interested in even faster  $\text{Ca}^{2+}$  events, such as fine properties of sharpe-wave ripples, local regenerative events or signal propagation along a dendritic arbor, the 20-400 Hz sampling rate of 3D AO point scanning can be still insufficient. This limitation can be overcome at some circumstances, for example, when we have the event repeated many times with very precise timing. Given these circumstances we were able to resolve sub-millisecond or even microsecond events and measure the propagation speed even along a 10-20  $\mu\text{m}$  segment of a dendritic branch.

## 5 METHODS

---

### 5.1.1 Mice

All experimental protocols were approved by the Animal Care and Experimentation Committee of the Institute of Experimental Medicine of the Hungarian Academy of Sciences (approval reference numbers PEI/001/194-4/2014 and PEI/001/1771-2/2015). All procedures complied with Hungarian and European regulations for animal research, as well as with the guidelines of Society for Neuroscience. The *in vivo* recordings from the primary visual cortex were performed on C57BI/6J, Thy1-Cre, vip/IRES-Cre mice (P60-120). Animals were allowed free access to food and water and were maintained in temperature-, humidity-, and light-controlled conditions. Transgenic lines were developed and bred at the Medical Gene-technological Unit (OGR) of the Institute of Experimental Medicine of the Hungarian Academy of Sciences.

### 5.1.2 Slice preparation and electrophysiology

Acute hippocampal slices were prepared from Thy1-Cre mice (injected with Cre dependent version of GCaMP6f vector) using isoflurane anesthesia followed by swift decapitation, in accordance with the Hungarian Act of Animal Care and Experimentation (1998; XXVIII, section 243/1998.). Horizontal (300-400  $\mu\text{m}$ ) brain slices were cut with a vibratome and stored at room temperature in artificial cerebrospinal fluid (ACSF) (in mM: 126 NaCl, 2.5 KCl, 2 CaCl<sub>2</sub>, 2 MgCl<sub>2</sub>, 1.25 NaH<sub>2</sub>PO<sub>4</sub>, 26 NaHCO<sub>3</sub>, and 10 glucose) as previously described<sup>2,5,6</sup>.

Hippocampal CA1 pyramidal cells were visualized using 900 nm infrared lateral illumination<sup>5</sup>. Current-clamp recordings were made at 23°C or 33°C (MultiClamp 700B, Digidata 1440: Molecular Devices; chamber heater: Luigs & Neumann; in-line heater: Supertech). For whole-cell current-clamp recordings, glass electrodes (6-9 M $\Omega$ ) were filled with (in mM): 125 K-gluconate, 20 KCl, 10 HEPES, 10 Di-Tris-salt phosphocreatine, 0.3 Na-GTP, 4 Mg-ATP, 10 NaCl. For fast-propagation speed measurements we added 0.2 mM Fluo-5F pentapotassium salt (Invitrogen) and 0.2 mM Alexa-594 (Invitrogen) to the pipette solution. For extracellular current-clamp recordings, glass electrodes (6-9 M $\Omega$ ) were filled with ACSF or with ACSF containing 1 M NaCl. All chemicals and drugs, unless otherwise noted, were purchased from

Sigma. Cells with a resting membrane potential more negative than  $-50$  mV were accepted.

Focal synaptic stimulation was performed as described earlier<sup>2,5,6</sup>. Briefly, 6-9 M $\Omega$  glass electrodes filled with ACSF were placed at a distance of 10-15  $\mu$ m from the dendrite (stimulation: 0.1 ms, 10-50 V, 10 ms pulse interval, 1-3 stimuli; BioStim, Supertech). Electrodes were targeted to the dendrite by a program written in MATLAB synchronizing the coordinate system of the patch-clamp manipulator and the microscope by the simultaneous use of two-photon imaging and transmitted oblique laser light data. Backpropagating APs were induced by somatic current injections (200-400 pA, 5 ms; 1-3 bAPs were evoked at 50 Hz).

### 5.1.3 Intrinsic imaging

During *in vivo* imaging and viral injection, the V1 region was localized with intrinsic imaging. For recording intrinsic signal first the skin was opened and the skull over the right hemisphere of the cortex was cleared. The intrinsic signal was recorded using the same visual stimulation protocol we used later during the two-photon imaging session.

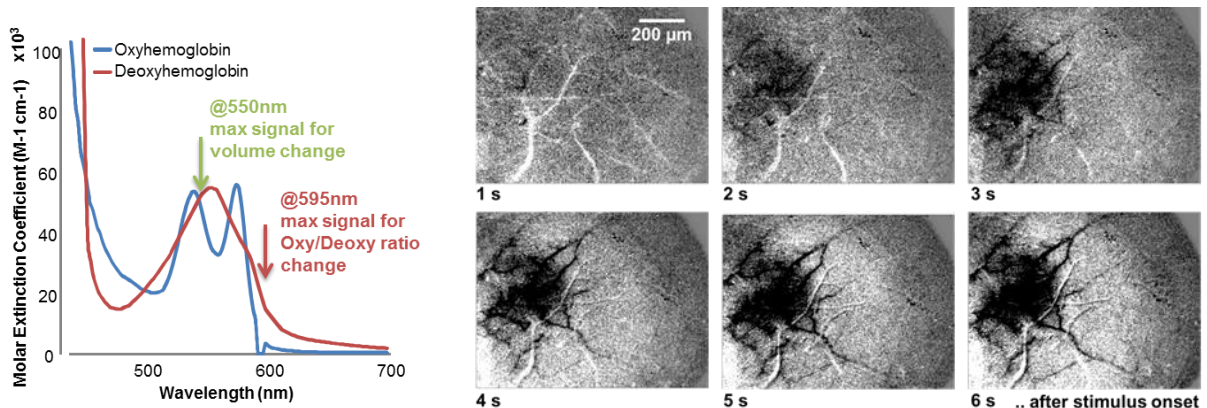


**Figure 12. Intrinsic imaging.** Left, absorption spectra of the oxy- and deoxy-hemoglobin shows that the highest relative difference in the absolute absorption of the two states of hemoglobin is present around 595nm, even if the highest absolute signal could have been detected with 550nm illumination. Right, normalized absorption of the brain surface 1-6s after the visual stimulation onset.

We could distinguish the region of interest by the absorption change in the given region, as described earlier<sup>48</sup>. Briefly, intrinsic imaging is based on the measurement of reflection change of the cortical surface. The source of the reflection change, depending

on the wavelength used for illumination, is either the change in oxygenization of the blood (595nm), or change in blood volume (550nm). Although the latter one has larger absolute signal, our aim was only to detect activation of V1, which could be detected more reliably with 595 nm illumination.

During the measurements we captured the baseline for 7 seconds in complete darkness, then moving bars were introduced for the mice for 7 seconds. Video signals were averaged for every second, and reflection change compared to baseline was calculated. Protocol was repeated 32 times and signals were averaged.

#### **5.1.4 AAV vector injection.**

The injection procedure was adopted from Chen et al. 2011 and Wertz et al 2015 with some modifications. A 0.5 mm hole was opened in the skull with the tip of a dental drill over the V1 cortical region (centered on average 0.5 mm anterior and 2 mm lateral to the lambda structure – previously localized by intrinsic imaging). The glass micro-pipette (tip diameter  $\approx 10 \mu\text{m}$ ) used for the injections was back-filled with 0.5  $\mu\text{l}$  vector solution ( $\approx 6 \times 10^{13}$  particles/ml) then injected slowly (20 nl/s for first 50 nl, and 2 nl/s for the remaining quantity) into the cortex, at a depth of 450  $\mu\text{m}$  under the pia. For population imaging we used AAV9.Syn.GCaMP6f.WPRE.SV40 or AAV9.Syn.Flex.GCaMP6f.WPRE.SV40 (in the case of Thy-1-Cre animals); both viruses were purchased from Penn Vector Core, Philadelphia, PA. For sparse labeling we injected the 1:1 mixture of AAV9.Syn.Flex.GCaMP6f.WPRE.SV40 and AAV1.hSyn.Cre.WPRE.hGH diluted 10,000 times. The cranial window was implanted over the injection site 2 weeks after the injection, as described in the surgical procedure section.

#### **5.1.5 Surgical procedure**

2-3 weeks after injection, mice were anaesthetized with a mixture of midazolam, fentanyl, and medetomidine (5 mg, 0.05 mg and 0.5 mg/kg body weight, respectively). A circular craniotomy (3 mm diameter) was made above the V1 cortex (localized before virus injection with intrinsic imaging) without touching the dura mater.

A custom-made aluminum head plate was fixed to the skull using cyanoacrylate glue and dental cement (**Figure 13**). During drilling, the place of craniotomy was rinsed

continuously with cold Ringer solution. When performing acute dendritic measurement the dura mater was also removed with a bended tip needle. The area of the craniotomy was covered with a double cover glass, as described previously<sup>49</sup>. For two-photon recordings, mice were awakened from the fentanyl anesthesia with a mixture of nexodal, revetor, and flumazenil (1.2 mg, 2.5 mg, and 2.5 mg/kg body weight, respectively) and kept under calm and temperature-controlled conditions for 10-20 minutes before the experiment. Before the imaging sessions, mice were kept head-restrained in the dark under the 3D microscope for at least 1 hour to accommodate to the setup. In some of the animals, a second or third imaging session was carried out after 24 or 48 hours.

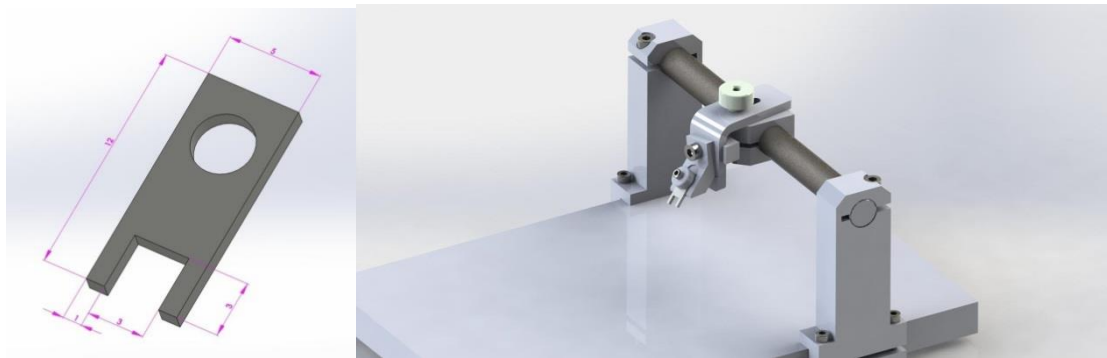


**Figure 13.** Custom made mouse head holder used during the experiments. (Left) Headplate mounted to the mouse's skull. (Right) In vivo holder.

### 5.1.6 Visual stimulation

A 15" computer monitor (Acer, 1280 x 768 pix resolution) placed 20 centimeters from the contralateral eye (covering  $\sim 100^\circ \times 70^\circ$  of the visual field) was used to cast the visual stimuli generated by a program written in MATLAB using the 'Psychtoolbox' add-on package (<http://psychtoolbox.org/wikka.php?wakka=HomePage>). To prevent stray light from entering the objective, a black cover was placed over the complete visual stimulation path. Each trial of the visual stimulation started by showing a black screen with a non-moving grating appearing at the edge of the screen after 2 s; after 1 s, the grating moved in a direction orthogonal to its orientation for 5 s (drifting speed 1 cycle per 1 s), was stopped for 1s, and then disappeared, leaving a black screen for a further 1 s and between the trials. Trials with eight different grating directions were tested with an angular interval of  $45^\circ$ .

### 5.1.7 Virtual reality environment

During the awake experiments, the mouse was head fixed, but free to run on a custom-designed linear treadmill made of a light rotating plastic plate (**Figure 14**). Easy rotation of the plate was provided by two ball-bearings (619/8, SKF). The motion of the treadmill was recorded with a high speed (1 kHz sampling rate) optical mouse (Urage reaper 3090, Hama) mounted upside down on the other side of the dial, and the angular displacement was recorded simultaneously at the same time as fluorescent signal. We used a self-developed script written in MATLAB to move the "wall" of the labyrinth on a 15" LCD screen according to the position signal of the optical mouse. Then we exported the output curves (velocity, position) to Excel for further analysis. Animals were habituated to the wheel for 20 minutes every day before the experiment, for at least three days, but no other behavioral training was used. For test of motion correction efficiency traces were divided into temporal intervals, running and rest, which were then separated by using a 2.6 mm/s speed threshold. See also **Figure 14** for more details.

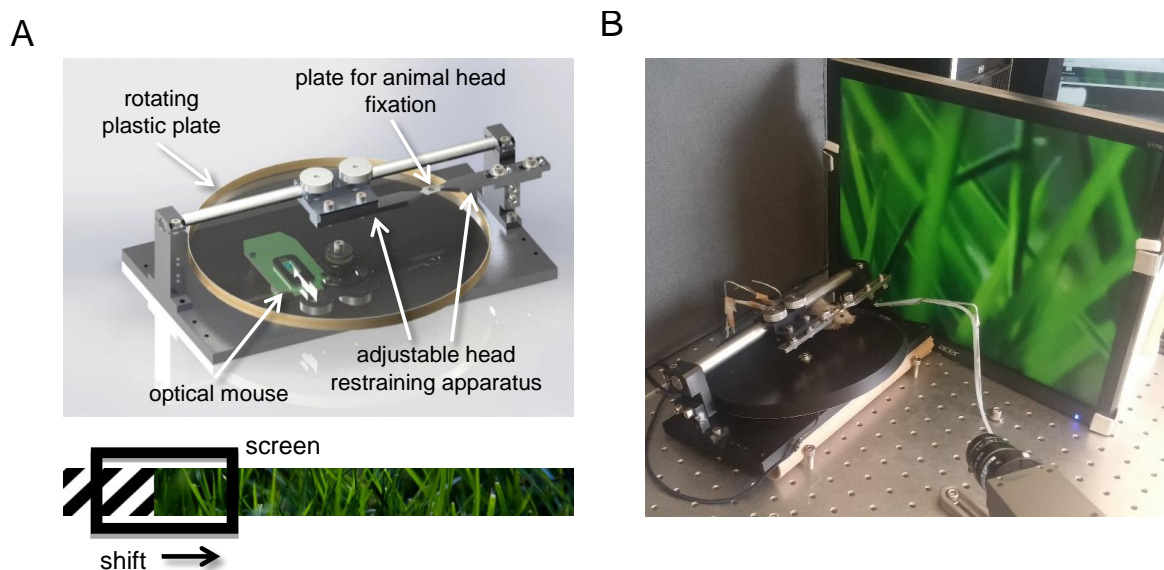


**Figure 14. Virtual reality (VR).** A linear treadmill was used to record the velocity of movement during fluorescent recording. (A) Solidworks image of the virtual reality environment. The position of a rotating light plastic plate was decoded by an optical mouse mounted upside down, and loaded into the MATLAB-based program. A 10 mm steel rod was stretched at both sides to minimize movement of the head-restraining apparatus during motion. A video screen placed in front of the left eye of the mouse was continuously updated according to the position signal with the actual part of an image. We realized a linear maze by teleporting the animal to the beginning of the VR image when it reached the end. (B) Image of the VR used with the 3D DRIFT AO microscope.

### 5.1.8 *In vivo* electrophysiology

To determine the correlation between  $\text{Ca}^{2+}$  transient and AP number, we performed cell-attached patch-clamp recording in *in vivo* conditions. The surgery was as described above, except for a small area left uncovered, about 1 mm wide, next to the cover glasses: this region was used as insertion site for the pipette, while the cells were measured under the cover glass, to limit tissue motion. For the recordings we used 7-8 M $\Omega$ -resistance borosilicate glass electrodes filled with extracellular solution, containing (in mM): 126 NaCl, 2.5 KCl, 2 CaCl<sub>2</sub>, 2 MgCl<sub>2</sub>, 1.25 NaH<sub>2</sub>PO<sub>2</sub>, and 100  $\mu\text{M}$  Alexa 594 (Invitrogen) to visualize the pipette. Electrophysiological data were recorded in current-clamp mode with 0 mV holding potential simultaneously with the calcium imaging. Transients were band-pass filtered between 1 Hz and 5 kHz and the number of APs was counted manually.

### 5.1.9 Data processing

Most of the analysis, including video rearrangement, motion correction, running average and  $\Delta F/F$  calculation was performed with the built-in analysis tools in the acquisition software (MES, Femtonics Ltd., Budapest, Hungary). Raw fluorescence data ( $F$ ) recorded along surface elements in 3D were spatially normalized, and then projected onto a 2D plot by applying the formula:  $\Delta F/F = (F(d_L, d_{tr1}, t) - F_0(d_L, d_{tr1}))/F_0(d_L, d_{tr1})$ , where  $t$  denotes time, and  $d_L$  and  $d_{tr1}$  indicate the longitudinal and the transversal distance along the ribbon, respectively. For 3D projection, 3D rendering, and 3D hyperstack analysis we used the ImageJ open-source software with some custom-written macros.

## 6 RESULTS

---

For reaching the settled aims, detailed in the previous section, we had to improve, on one hand, the imaging system for more reliable performance, and, on other hand, I had to design new measurement methodology for the most reliable use of these technical advances.

In the first part of the result section I will explain the technical advances that ensure the long-term reliable use of AO scanning from behaving animals. We made the following improvement compared to the previous system: (i) I have installed a four prism compressor and an angular drift compensation lens to the system, (ii) We designed new driving signals to the AO deflectors for faster scanning, (iii) and we designed new software component to realize new scanning methods.

### 6.1 *The new AO scanning system*

Before the detailed description of these developments, for the better understanding, I first explain the complete optical design of the final system, and then detail the necessity and function of the specific components. Since having an overall picture of the optical design will help to me to explain more easily the new developments in detail.

The 105 fs long laser pulses were delivered by a Ti:S laser at a 80 MHz repetition rate (Mai Tai, Spectra Physics, **Figure 15**). The coherent backreflections from optical elements were blocked by a new type of Faraday isolator (BB9-5I, EOT) that had a higher center wavelength (900 nm) and provided 5-10% higher throughput in the desired (850-950 nm) wavelength range (92% transmission at 900 nm) than the previous version<sup>2</sup>. The elimination of thermal drift errors were realized by two automated beam stabilization units (*beam stab. #1* and *#2*). Each stabilization unit was built from two position sensors (quadrant detectors,  $q1$ - $q2$ , and  $q3$ - $q4$ ) and two motorized mirrors ( $m1$ - $m2$ , and  $m9$ - $m10$ ), wired in a feedback loop. The first beam stabilization unit contained the following items:  $m1$ ,  $m2$ ,  $m3$ ,  $m4$ ,  $m5$ ,  $q1$ , and  $q2$  (**Figure 15**), where  $m1$  and  $m2$  are silver mirrors (PF03-03-P01, Thorlabs) in piezoelectric mounts (ASM003, Thorlabs) controlled by a high voltage electronic controller (TPZ001, Thorlabs) and  $m3$  and  $m4$

are backside polished broadband dielectric mirrors (BB1-E03P, Thorlabs). The position of the laser beam is detected by quadrant detectors ( $q1$  and  $q2$ , PDQ80A and TPA101, Thorlabs). All the electronics are mounted in a control hub (TCH002, Thorlabs) and programmed to perform closed-loop beam alignment at high speed ( $\approx 300$  Hz).

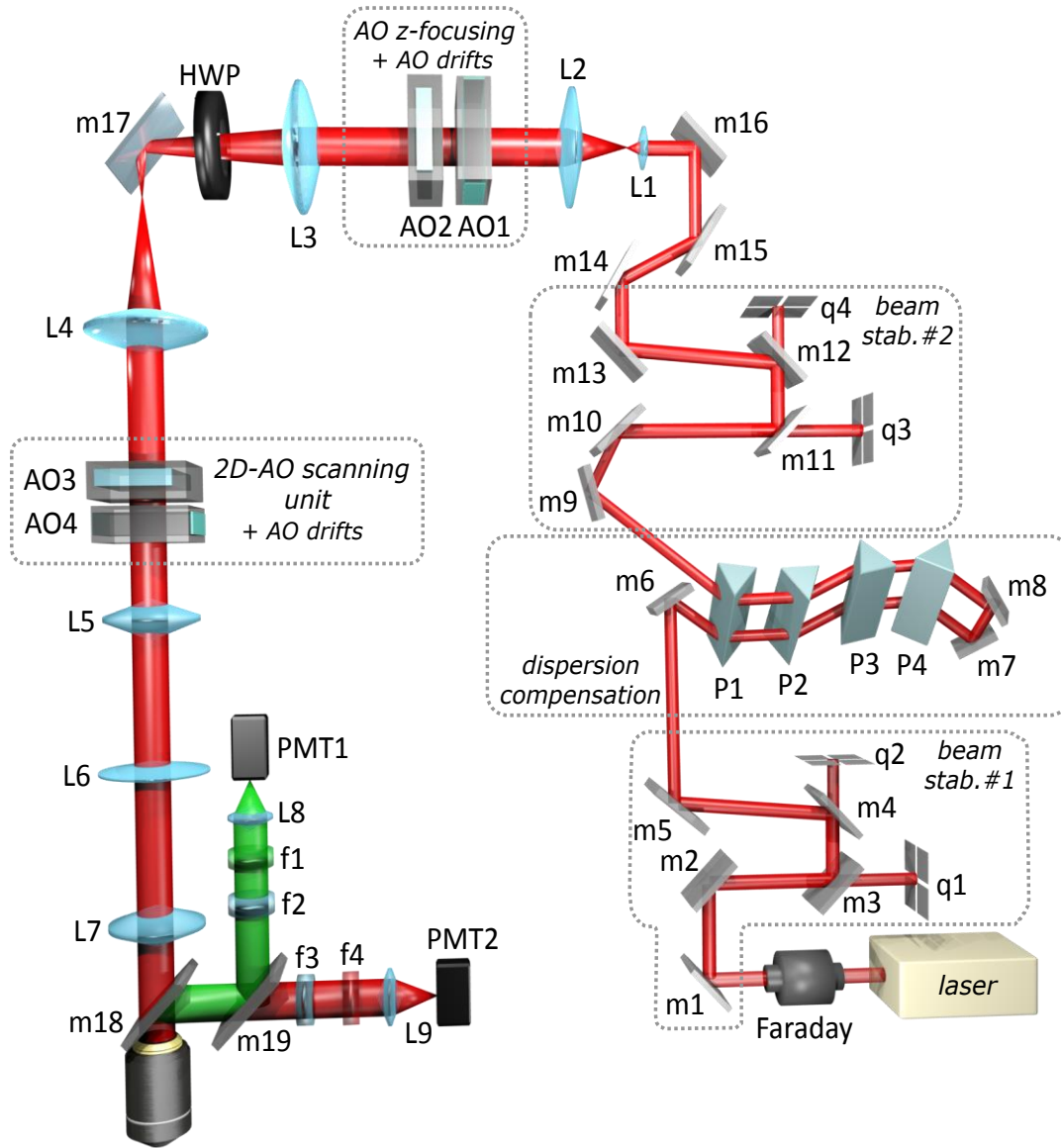


**Figure 15. Block diagram of the 3D DRIFT AO microscope and four-prism compressor unit.** Faraday: Faraday isolator, m1-17: broadband dielectric mirrors, m18-19: dichroic mirror, q1-4: quadrant detectors, P1-4: prisms, L1-7: lenses, A1-4: acousto-optic deflectors. (See details in the main text.)

The temporal dispersion introduced by the acousto-optic devices and other optical elements in the assembly is compensated by the introduction of a new, motorized four-prism compressor that optimizes the dispersion compensation parallel with the

wavelength tuning (**Figure 18**). The four prism sequence (*P1-P4*) is coupled to the light pathway by two broadband dielectric mirrors *m6* and *m9* (BB1-E03, Thorlabs), and consists of Brewster angle prisms from SF11 (320-8525 apex angle 59°, Eksma Optics). The apex distance between *P2* and *P3* was 692 mm at 880 nm. The retro reflector after the fourth prism (*m7* and *m8*) was made of two square dielectric broadband mirrors (BBSQ05-E03, Thorlabs). To obtain the same level of second-order dispersion compensation, the distance between the first and second prism pairs should vary linearly with wavelength. Moreover, the angle of refraction at the first prism pair changes with wavelength, so the second pair should be shifted in the plane of refraction to meet the refracted beam at the optimal position of its aperture. Therefore, the first group of prisms (*P1* and *P2*) was fixed, and the second group (*P3* and *P4*) and the two retro mirrors (*m7* and *m8*) were translated in the horizontal plane using two motorized linear slides with orthogonal axes. Positions could be set automatically at each target wavelength. This combination added a large negative second- (up to 75-80,000 fs<sup>2</sup>) and third-order (up to 35-40,000 fs<sup>3</sup>) dispersion that can be tuned with the wavelength. The amount of dispersion compensation required wasn't a monotonic function of wavelength, meaning that the distances between the first and second group of prisms need to be varied in a range between 650 mm and 970 mm in the desired 800-950 nm wavelength range in order to get the maximal two-photon excitation at the depth. The fine-tuning of the prisms was performed by optimizing the positions of the two motorized slides based on two-photon image contrast and SNR at each wavelength.

The second stabilization unit is placed after the prism compressor and contains the following items: *m9*, *m10*, *m11*, *m12*, *m13*, *q3*, and *q4*. The *m9* and *m10* broadband dielectric mirrors were mounted on motorized mirror mounts (U100-AC and NSA12, Newport) and driven by Newport servo motor controller and drivers (NSC200 and NSC-SB). The same types of quadrant detectors (*q3* and *q4*) were used (PDQ80A and TPA101, Thorlabs), as in the first beam stabilization unit. The beam alignment was performed by custom written software.

The beam expander consists of two achromatic lenses *L1* (ACN254-075-B, Thorlabs) and *L2* (AC508-2000-B, Thorlabs) and is connected to the optical pathway broadband dielectric mirrors (*m13*, *m14*, *m15*, and *m16*; BB1-E03 Thorlabs). *L1* and *L2* lenses were selected to set the laser beam to match the large apertures (15 mm) of the first pair

of AO deflectors. Some mirrors are omitted on the block diagram to make the beam path more manageable, these mirrors are 1 inch dielectric (BB1-E03, Thorlabs) before the beam expander, and 2 inch dielectric mirrors (BB2-E03, Thorlabs) after the beam expander.

The first two deflectors (*AO1* and *AO2*) formed two orthogonal electric cylinder lenses (*AO z-focusing unit*) and were filled with chirped acoustic waves. A new adjustment technique for the acousto-optical deflectors, a mechanical actuator with six degrees of mechanical freedom (instead of the former version with five degrees of freedom) meant it was possible to carefully align the deflection axes and accurately centralize the laser beam. Importantly, not only *z* focusing but also small extent *x* and *y* scanning was performed during 3D drifts with the *AO1* and *AO2* deflectors, respectively. The *z*-focusing unit and the 2D-AO scanning units were linked together by a telecentric relay system formed from two identical achromatic lenses of 150 mm effective focal length (*L3* and *L4*, #47-318, Edmund Optics). The lenses are arranged for best imaging of the back focal plane of the first lens to the image side focal plane of the second lens. These planes are aligned as close as possible to the intermediate planes between deflectors deflecting in the *x* and *y* directions, respectively. We used a 2-inch broadband dielectric mirror (BB3-E03, Thorlabs) to make the light way compact (*m17*). The half wave plate (*AHWP10M-980*, Thorlabs) ensures that the second pair of AO deflectors receives the entering light with a linear polarization oriented for optimal diffraction efficiency of the deflectors in the scanning unit. This wave plate is adjusted by monitoring the useful output of the scanner unit, and maximizing the deflected power. The wave plate compensates the rotation of the polarization plane caused by the first deflectors and the subsequent mirrors.

The 2D-AO scanning unit formed by two deflectors (*AO3* and *AO4*, Gooch and Housego) scans laterally and also sets the lateral and longitudinal drift of the focal spot, in cooperation with the *z*-focusing unit. The driving signals contain the appropriate radio frequency – time functions that move the focal spot along pre-defined 3D trajectories. Lateral scanning was minimized at the *z*-focusing and maximized at the 2D-AO scanning units by using the feature that only relative frequencies ( $\Delta f_{0x}$  and  $\Delta f_{0y}$ ) but not the absolute frequencies ( $f_{1x}(0,0)$ ,  $f_{2x}(0,0)$ ,  $f_{1y}(0,0)$ , and  $f_{2y}(0,0)$ ) parameters were determined by the starting position, and the speed of the 3D. The AO deflectors in the

scanning unit had the same aperture diameters (15 mm) and were made in the same crystallographic orientation as the deflectors of the focusing unit to simplify the acoustic driver frequency functions. The whole scanning assembly was based on large-aperture (15 mm) optical components. A first achromatic lens of 200 mm focal length  $L5$  (#47-319, Edmund Optics) focused the diffracted light beams onto the surface of a specially designed field lens  $L6$ , which was imaged onto the back aperture of the objective by an achromatic lens of 180 mm focal length  $L7$  (322246525, Linos).

The primary beam splitter ( $m18$ ) was a long-pass dichroic with a cut-on wavelength of 700nm (700dcrxu, Chroma Technology). The beam splitter that separates the red and green channels ( $m19$ ) was a long-pass dichroic with an edge at 600 nm (t600lpxr, Chroma Technology). The green absorption band pass filter ( $f1$ ) was centered at 520 nm with a range of 60 nm (ET520/60m, Chroma Technology), and the red filter ( $f4$ ) was centered at 650 nm with a range of 100 nm (ET650/100m, Chroma Technology). Extra IR filters ( $f2$  and  $f3$ : ET700sp-2p8, Chroma Technology) were introduced to both detection pathways to minimize the detection of the IR light backscattered into the photomultiplier units ( $PMT1$  and  $PMT2$ ). The fluorescent light is collected by planoconvex lens (LA1805-A, Thorlabs) in both the green and the red channels ( $L8$  and  $L9$ ). Photomultiplier cathode material was GaAsP (H10770PA-40, Hamamatsu). The entire detector unit ( $m18$ ,  $m19$ ,  $f1$ - $f4$ ,  $L8$ ,  $L9$ ,  $PMT1$ ,  $PMT2$ ) was fixed directly to the motorized objective arm to minimize the detection pathway. This therefore maximized detection of backscattered fluorescent light. We used a water-immersion 20 $\times$  objective (XLUMPlanFLN 20X, Olympus) with a 1.0 numerical aperture.

We also used a new method to mount mirrors. Previous mounting methods which used a rubber-ended screw on the side were not sufficient because they introduced stress and bent the mirror surface, resulting in a significant wavefront error which diminished resolution. Therefore we used UV-curing optical adhesive (NOA61, Thorlabs) to mount these critical mirrors, and to achieve diffraction limited spot in the center of the field.

## 6.2 Dispersion compensation

### 6.2.1 Material dispersion compensation

Material dispersion occurs because different spectral components are traveling with different speed in the optical material and can cause the elongation of the ultrashort laser pulses. As it have been shown<sup>50</sup> pulse length are inversely proportional with the induced two-photon signal. Since our deflectors are acoustically rotated for higher transmission efficiency, they have larger device length that is causing larger material dispersion. This large dispersion can increases the pulse length almost 100 times, thus decreasing fluorescent signal to 1% of what we could obtain with the original short pulses. That would reduce the signal-to-noise ratio to the level which is not sufficient for reliable in vivo imaging.

We have shown in a previous work that this high spatial dispersion can be compensated for, at least to a third order<sup>21</sup>. For the present optical design of the 3D microscope we needed to compensate for about 72,000 fs<sup>2</sup> second-order dispersion (GDD) and about 40,000 fs<sup>3</sup> third-order dispersion (TOD) - the precise amount depends on the objective used and also on the central wavelength ( $\pm 1000$  fs<sup>2</sup> and  $\pm 730$  fs<sup>3</sup>). Material dispersion compensation is realized by a custom designed, motorized two-pass four-prism compressor<sup>51</sup> to provide the desired compensation at a given wavelength. The level of GDD and TOD compensated by the four-prism compressor can be adjusted by changing the spacing between the prisms. To test our compressor design, pulse length measured in front of the objective with an autocorrelator (Mini, APE GmbH). The four-prism compressor is set to obtain close to the minimum pulse length (~108 fs), that required 70 mm, 950 mm, and 80 mm distance between prisms, respectively, at 880 nm which is in good agreement with the modeling data.

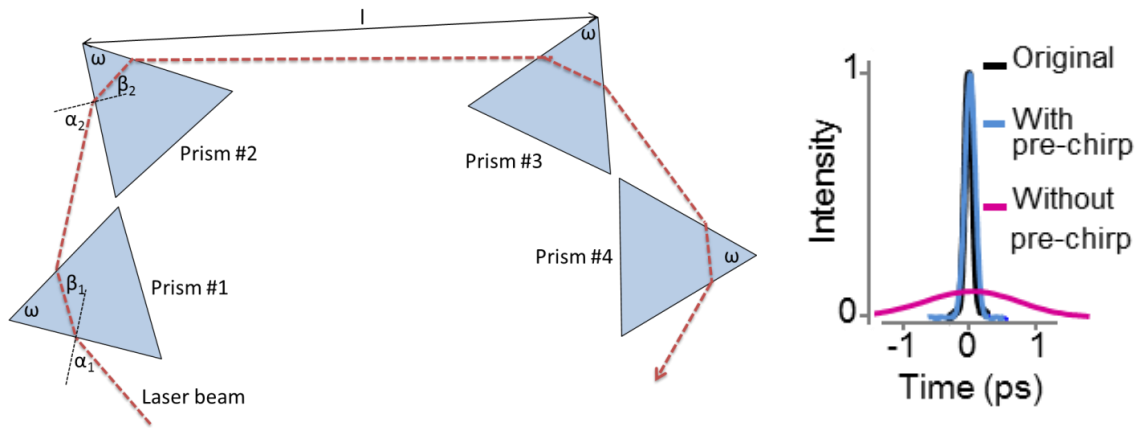


**Figure 16. Pulse compression.** Left, notation for the equations on pulse compression. Right, temporal length of the individual laser pulses at the output of the laser, without and with pulse compression. (Pulse lengths: original – 97fs; with pre-chirp compensation – 108fs; without pre-chirp – 1.4ps)

### 6.2.2 Calculating material dispersion introduced by the optical pathway

For the accurate material dispersion compensation we should first define the amount of dispersion introduced by our optical design. To calculate this material dispersion first I determined the distance travel by the laser light in all of the different materials we used in the system, including all the optical elements, the AO crystals, and also in the air between these components. Then I determined the wavelength dependent refractive index for the materials used in the optical system. **Figure 17** shows that for glass SF6. Similar equation can be drawn for all the materials used. Next I summed up the optical distance travelled in all separate materials, calculated from the complete optical model of the system. Namely: Air: 1209.36 mm; TeO<sub>2</sub> crystal (orthogonal orientation): 60.26 mm; TeO<sub>2</sub> crystal (ex-orientation): 60.26 mm, LAKN22 glass: 21.94 mm; SFL6 glass: 11.03mm; BK7 glass: 7.86 mm; SF5 glass: 4.24 mm; SF10 glass: 4.21 mm; BAK4 glass: 8.95 mm.

Refractive index coefficients for Hikan E-SFL6 glass:

$$\begin{aligned} SFL6_1 &= 3.117837 & SFL4 &= 1.813481 \cdot 10^{-3} \\ SFL6_2 &= 1.194107 \cdot 10^{-2} & SFL5 &= 4.696699 \cdot 10^{-6} \\ SFL6_3 &= 4.436023 \cdot 10^{-2} & SFL6 &= 1.617541 \cdot 10^{-5} \end{aligned}$$

Wavelength dependent refractive index of Hikan E-SF6 glass:

$$\begin{aligned} n_{SFL6}(\lambda) \\ = \sqrt{SFL6_1 + SFL6_2 \cdot \lambda^2 + SFL6_3 \cdot \lambda^{-2} + SFL6_4 \cdot \lambda^{-4} + SFL6_5 \cdot \lambda^{-6} + SFL6_6 \cdot \lambda^{-8}} \end{aligned} \quad (\text{Equation 3})$$

The above equation, thus the wavelength dependent refractive index of the SFL6 glass can be visualized as follows:

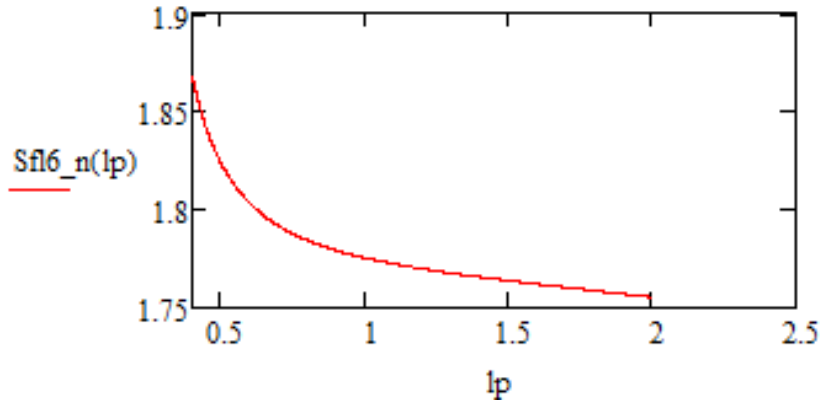


**Figure 17.** Wavelength dependent refractive index of SFL6 glass (where  $lp$  refers to wavelength in  $\mu m$ ).

Having the wavelength dependent refractive index for all the material used, and knowing the optical length for all (the sum distance the light traveled in the given type of material), the phase shift induced by the optical elements can be defined as:

$$\begin{aligned} \varphi(\omega) = \frac{\omega}{c} (l_{Air} \cdot n_{Air}(\omega) + l_{TeO2o} \cdot n_{TeO2o}(\omega) + l_{TeO2e} \cdot n_{TeO2e}(\omega) + l_{LaKN22} \cdot \\ n_{LaKN22}(\omega) + l_{SFL6} \cdot n_{SFL6}(\omega) + l_{Bk7} \cdot n_{Bk7}(\omega) + l_{SF5} \cdot n_{SF5}(\omega) + l_{SF10} \cdot \\ n_{SF10}(\omega) + l_{Bak4} \cdot n_{Bak4}(\omega)) \end{aligned}$$

(Equation 4)

where  $\varphi(\omega)$  is the phase shift,  $c$  is the speed of light in vacuum. For the material dependent variables,  $n_{Air}(\omega)$ , for example, is the refractive index in air and  $l_{Air}$  is the

distance traveled in this material, all others material are referred similarly. From these equations the second and third order of dispersion could be calculated as follows:

$$GDD(\omega) = \frac{d^2}{d\omega^2} \varphi(\omega) \quad (\text{Equation 5})$$

$$TOD(\omega) = \frac{d^3}{d\omega^3} \varphi(\omega) \quad (\text{Equation 6})$$

For 800 nm light GDD and TOD, so the second and third order dispersion which has to be compensated are:  $GDD(800\text{nm}) = 74\,430\text{ fs}^2$  and  $TOD(800\text{nm}) = 51\,163\text{ fs}^3$ .

See **Table 1** for GDD and TOD presented by the AO crystals at different wavelengths.

**Table 1. Material dispersion of the complete system.** The table presents the GDD and TOD presented by an acousto-optical deflector at different wavelengths.

| wavelength             | 800 nm | 875 nm | 900 nm | 925 nm | 950 nm |
|------------------------|--------|--------|--------|--------|--------|
|                        | 800 nm | 875 nm | 900 nm | 925 nm | 950 nm |
| GDD (fs <sup>2</sup> ) | 14342  | 12663  | 12194  | 11660  | 11267  |
| TOD (fs <sup>3</sup> ) | 8543   | 7752   | 7545   | 7340   | 7153   |

### 6.2.3 Determining prism compressor axis lengths

Next I designed the optimal spacing and geometry of the prisms to compensate for the calculated material dispersions. Two-prism configuration would only be sufficient with very large distance between the crystals and very large crystals apex length that would reduce both transmittance efficiency and beam stability more than it is reasonable. Thus a four prism configuration was designed.

The optimal vertex angle of the prisms for minimal reflection on the prism's surface can be calculated as:

$$\alpha(\lambda) = \tan^{-1} \left( \frac{n_0(\lambda)}{n_{Air}(\lambda)} \right) \quad (\text{Equation 7})$$

$$\beta(\lambda) = \sin^{-1} \left( \sin \alpha(\lambda) \cdot \frac{n_{Air}(\lambda)}{n_0(\lambda)} \right) \quad (\text{Equation 8})$$

$$\omega(\lambda) = 2 \cdot \beta(\lambda) \quad (\text{Equation 9})$$

where  $n_0(\lambda)$  is the wavelength dependent refractive index of the prism's material and  $n_{Air}(\lambda)$  is the refractive index of the material between the prism. For this calculation I used the refractive index of 22°C, particle free air.  $\alpha(\lambda)$  is the input angle of the beam at

Brewster angle, which provides the minimal reflection for the given  $\lambda$  wavelength.  $\beta(\lambda)$  is the incident angle between the prisms wall and the beam, inside the prism.  $\omega(\lambda)$  is the vertex angle for the given  $\alpha(\lambda)$  and  $\beta(\lambda)$  values. For 800 nm center wavelength and SFL6 glass as prism material  $\alpha = 59.697$  deg,  $\beta = 30.303$  deg, so  $\omega$ , thus the optimal apex angle for this prism material is 60.6 deg.

We used prism with this (ideal) optical apex angle, as calculated above, and placed them in the light path so the light enters all crystals in the optimal Brewster angle. These conditions determine the angle of all prisms relative to each other, so the only freedom left in the design is the distance between the components. Taking this in account, the distance traveled by the light beam in each crystal, depending of the wavelength, can be calculated as follows:

**Prism 1:**

$$\varphi_1 = \alpha(\lambda_0)$$

$$d_{1,be}(\lambda) = d_1$$

$$\gamma_1(\lambda) = \sin^{-1} \left( \sin(\varphi_1) \cdot \frac{n_{Air}(\lambda)}{n_1(\lambda)} \right)$$

$$\delta_1(\lambda) = \omega(\lambda_0) - \gamma_1(\lambda)$$

$$\varepsilon_1(\lambda) = \sin^{-1} \left( \sin(\delta_1(\lambda)) \cdot \frac{n_1(\lambda)}{n_{Air}(\lambda)} \right)$$

$$d_{1,ki}(\lambda) = d_{1,be} \cdot \frac{\cos(\gamma_1(\lambda))}{\cos(\delta_1(\lambda))}$$

$$l_1(\lambda) = d_{1,be} \cdot \frac{\cos(\omega(\lambda_0))}{\cos(\delta_1(\lambda))}$$

**Prism 2:**

$$\varphi_2 = \varphi_1 + \varepsilon_1(\lambda) - \varepsilon_1(\lambda_0)$$

$$d_{2,be}(\lambda) = d_1 + (d_{1,ki}(\lambda_0) - d_{1,ki}(\lambda)) + l_{12} \cdot \frac{\sin(\varepsilon_1(\lambda_0) - \varepsilon_1(\lambda))}{\cos(i(\lambda))}$$

$$\gamma_2(\lambda) = \sin^{-1} \left( \sin(\lambda_0) \cdot \frac{n_{Air}(\lambda)}{n_2(\lambda)} \right)$$

$$\delta_2(\lambda) = \omega(\lambda_0) - \gamma_2(\lambda)$$

$$\varepsilon_2(\lambda) = \sin^{-1} \left( \sin(\delta_2(\lambda)) \cdot \frac{n_2(\lambda)}{n_{Air}(\lambda)} \right)$$

$$d_{2,ki}(\lambda) = d_{2,be} \cdot \frac{\cos(\gamma_2(\lambda))}{\cos(\delta_2(\lambda))}$$

$$l_2(\lambda) = d_{2,be} \cdot \frac{\cos(\omega(\lambda_0))}{\cos(\delta_2(\lambda))}$$

where  $\gamma_1(\lambda)$  and  $\gamma_2(\lambda)$  is the wavelength dependent entering angle of the given beamlet into the first and second prisms,  $\delta_1(\lambda)$  and  $\delta_2(\lambda)$  is the angle of the beam inside the prisms included with the prism's wall and the given beamlets, while  $\varepsilon_1(\lambda)$  and  $\varepsilon_2(\lambda)$  is the angle how the beamlets with different wavelength leaving the crystals.  $n_2(\lambda)$  and  $n_1(\lambda)$  are the refractive index of the first and second prism.  $d_{1,be}(\lambda)$  and  $d_{2,be}(\lambda)$  is the distance of the wavelength dependent entering site to the prism measured from the crystals' apex, while  $d_{1,ki}(\lambda)$  and  $d_{2,ki}(\lambda)$  is the position where the given beamlet leaving the crystal.  $l_1(\lambda)$  and  $l_2(\lambda)$  are the distance traveled by the light with a given

wavelength in the prisms. Prism 3 is symmetric to Prism 2 while Prism 4 is symmetric to Prism 1, thus I won't detail the equation for these crystals here.

From the difference in the traveled distance of the beamlets of different wavelengths inside the prisms the negative phase shift can be calculated as:

$$L(\lambda) = n_1(\lambda) \cdot l_1(\lambda) + n_2(\lambda) \cdot l_2(\lambda) + n_3(\lambda) \cdot l_3(\lambda) + n_4(\lambda) \cdot l_4(\lambda)$$

$$\Psi(\lambda) = \frac{2\pi}{\lambda c} \cdot L(\lambda) \quad \Psi'(\omega) = \Psi\left(\frac{2\pi c}{\omega}\right) \quad (\text{Equation 10})$$

where  $c$  is the speed of light.  $\Psi(\omega)$  is the phase shift calculated in the frequency band.

From the total phase shift result as:

$$GD(\omega) = \frac{d}{d\omega} \Psi'(\omega) \quad (\text{Equation 11})$$

$$GDD(\omega) = \frac{d^2}{d\omega^2} \Psi'(\omega) \quad (\text{Equation 12})$$

$$TOD(\omega) = \frac{d^3}{d\omega^3} \Psi'(\omega) \quad (\text{Equation 13})$$

After optimization of the equations, using the actual parameters of the optical design, we got the following geometrical parameters for the optimal pulse compressor.

| <i>Distance from the vertex at the<br/>central wavelength</i> | <i>Distance of prism along the<br/>central wavelength</i> |
|---|---|
| $d_1 = 5 \text{ mm}$  | $l_{12} = 70 \text{ mm}$                                  |
| $d_2 = 5 \text{ mm}$  | $l_{23} = 930 \text{ mm}$                                 |
| $d_3 = 13 \text{ mm}$   | $l_{34} = 80 \text{ mm}$                                  |
| $d_4 = 13 \text{ mm}$   |   |

where  $d_1, d_2, d_3$  and  $d_4$  is the distance of the position where the center wavelength of the beam enters the first, second, third and fourth crystal and the apex of the given prism, while  $l_{12}, l_{23}$  and  $l_{34}$  is the distance between the first and second, second and third and third and fourth prisms.

From these distances, supposing that the light is crossing the prism compressor two times in the optical design, the compensated material dispersion for 800 nm wavelength is:  $GDD_{comp}(800nm) = 79\,525\text{ fs}^2$  and  $TOD_{comp}(800nm) = 87\,174\text{ fs}^3$ .

As it can be seen when we fully compensate for GDD and mostly the higher order dispersion elements are overcompensated (the  $5000\text{ fs}^2$  difference between the desired and the actual compensation is inserted for compensating for the material dispersion of the objective<sup>52</sup>). Unfortunately there is no optimal four prism arrangement which can separately handle all orders. In practice we did not see the effect on the acquired images neither on raw fluorescent intensity nor on dF over F counts.

The final four prisms compressor design (shown on **Figure 18**) is built with motorized movement of the prism pairs, thus the designed optical arm lengths can be easily reached. Using this compensation, we could not detected significant change in the image quality or the signal brightness when used the same excitation energy, between a 2D system whit no significant material dispersion and the AO system where the introduced dispersion is compensated.

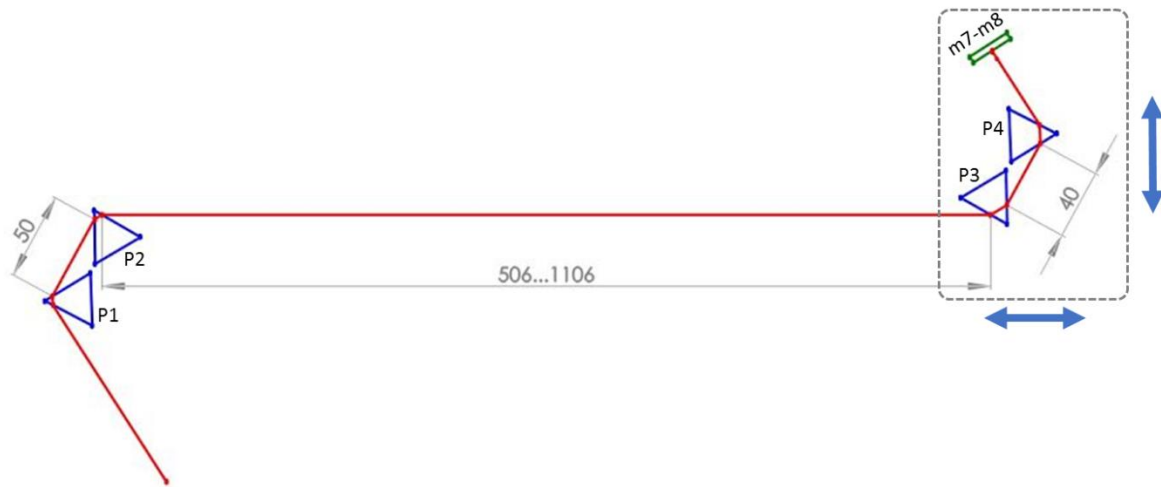


**Figure 18. Four-prism compressor unit.** Mechanical model for realization of the compressor with the arm lengths designed by my calculations. P1-P4: prisms; m7-m8: broadband dielectric mirrors; gray numbers: distances in mm; blue arrows: direction of movement of the motorized mirrors. See details in the main text.)

#### 6.2.4 Angular dispersion compensation.

Besides the material dispersion, the AO crystals and other optical elements introduce a large spherical inhomogeneity to the laser beam that will cause a large angular dispersion in the image field (up to 6 mRadian), thus object on the side of the field of view will appear elongated. The main ground of this effect is that the different spectral components of the ultrashort laser beam are diffracted differently on the AO deflectors. This effect is larger at the edges of the imaging field, causing a spatial dependent aberration of the point spread function. The exact properties of this dispersion could be determined from the optical model and fully compensated.

The angular dispersion compensating unit made of highly dispersive glass and placed in the focus of a 250 mm focal length lens (the scan lens of the AO imaging light path), positioned after the scanner unit. In order to calculate the surface equation of this lens element we need to go back to the general equation of prisms. The amount of angular dispersion which one prism can compensate for can be matched by properly selecting the incidence angle  $\alpha_1$  and the prism's opening angle  $\alpha_p$ . The output angle ( $\alpha_2$ ) after the prism is given by:

$$\alpha_2(\alpha_1, \alpha_p, \lambda) = a \sin \left( n(\lambda) \sin \left( \alpha_p - a \sin \left( \frac{\sin(\alpha_1(\lambda))}{n(\lambda)} \right) \right) \right),$$

where  $n(\lambda)$  is the refractive index. The wavelength-dependent incidence angle can be determined from the rotation angle of the prism  $\beta$  relative to the optical axis, hence the wavelength-dependent angle of propagation of the diffracted beams  $\theta_{def}$ :

$$\alpha_1(\lambda) = \theta_{def}(\lambda, f_1, f_2) - \beta,$$

and the total deflection angle of the prism:

$$\Delta\alpha(\alpha_1, \alpha_p, \lambda, f_1, f_2) = \theta_{def}(\lambda, f_1, f_2) + \beta - a \sin \left( n(\lambda) \sin \left( \alpha_p - a \sin \left( \frac{\sin(\theta_{def}(\lambda, f_1, f_2) - \beta)}{n(\lambda)} \right) \right) \right) - \alpha_p,$$

The zero angular dispersion requirement after the prism can be expressed as:

$$\frac{\partial[\Delta\alpha(\alpha_1, \alpha_p, \lambda, f_1, f_2)]}{\partial\lambda} = 0$$

The beams deflected at different frequencies in the scanner are spatially separated in the focal plane of the first part of this unit. The different optical wavelength components in each deflected wave are also spatially and angularly dispersed in this plane, and their dispersion also increases as the deflection angle increases, but their spatial dispersion is an order of magnitude less than the separation caused by the acousto-optic deflection. In this case, the angular dispersion increases symmetrically with the distance from this axis,  $r$  ( $r = \sqrt{x^2 + y^2}$ ).

The optimal surfaces, however, are not spherical surfaces, but can be expressed as aspheric and conic surfaces with the primary radii given by the equations:

$$c = \frac{\frac{I}{R_l} r^2}{1 + \sqrt{1 - (1 + k_l) \frac{r^2}{R_l}}} + \sum_{n=1:6} a_n r^n$$

where the  $k_l$  conic and  $a_n$  aspheric parameters are determined by optical modeling. The value of the radius and the minimum glass thickness at the optic axis is also determined with optimization using the ZEMAX optimization algorithms. Two merit functions are consecutively used, one containing the angular dispersion and aperture in front of the objective, and a second targeting the minimum spot size in the sample plane (the focal plane of the objective). Iteration of these two leads to optimized lens surfaces for the given material and the problem set (see details in Katona et al 2012).

When comparing a 3D setup using a simple telescope instead of a telescope with the lens element included as described above, we can obtain a lateral field of view which is ~2-fold larger, with the same focused spot size and dispersion at the edges of this area (see **Figure 19** and **Figure 20** below).

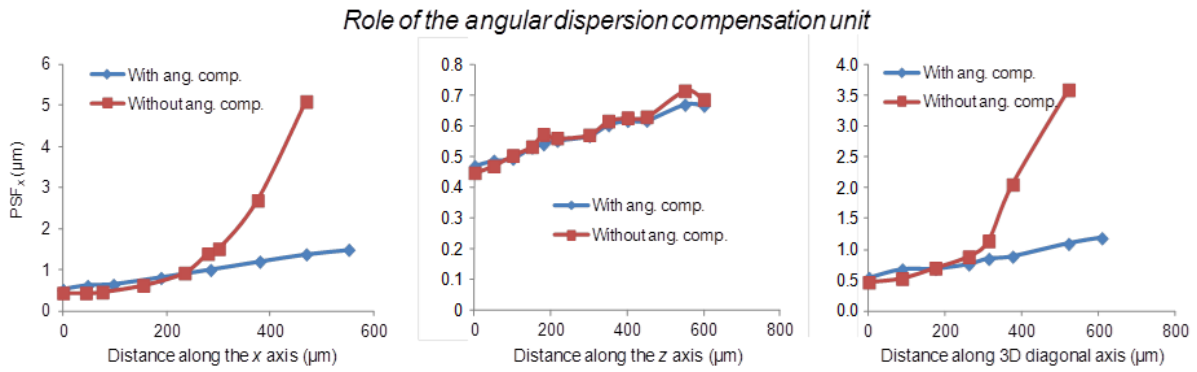


**Figure 19. Angular dispersion compensation.**  $PSF_x$  calculated as a function of distance from the origin along the  $x$ ,  $z$ , and diagonal axes (azimuth:  $45^\circ$ , altitude:  $45^\circ$ ) with (red traces) and without (blue traces) the angular dispersion compensation unit. Note that, at greater distances from the origin, angular dispersion due to the compensation unit has a reduced effect on PSF size.

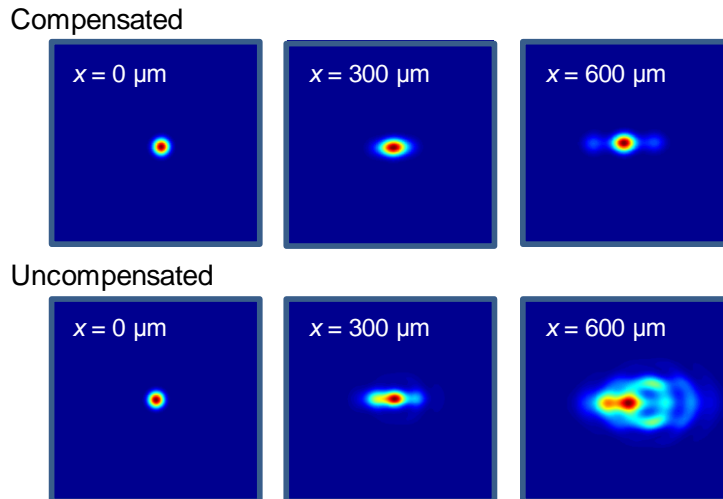


**Figure 20. Effect of angular dispersion compensation on the focal spot.** Simulated focal spot intensity distributions, squared in order to simulate the two-photon excitation efficiency, with (top) and without (bottom) the angular dispersion compensation unit in the  $z = 0$  plane at  $x = 0$ ,  $300 \mu\text{m}$ , and  $600 \mu\text{m}$  from the origin along the  $x$ -axis. Note the increasing spread of the spot distribution due to angular dispersion with increased distance from the origin when the angular dispersion compensation unit is not included (uncompensated).

### ***6.3 Increased transmittance efficacy and scanning volume at long wavelengths***

The scanning volume of the previous version of our 3D AO microscope was  $700\ \mu\text{m} \times 700\ \mu\text{m} \times 1,400\ \mu\text{m}$  in transparent samples and was limited to  $400\ \mu\text{m} \times 400\ \mu\text{m} \times 500\ \mu\text{m}$  during *in vivo* measurements with synthetic dyes due to the low transmitted laser intensity (about 10%)<sup>2</sup>. Furthermore, these measurements were performed at 800 nm central wavelength, where Ti:S lasers have an intensity maximum and AO deflectors work with high efficiency. In contrast, at longer wavelengths (above 880 nm), that is required for genetically encoded calcium sensors, such as GCaMP6, the output laser intensity and the total transmission of the scan-head dropped overall by about 3.5-fold and, therefore, the scanning volume was reduced to about  $150\ \mu\text{m} \times 150\ \mu\text{m} \times 200\ \mu\text{m}$ . To increase the total transmission efficiency we have further improved the 3D scan-head and the whole optical pathway. First we installed AO deflectors optimized for longer wavelength, 850-950 nm (**Figure 21**). Also we have increased the center frequency to extend the AO bandwidth, optimized AO deflector angles by carefully modeling the wavelength sensitivity of AO cell orientation<sup>53</sup>, and changed many further opto-mechanical elements to be ideal for this longer wavelength.

Finally, we optimized the electric circuitry coupling the driver signal to the piezo transducer, to increase the AO wave generation efficiency and bandwidth. Thanks to these improvements we were able to achieve about a 4-fold higher transmission in the range of 850-950 nm (**Figure 22**). Thanks to the increased transmission efficiency, the broad field of view, large 3D scanning volume and somatic resolution for the whole field of view as in our earlier work<sup>2</sup> was also well preserved at longer wavelengths (the scanning volume now  $650\ \mu\text{m} \times 650\ \mu\text{m} \times 1100\ \mu\text{m}$  in transparent sample at 880nm).

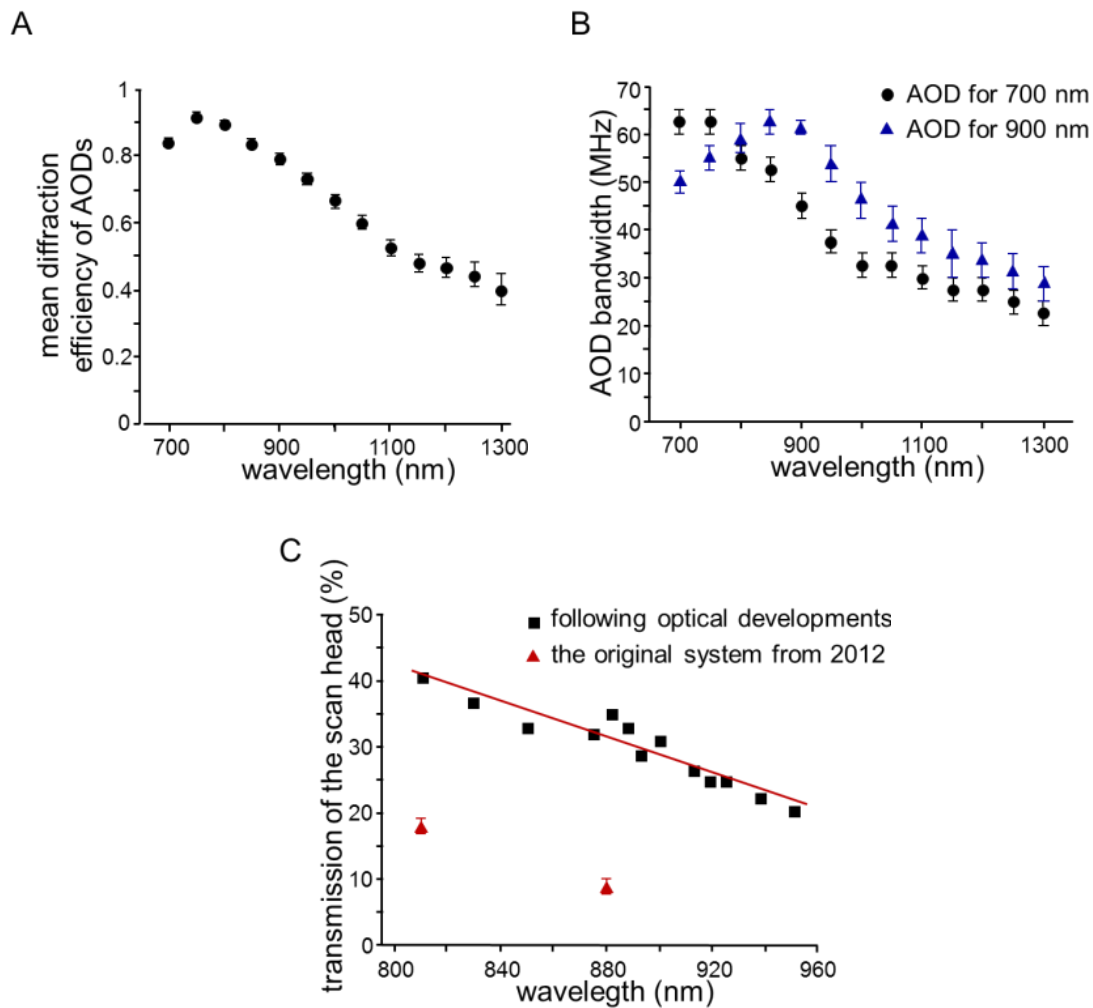


**Figure 21. Transmittance efficiency of the AOD crystals.** (A) Maximal diffraction efficiency (mean  $\pm$  SEM) of AO deflectors as a function of wavelength. The maximal diffraction efficiency was independent of crystal orientation: data from AO deflectors developed for different wavelengths were therefore pooled. (B) In contrast, AOD bandwidth did depend on crystal orientation. Full width at half maximum (FWHM) of diffraction efficiency as a function of wavelength for deflectors where the acoustic wave propagated at a higher angle ( $10^\circ$ ) relative to the  $[1,1,0]$  crystallographic axis (blue) was compared to the one of deflectors with a lower relative propagation angle ( $8.5^\circ$ ) (black). The first deflector with a  $10^\circ$  relative angle was optimized for 900 nm and the second for 700 nm. (C) Maximal transmission of the scan head as a function of wavelength (black). The maximal transmission was measured in the center (at  $x,y,z=0$ ) and decreased as a function of wavelength. Red triangles show transmission of the scan head of the earlier version of the microscope<sup>2</sup>.

The spatial resolution decreased as a function of distance from the center, but remained smaller than the typical diameter of neuronal somata in the entire scanning volume. The maximal scanning volume was about  $500 \mu\text{m} \times 500 \mu\text{m} \times 650 \mu\text{m}$  with the GCaMP6f sensor during *in vivo* measurements (**Figure 23**). This volume is more than two orders of magnitude larger than those previously reported with GECIs<sup>14</sup>. Importantly, in these

measurements we used a high numerical aperture objective (NA = 1.0) which provided a good spatial resolution (about 400 nm in the center). Obviously, with low-magnification objectives we can extend the scanning volume, but the lower numerical aperture of the currently available low magnification objectives decreases spatial resolution<sup>2</sup>.

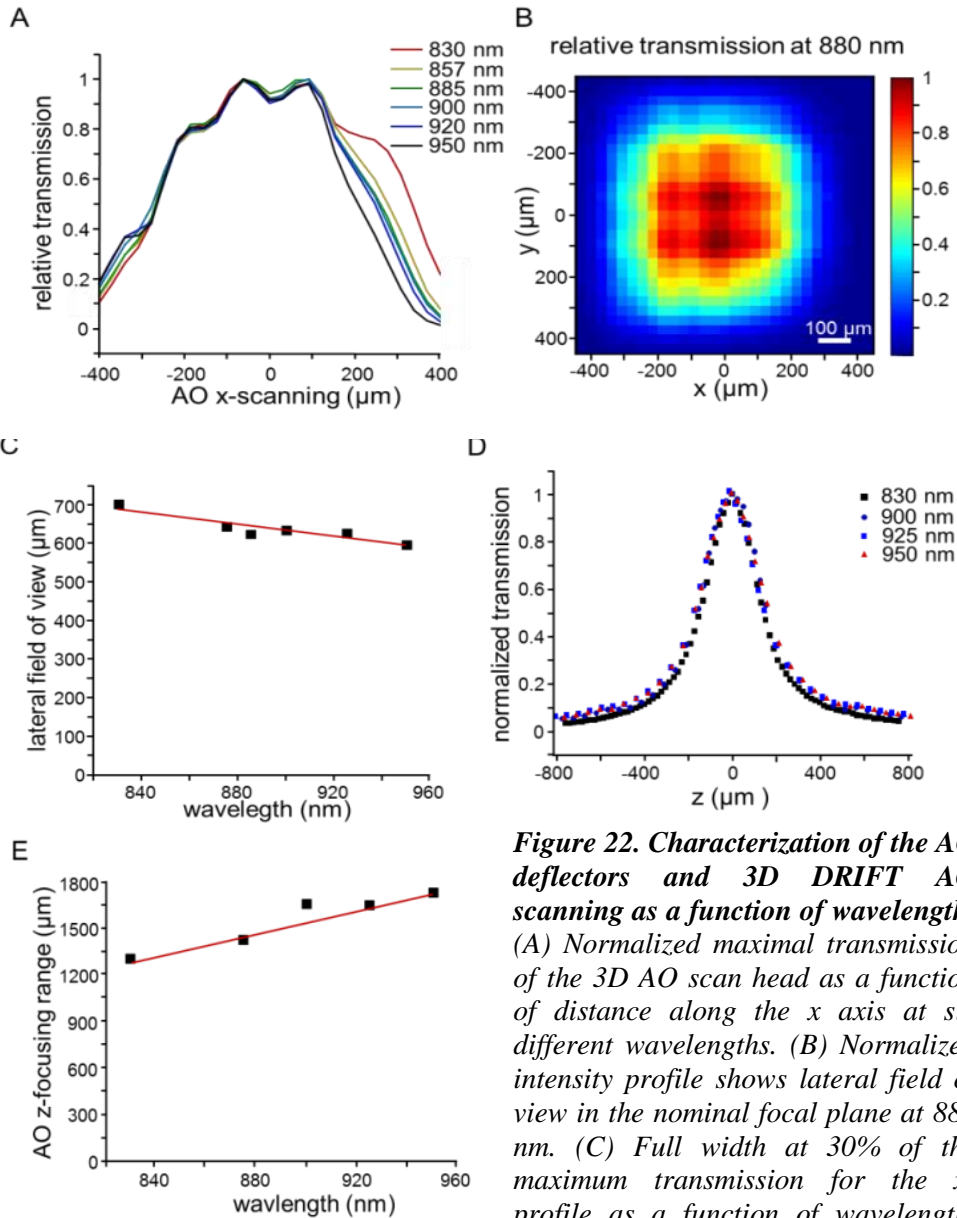


**Figure 22. Characterization of the AO deflectors and 3D DRIFT AO scanning as a function of wavelength.**

(A) Normalized maximal transmission of the 3D AO scan head as a function of distance along the x axis at six different wavelengths. (B) Normalized intensity profile shows lateral field of view in the nominal focal plane at 880 nm. (C) Full width at 30% of the maximum transmission for the x-profile as a function of wavelength. (D) Normalized transmission of the 3D

AO scan head at different states of AO z focusing (from  $-800 \mu\text{m}$  to  $+800 \mu\text{m}$ ) for four different wavelengths (830 nm, 900 nm, 925 nm, 950 nm). Note that the z profile of the transmission becomes wider as a function of increasing wavelength. (E) Full width at 5% of the maximum transmission for the normalized z-profiles (AO z-focusing range) as a function of wavelength.

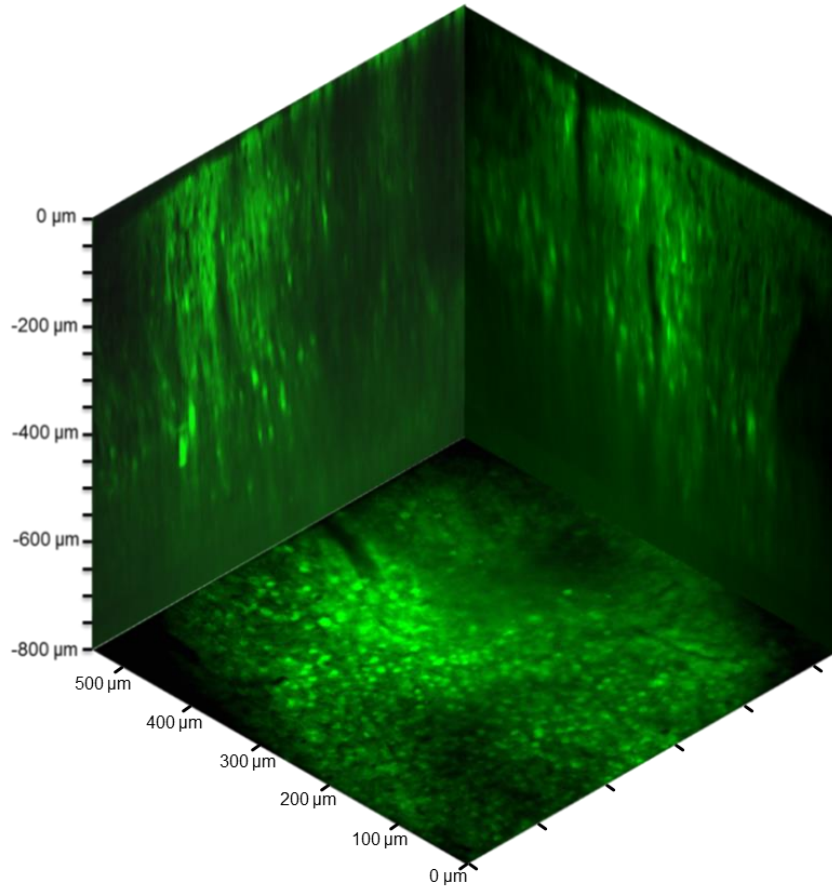


**Figure 23.**  $800 \times 550 \times 550 \mu\text{m}$  block of the cortex labeled with GCaMP6f. Z-stack taken with AO random access scanning.

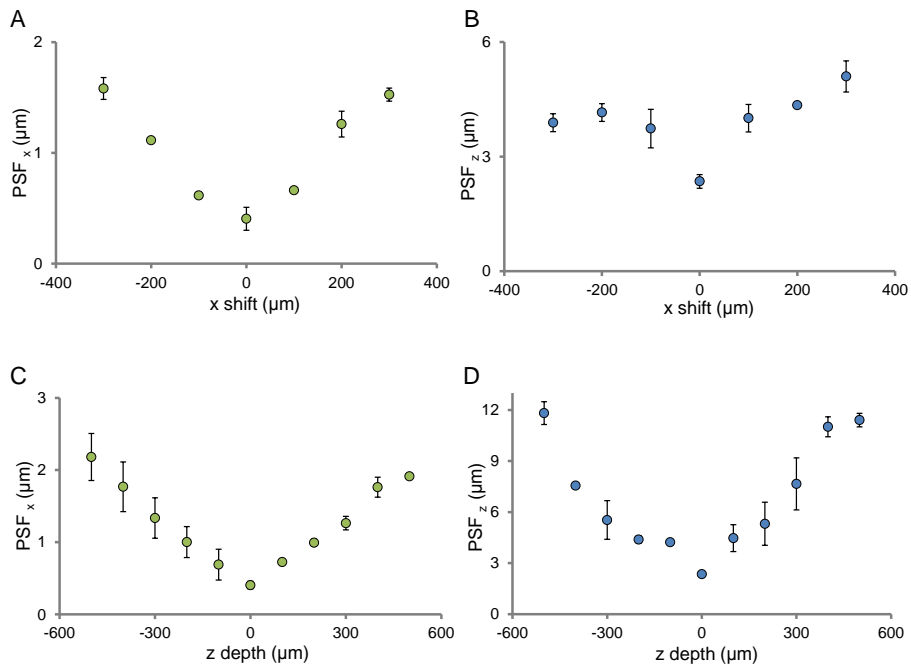


**Figure 24.** Full width at half maximum values (mean  $\pm$  SEM) of the point spread function along the z and x axes were plotted as a function of distance along the x and z axes.

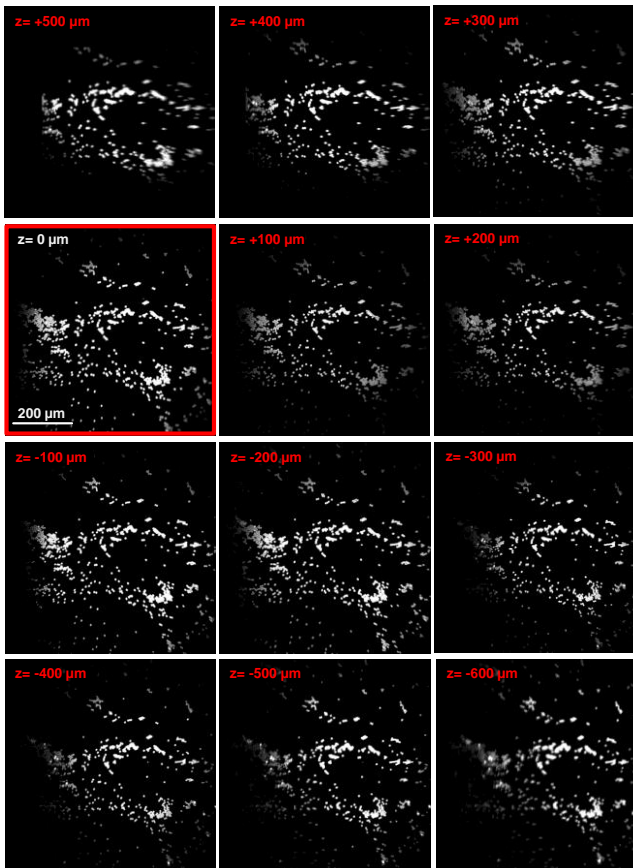


**Figure 25.** Maximal field of view of the 3D DRIFT AO microscope with the 20 $\times$  objective at different AO  $z$ -focusing levels (from  $-600\ \mu\text{m}$  to  $+500\ \mu\text{m}$ ). Images were taken at 880 nm. The fluorescent sample consisted of  $6\ \mu\text{m}$ -diameter beads on a cover glass. We moved the objective arm to compensate for the different AO  $z$ -focusing levels to keep the same beads in focus. Red numbers show the  $z$  shifts required for refocusing. The maximal field of view was  $\approx 650\ \mu\text{m}$  at  $z = 0\ \mu\text{m}$  and beads remained visible in over a scanning range of  $1100\ \mu\text{m}$ . The  $z = 0$  was the nominal focal plane of the objective.

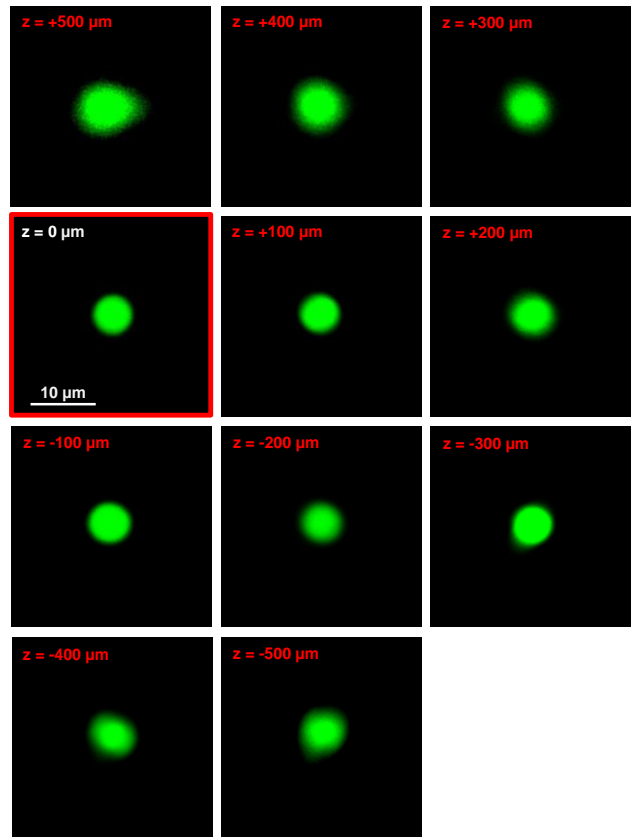


**Figure 26.** Image of a  $6\ \mu\text{m}$  diameter fluorescent bead at 880 nm. We moved the objective arm to compensate for the different AO  $z$ -focusing levels to keep the same bead in focus. Red numbers show the  $z$  shifts required for refocusing.

## 6.4 Continuous 3D Trajectory Scanning with AO deflectors

3D AO random-access point scanning is a powerful tool when we are measuring from acute brain slices or from an anesthetized animal, but faces two major technical limitations if we would like to measure from behaving animals

- i) fluorescence data are lost or contaminated with large amplitude movement artifacts during *in vivo* recordings; and
- ii) sampling rate is limited by the large optical aperture of AO deflectors, which must be filled by an acoustic wave to address a given scanning point.

The first issue occurs because the actual location of the recorded ROIs are continuously changing during *in vivo* measurements due to tissue movement caused by heartbeats, blood flow in nearby vessels, respiration, and physical motion<sup>47</sup>. This results in fluorescence artifacts because of the spatial inhomogeneity of the baseline fluorescence signal and in relative fluorescence changes. In addition, the amplitudes of motion-induced transients can even be larger than the ones induced by one or a few action potentials detected by genetically encoded calcium indicators (GECIs)<sup>40</sup>. Therefore it is difficult to separate post-hoc the genuine fluorescence changes associated with neural activity and the artifacts caused by brain movement. The second issue with 3D point-by-point scanning occurs because of the relatively long switching time (about 20-33  $\mu$ s) of AO crystals, which limits either the measurement speed or the number of ROIs. To achieve large scanning volumes with a high spatial resolution, we need large AO deflector apertures. However, to fill these large apertures with an acoustic signal takes considerable time. Therefore, the long-duration AO switching time slows down the scanning rate.

In order to achieve both high temporal and spatial sampling rates, we developed a new scanning approach, Continuous Trajectory Scanning. The fast *z*-scanning range of this method can be hundreds of microns, and there are no mechanical constraints which limit trajectory selection.

In order to implement the Continuous Trajectory Scanning approach, we first defined a 3D trajectory on which we would like to perform the fast trajectory scanning, the length, direction and speed along this scan-line is determined the measurement properties, but usually defined by using the 3D volume information from a *z*-stack of the region of

interest and manual selection of the ROIs. This trajectory is then divided up to guiding points according to the preset drift length. During scanning the laser is focused onto the first guide point, where the interpolation curve starts. Next, the focal point is forced to drift continuously in the  $x$ - $y$  plane in the direction of the interpolation curve (see below partial chirp compensation to evoke continuous lateral motion) until the distance between the center of the focal point and the interpolation curve exceeded 50% of the size of the PSF in the  $z$ -direction (**Figure 28**; **Figure 29**). Then the focal spot is stepped along the  $z$ -axis, in the direction of the interpolation curve, with a step size corresponding to the PSF size. From this new position, the drift-jump procedure is restarted and repeated until the end of the interpolation curve was reached (corresponding to the last guide point). The required drift velocity is determined by equations detailed in the next point. Finally, the raw fluorescence trace is spatially normalized before visualization (**Figure 27**). Although the jumps along the  $z$ -direction take the same time as the steps in the point-by-point scanning mode, by increasing the sampling rate of the detectors we were able to record with approximately tenfold higher spatial sampling rate during lateral drifting as compared to point-by-point scanning (595.2 points/kHz instead of 54.3 points/kHz). The PSF did not change during the lateral drift (**Figure 28**). The sequence of fast drifts in the  $x$ - $y$  direction and jumps in the  $z$ -direction allowed us to perform high speed and high spatial sampling along 3D trajectories.

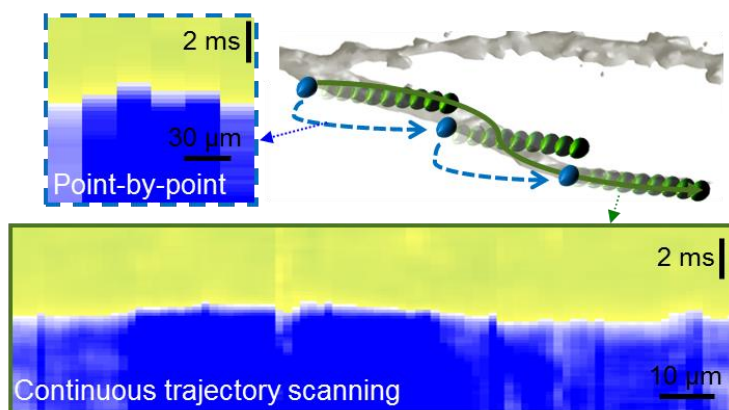


**Figure 27.** *3D trajectory scanning of dendritic  $Ca^{2+}$  spike propagation. Point-by-point and continuous 3D trajectory scanning of dendritic segments. Top right, schema of the scanning modes (blue point-by-point scanning; green, continuous scanning). Example of  $Ca^{2+}$  responses measured by point-by-point (top left) and continuous trajectory modes (bottom). Traces were spatially normalized.*

### 6.4.1 Moving the focal spot in 2D

Chirped acoustic wave with a counter-propagating differently chirped acoustic wave can result in continuous line-scanning with a given velocity in a given focal plane when the frequency slopes of the chirps of the focusing and counter-propagating AO waves are selected properly.

Briefly, the temporal variation of the deflected beam angle of the laser beam emerging from one AO deflector with a chirped acoustic sweep of slope ‘ $a$ ’ is described by the acousto-optic law<sup>14</sup>:

$$\frac{\partial \alpha}{\partial t} = K \cdot \frac{\partial f}{\partial t} = K \cdot a \quad (\text{Equation 14})$$

where  $K$  describes the dependence of the deflection angle  $\alpha$  on the acoustic frequency  $f$  in a given deflector:  $\alpha = K \times f$ . When this AO deflector is combined with a second AO deflector with counter-propagating chirped acoustic pulses, the subsequent optics with magnification  $M$  and the objective with effective focal length  $f_{obj}$  transform this angle variation into the lateral shift of the spot in the focal plane with velocity:

$$v = (K_2 a_2 - K_1 a_1) \cdot \frac{f_{obj}}{M} \quad (\text{Equation 15})$$

where  $a_1$  and  $a_2$  are the chirps of the focusing and the counter-propagating AO waves, in the first and second AO deflector, respectively, and  $K$  is different for the first ( $K_1$ ) and second deflectors ( $K_2$ ), because they have different configurations and geometries. The movement of the focal spot is restricted to a given  $z$ -plane if the slopes in a deflector pair are shifted symmetrically to maintain

$$K_2 a_2 + K_1 a_1 = \text{const} \quad (\text{Equation 16})$$

Our optical model determined the chirp parameters required, and these were confirmed in measurements on fluorescent beads.

The same is valid for both  $x$  and  $y$  direction of deflection. Thus, continuous scanning in any arbitrary direction with a given speed in each focal plane can be realized with small jumps along the  $z$  axis (continuous 3D trajectory scanning). When the velocity is set to zero we got back the random-access point scanning mode. We use a fairly simple method in the algorithm that determines the frequency sweep slopes, which cause the

spot to move in a plane at a prescribed  $z$  depth in the required direction with a prescribed velocity  $v$ . Our simulations and measurements have also shown that the spatial resolution does not change noticeably during the drift (**Figure 28**).

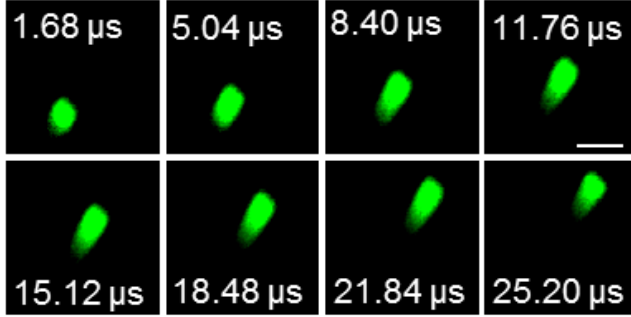


**Figure 28** Images of a fluorescent bead as the function of time in continuous trajectory scanning mode. Images of the same fluorescent bead at different time points during drift. The bead's image was elongated because the focal spot was moving during PMT integration. Scale bar,  $2 \mu\text{m}$ .

**Maintaining constant  $z$  at different drift velocities in continuous 3D trajectory scanning mode.** We use a fairly simple method in the algorithm that determines the frequency sweep slopes, which cause the spot to move in a plane to a predetermined  $z$  depth in the desired direction with a desired velocity  $v$ . The optical system was designed to produce zero astigmatism in the nominal focal plane; the astigmatism would increase nearly linearly with the  $\Delta z$  distance from this plane, if the slope values in the  $x$  and  $y$  deflectors are kept equal. However, the slope values are set to achieve zero or near zero astigmatism for any  $z = \text{const.}$  plane. The  $z$  value in the  $x$ - $z$  ( $z_x$ ) plane can be determined directly from the slopes in the respective deflectors:

$$z_x = \frac{M_x^2 f_{obj} \left( \frac{v_x}{K_{1x} a_{1x} + K_{2x} a_{2x}} \right)}{M_x^2 \left( \frac{v_x}{K_{1x} a_{1x} + K_{2x} a_{2x}} \right) + f_{obj}}, \quad (\text{Equation 17})$$

where  $M_x$  is the magnification in the respective planes.  $K_{1x}$  and  $K_{2x}$  represent the linear dependences of the deflection angles on the acoustic frequencies characteristic to the deflectors deflecting in the  $x$ - $z$  plane in the AO  $z$ -focusing unit and 2D-AO scanning unit, respectively.  $a_{1x}$  and  $a_{2x}$  are the acoustic frequency slopes in the same deflectors,  $f_{obj}$  is the focal length of the objective and  $v_x$  is the projection of spot velocity ( $v$ ) to the  $x$  axis. The same is valid for the  $y$ - $z$  ( $z_y$ ) plane. The zero astigmatism condition is:

$$z_x = z_y, \quad (\text{Equation 18})$$

Therefore, from **Equation 14 – Equation 17** the slope values  $a_{1x}$ ,  $a_{2x}$ ,  $a_{1y}$ ,  $a_{2y}$  can be determined for the required  $z_x = z_y$ ,  $v_x$ ,  $v_y$  values.

**PSF during continuous 3D trajectory scanning with AO deflectors.** In the continuous trajectory scanning method, the focal plane ( $z$ -depth) is constant during lateral drifting, and the optical system linking the scanner with the sample does not introduce additional optical errors to the focusing process. Since the AO  $z$ -focusing unit's deflectors are imaged onto the deflectors in the 2D scanner unit, and necessarily the  $x$ - $z$  and  $y$ - $z$  deflecting deflectors are not exactly at the same positions relative to the relaying telecentric lenses – the longitudinal sizes of the deflectors (10-30 mm) are not negligible relative to the length of the imaging system (~600 mm) – this imaging introduces astigmatism when  $z$  is increased in any direction from the nominal focal plane, or when the drift velocity in a given plane is increased. However, in the latter case, the slope differences between the consecutive deflectors must be increased almost symmetrically to maintain the focal plane constant, which means that an equal amount of slope shift with opposite sign should be applied to the deflector pairs operating in the  $x$ - $z$  and  $y$ - $z$  planes, respectively.

The symmetrical slope shift also helps to compensate successfully for the appearance of additional astigmatism by adding slightly different slopes to the  $x$ - $z$  and  $y$ - $z$  pairs.

For optimum operation, the sweep slope mismatch is optimized for minimal astigmatism in any  $z \neq 0$  plane, to obtain the best spot size and shape. Our simulations (**Figure 29**) confirm that, under these conditions, the spot parameters are not modified significantly during the drift.

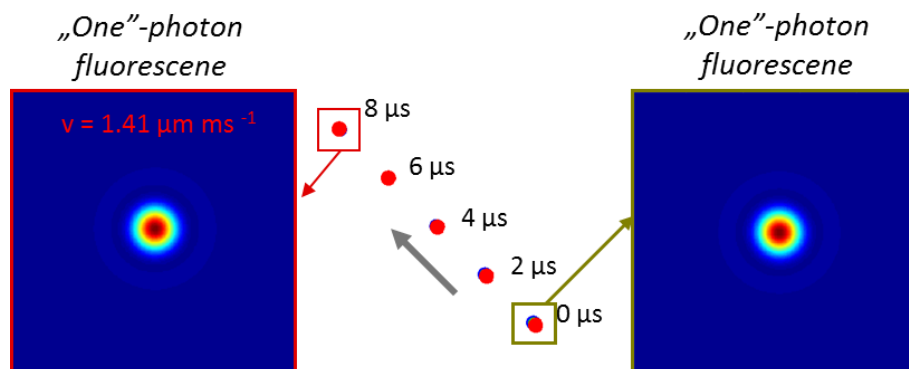


**Figure 29. Simulation of the PSF during drifting in the nominal focal plane in continuous 3D trajectory scanning mode. PSF did not change, even at very high velocity.**

The Strehl ratio only decreases with the distance from the optimum point (from the middle of the scanned volume) according to the rule valid for stationary focal spots.

The drifting of the focal spot was verified experimentally (**Figure 28** showing images of a 1  $\mu\text{m}$ -diameter fluorescent bead). The focal spot drifted along an oblique axis relative to the basic  $x$ - $y$  coordinates during the capture of each pixel of the image, while the PMT sampling rate was increased to sample fluorescence at 595.2/pixels kHz. Each panel in **Figure 28** shows an image formed from the samples at a constant relative time difference, measured from the beginning of pixel sampling (time difference values written on the panels). The different positions of the bead images on the different panels are due to the focal spot drifting at a high speed of about 170  $\mu\text{m}/\text{ms}$ . The elongation of the bead image in **Figure 28** is caused by the relatively long PMT sampling (1.68  $\mu\text{s}$ ) and integration time used in this measurement.

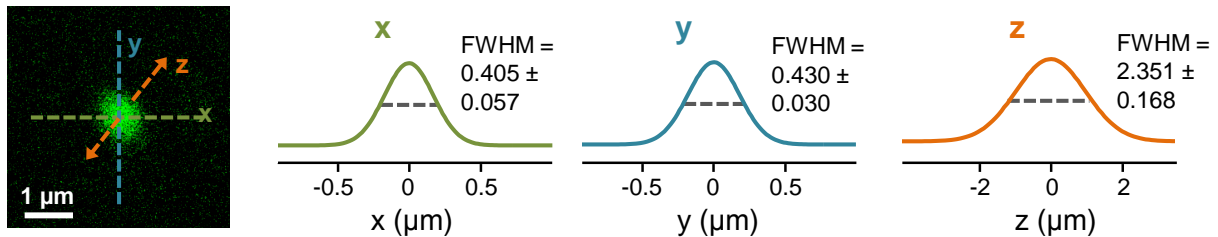


**Figure 30. Spatial resolution of the 3D DRIFT AO microscope. Left, fluorescent image of a 170 nm fluorescent bead with 3D DRIFT AO microscope. Right, average normalized fluorescence histograms along the  $x$ ,  $y$  and  $z$  axis for of  $n = 3$  beads. Resolution was determined as the full width at half maximum in every histogram (mean  $\pm$  SEM).**

#### 6.4.2 Moving the focal spot in 3D

In real biological samples the extent and motion induced movement of the regions of interest (somatas, dendrites or dendritic spines) are scarcely limited to two-dimensions. Especially when measuring *in vivo* cortical pyramidal cells, since their apical dendrites usually stretch perpendicular to the cortical surface. To extend the drift scan method from 2D to 3D we calculated the one-to-one relationship between the focal spot coordinates and speed, and the chirp parameters of the four AO deflectors, starting at any point in the scanning volume. For the optical calculation, we use a paraxial

approximation of the whole AO microscope applied in two perpendicular planes whose orientations are set by the deflection directions of the AO deflectors (**Figure 31**).

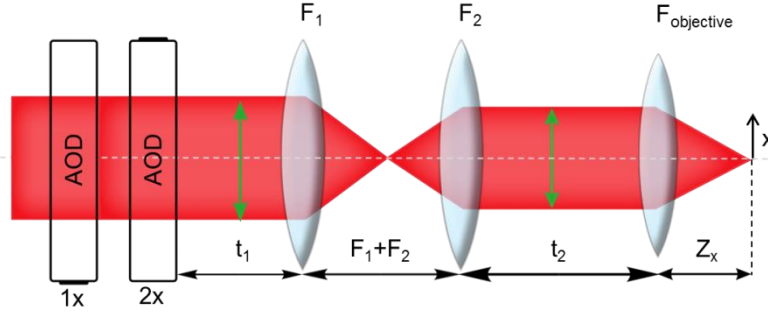


**Figure 31.** The optical geometry of the 3D focusing system used for calculating fast 3D drifts along arbitrary directions in space.

To calculate the driving signal for performing 3D drift along a predefined trajectory first we need the following three groups of equations:

**1**, the simplified matrix equation of the AO microscope in the x-z (and y-z) planes:

$$\begin{pmatrix} x_0 \\ \alpha_0 \end{pmatrix} = \mathbf{A} * \begin{pmatrix} x \\ \alpha \end{pmatrix} \quad (\text{Equation 19})$$

$$\mathbf{A} = \begin{pmatrix} 1 & z_x \\ 0 & 1 \end{pmatrix} \begin{pmatrix} 1 & 0 \\ -1/F_{obj} & 1 \end{pmatrix} \begin{pmatrix} 1 & t_2 \\ 0 & 1 \end{pmatrix} \begin{pmatrix} 1 & 0 \\ -1/F_2 & 1 \end{pmatrix} \begin{pmatrix} 1 & F_1 + F_2 \\ 0 & 1 \end{pmatrix} \begin{pmatrix} 1 & 0 \\ -1/F_1 & 1 \end{pmatrix} \begin{pmatrix} 1 & t_1 \\ 0 & 1 \end{pmatrix} \quad (\text{Equation 20})$$

$$\mathbf{A} = \begin{pmatrix} -\frac{F_2}{F_{obj}F_1}(F_{obj} - z_x), & F_1 + F_2 - (F_1 + F_2)\frac{z_x}{F_{obj}} - \frac{F_2 t_1}{F_1} - \frac{F_1 t_2}{F_2} - \frac{F_1 z_x}{F_2} + \frac{z_x}{F_{obj}} \left( \frac{F_2 t_1}{F_1} + \frac{F_1 t_2}{F_2} \right) \\ \frac{F_2}{F_1 F_{obj}}, & \frac{F_2 t_1}{F_1 F_{obj}} - \frac{F_1}{F_2 F_{obj}} (F_2 + F_{obj} - t_2) - \frac{F_2}{F_{obj}} \end{pmatrix} \quad (\text{Equation 21})$$

$$\mathbf{A} = \begin{pmatrix} -\frac{F_2}{F_{obj}F_1}(F_{obj} - z_x), & -\frac{F_1 z_x}{F_2} \\ \frac{F_2}{F_1 F_{obj}}, & -\frac{F_1}{F_2} \end{pmatrix} \quad (\text{Equation 22})$$

**2**, the basic equation of the AO deflectors:

$$\alpha = K * f \quad (\text{Equation 23})$$

where both  $\alpha$  and  $f$  are functions of time and the  $x$  coordinate.

**3**, temporally non-linear chirps for the acoustic frequencies in the deflectors deflecting in the x-z (and y-z) plane ( $f$ ):

$$f_i(x, t) = f_i(0,0) + (b_{xi} * (t - \frac{D}{2*v_a} - \frac{x}{v_a}) + c_{xi}) * (t - \frac{D}{2*v_a} - \frac{x}{v_a}) \quad (\text{Equation 24})$$

(where  $i=1$  or  $i=2$ , indicates the first and second x deflector;  $D$  the diameter of the AO deflector; and  $v_a$  is the propagation speed of the acoustic wave within the deflector)

Here we calculate everything in the x-z plane, where the x axis being the deflection direction of one AO deflector pair (y being that of the other) and z is the optical axis coinciding with the symmetry axis of the cylindrical objective. The same calculation should also be applied in the y-z plane. From these three groups of equations (**Equation 19 – Equation 24**) we can calculate the  $x_0$  coordinate of the focal spot. To have all rays focused on the focal point of the objective, the x- and  $x^2$ -dependent parts of the  $x_0$  coordinate must vanish (all rays starting at any x coordinate in the deflector aperture must pass through the same  $x_0$  coordinate in the focal plane), from which we can express the t dependence of the z coordinate:

$$z_x(t) = \frac{\frac{F_2}{F_1}}{\frac{F_2}{F_{obj}F_1} + K\frac{F_1c_{x1}+c_{x2}}{F_2v_a} + 2*K\frac{F_1b_{x1}+b_{x2}}{F_2v_a} * (t - \frac{D}{2v_a})} \quad (\text{Equation 25})$$

This equation has, however, a non-linear temporal dependence. Therefore, we need its Taylor series to simplify further calculations. Our simplest presumption was that for the linear part, time dependence will dominate over the quadratic part; therefore, the velocity along the z axis in the z-x plane is nearly constant ( $v_{zx}$ ):

$$v_{zx} = \frac{(-2K\frac{b_{x1}+b_{x2}}{v_a})}{\left(\frac{F_2}{F_{obj}F_1} + K\frac{F_1c_{x1}+c_{x2}}{F_2v_a} - 2*K\frac{F_1b_{x1}+b_{x2}}{F_2v_a} * \left(\frac{D}{2v_a}\right)\right)^2} \quad (\text{Equation 26})$$

and, using the above expressions, the velocity along the x axis ( $v_x$ ) can be evaluated as:

$$v_x(t) = \frac{dx_0(t)}{dt} = + \frac{2*K\frac{F_1b_{x1}+b_{x2}}{F_2v_a}}{\left(\frac{F_2}{F_{obj}F_1} + K\frac{F_1c_{x1}+c_{x2}}{F_2v_a} + 2*K\frac{F_1b_{x1}+b_{x2}}{F_2v_a} * \left(t - \frac{D}{2v_a}\right)\right)^2} * K * [f_{x1}(0,0) - f_{x2}(0,0) + \left(t - \frac{D}{2v_a}\right) * (c_{x1} - c_{x2})] - \frac{1}{\frac{F_2}{F_{obj}F_1} + K\frac{F_1c_{x1}+c_{x2}}{F_2v_a} + 2*K\frac{F_1b_{x1}+b_{x2}}{F_2v_a} * \left(t - \frac{D}{2v_a}\right)} * K * [(c_{x1} - c_{x2})] \quad (\text{Equation 27})$$

In the last step we want to analyze the motion of the focal spot along different 3D trajectories. For simplicity, we calculate the drift along a general 3D line with an arbitrary velocity and an arbitrary angle relative to the axes. The x-z and y-z planes can

be treated separately as above. In the x-z plane we can express the projection of the 3D line as:

$$z_x(t) = z_0(0) + \frac{v_{zx0}}{v_{x0}} * x_0(t) - \frac{v_{zx0}}{v_{x0}} * x_0(0) \quad (\text{Equation 28})$$

When we combine the expression  $z_x(t)$  with  $x_0(t)$ , the similarly calculated  $z_y(t)$ , and  $y_0(t)$ , and add all the required initial positions ( $x_0, y_0, z_0$ ) and speed parameter values ( $v_{x0}, v_{y0}, v_{zx0} = v_{zy0}$ ) of the focal spot, we can determine all the parameters required to calculate the non-linear chirps according to **Equation 24** in the four AO deflectors ( $\Delta f_{0x}, b_{x1}, b_{x2}, c_{x1}, c_{x2}$  and  $\Delta f_{0y}, b_{y1}, b_{y2}, c_{y1}, c_{y2}$ ). Note that  $\Delta f_{0x}$  and  $\Delta f_{0y}$  are not fully determined; here we have an extra freedom to select from frequency ranges of the first ( $f_1$ ) and second ( $f_2$ ) group of AO deflectors to keep them in the middle of the bandwidth during 3D scanning. In summary, we were able to derive a one-to-one relationship between the focal spot coordinates and speed and the chirp parameters of the AO deflectors. Therefore, we can generate fast movement along any 3D line, starting at any point in the scanning volume.

### 6.4.3 Fast 3D DRIFT AO microscopy

During these fast 3D drifts of the focal spot, the fluorescence collection is uninterrupted, lifting the pixel dwell time limitation of the previously used point scanning. Scanning speed can be up to 10 mm/ms along any segments of any 3D lines situated in any location in the entire scanning volume with minimal loss of resolution at high speeds (see

**Figure 32** for details).

In this way, fluorescence information can be continuously collected when scanning the entire 3D line in the same short period of time ( $\approx 20 \mu\text{s}$ ) as this is required for single-point scanning in the point-by-point scanning mode. The data acquisition rate is limited only by the maximal sampling rate of the PMT units. Therefore, we can generate folded

surface (or volume) elements. For example from transversal or longitudinal 3D lines (

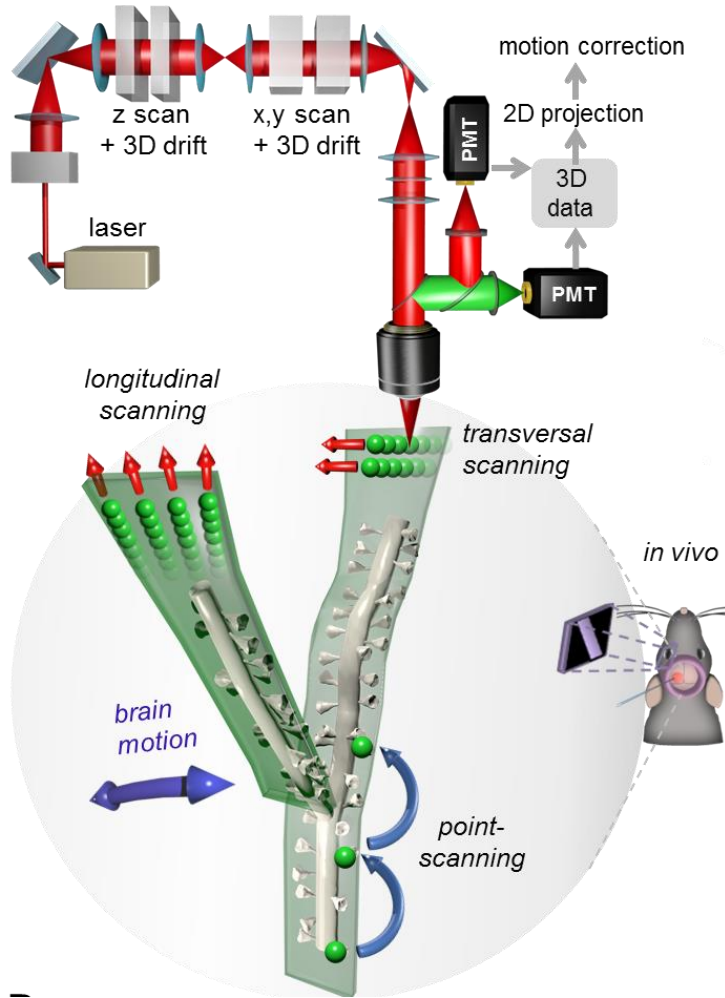
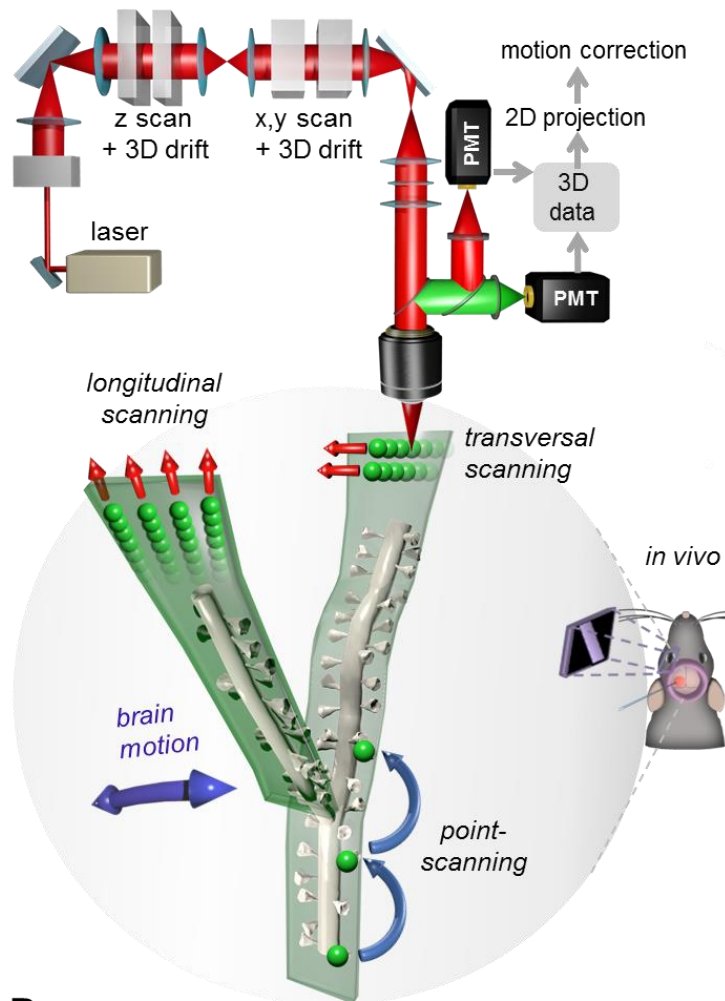


**Figure 33**), we can fit them to long, tortuous dendrite segments and branch points in an orientation which minimizes fluorescence loss during brain motion (3D ribbon



scanning, —

**Figure 33**), and image them at high speed.

Using 3D DRIFT AO microscopy we can extend the pre-selected individual scanning points to small 3D lines, surfaces, or volume elements to cover not only the pre-selected ROIs but also the neighboring background areas or volume elements while utilizing an increased data sampling rate.

Therefore, we can preserve fluorescence information from the pre-selected ROIs during 3D measurements even in the brain of behaving animals, while maintaining the 10-1000 Hz sampling rate necessary to resolve neural activity at the individual ROIs. demonstrated that these techniques can decrease the amplitude of motion artifacts by more than one order of magnitude and, therefore, enable the fast functional measurement of neuronal networks at the level of tiny neuronal processes, such as spiny

dendritic segments, even in head-restrained, behaving animals in a z-scanning range of more than 650  $\mu\text{m}$  in 3D even under conditions when large-amplitude motion artifacts are generated by physical movement.

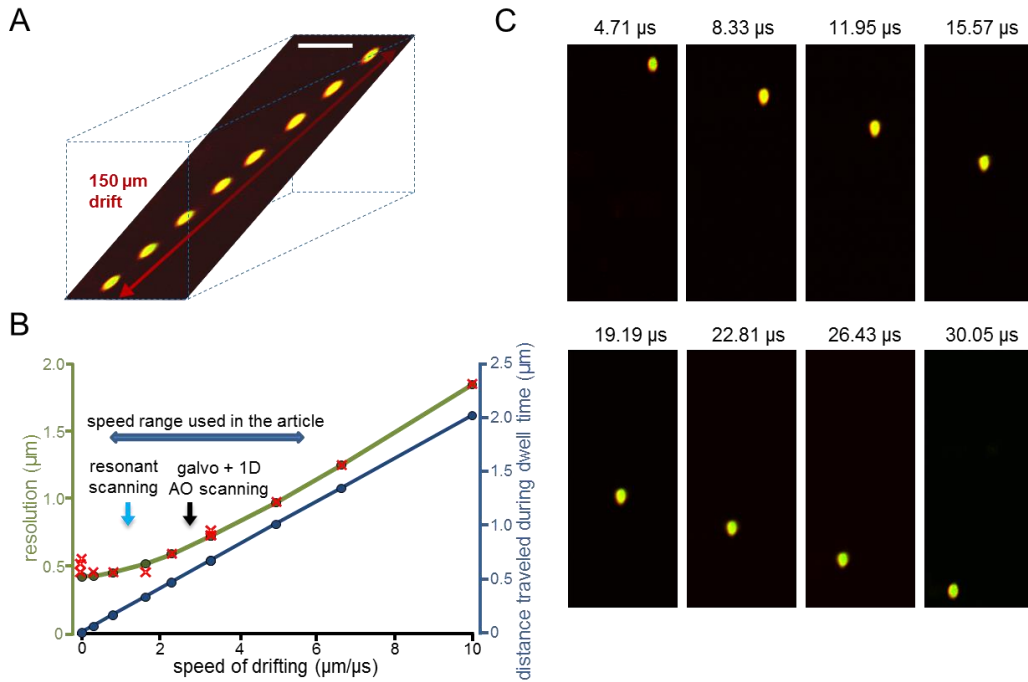


**Figure 32. Effect of fast 3D AO drifts on the size of the PSF.** 3D AO drifts were generated with up to 10  $\mu\text{m}/\mu\text{s}$  speed in different directions to analyze elongation of the PSF. (A) Maximal intensity projection image of a 6  $\mu\text{m}$  fluorescent bead during 3D DRIFT AO scanning. Images of the fluorescent beads at different time points were overlaid. The 3D AO drift was generated with 4.55  $\mu\text{m}/\mu\text{s}$  speed. (B) FWHM of the PSF along the direction of the fast drift as a function of the speed of 3D drifts (green line). Note the increasing PSF at higher speeds. FWHM along the perpendicular direction did not change. This blurring effect of the PSF can be explained by the movement within the pixel dwell time (blue line). The blue arrow indicates the maximal scanning speed of the typical resonant galvo system (see for example Varga et al., 2011). The black arrow indicates the scanning speed of a typical 2D system with one integrated AO deflector (see for example Chen et al., 2012). (C) Maximal intensity projection image of a 6  $\mu\text{m}$  fluorescent bead with 3D DRIFT AO scanning at different time points.

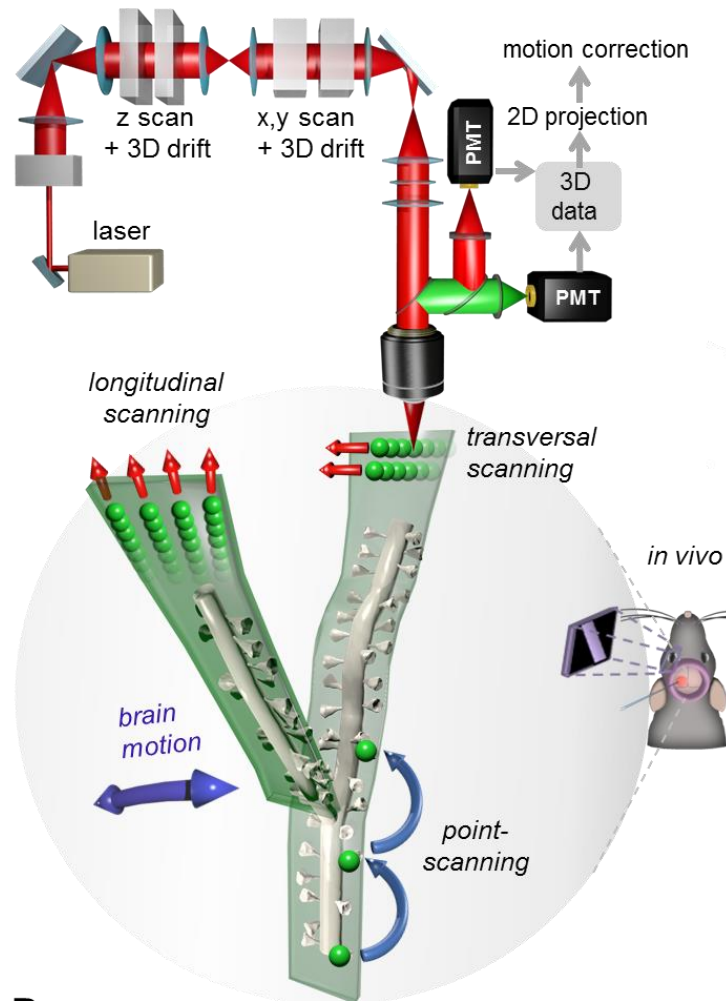


**Figure 33. Schematic of the *in vivo* measurements performed with 3D DRIFT AO microscopy.** In contrast to traditional point-by-point scanning, here the z scanning and x, y scanning units of the microscope can drift the focal spot in 3D in an arbitrary direction and with an arbitrary speed. Therefore, we can extend individual scanning points to a small surface or even volume elements by using, for example, longitudinal or transverse scanning. These surface and volume elements can be set parallel to the average direction of brain movement to preserve fluorescence information for motion correction, even in behaving animals.

## 6.5 Correction for the motion instabilities

In this chapter I will summarize in more detail the sources of motion mentioned in the previous chapters. These motions have multiple sources of motions when we are performing single point laser scanning imaging of *in vivo* or *in vitro* samples. Also all of these movements have different spatial and temporal characteristic; thus we need different compensation method for each of them. I will follow the path of the light during the detailed description of the different artefact sources and then detail the solutions we developed for compensation of these effects.

### 6.5.1 Beam stabilization

The first source of the instability is the optical elements' sensitivity to thermal drift (mechanical hysteresis of the compartments caused by the daily temperature drift in the lab), humidity fluctuation (increasing the mechanical hysteresis), long term change in the stability of the optical elements and change is the laser output pulse shape, mainly in its divergence. Unfortunately, even with the top quality laser sources in the market – MaiTai HP or Chameleon Ultra – we observed a modest change in the laser beam position and in the beam's divergence, which could cause a detectable error in the output power for such a sensitive optical configuration as an AO microscope. One possible explanation to this that these devices only have laser stability controlled in a single point, which is only enough to maintain stable laser position, but the angle of the output beam can still change slightly. Although this error is in the range of milliradians, the lightpath of the AO microscope is around 10 meters long and contains more than one hundred optical elements, including the AO crystals that are extremely sensitive to the incident light angle, so even this small instability causes detectable error. As a result of this, in our system, long term, precise beam stabilization can be secured only by active beam alignment. The recent optical lightpath contains two steps of beam stabilization, the first one directly after the laser source, the second right before the light is coupled in the optical scan head. Each section of the beam stabilization unit consist of beam samplers, allowing a small portion (~0.1%) of the beam to the surface of the quadrant detectors and motorized mirrors which are aligning back the laser pulse if disposition is detected on the quadrant detector.

I designed the actuation software in Labview. The control loop consists of a single 'For' loop continuously measuring the position of the beams on all four quadrant detectors. If misalignment is noticed at any of the detectors, the motorized mirrors are driven to the desired direction according to a predefined sequence. If the intensity suddenly drops at the detectors (caused for example by sudden shut down of the laser) then the actuation circle automatically stops.

By designing the control program in loops instead of "If" functions the computation time reduced and the frequency of the stabilization is around 100 Hz. The position stability of the beam after the second stabilization cycle is under 1 milliradian. At that point the laser beam is 15 mm wide, thus the error was so small that I cannot determine the amount more precisely than that. I have also tested the effect of the beam stabilization precision by turning off the feedback loop and setting the error of the position to be three time larger than the threshold of the automatic feedback. Even at that position of the beam there was no detectable degradation of the resolution or laser energy under the objective. The only possible final source of misalignment could be only the mechanical displacement caused by the thermal drift of the detectors, but I have not experienced long term instability which could be caused by this effect. Probably because even if such displacement occurs it should have different extend and time scale for the four quadratic detectors, thus they are also compensating for each other's errors.

Thus we assumed that the two steps of stabilization coupled with the fast control loop are sufficient to correct for all errors caused by the instability of the optical elements.

### **6.5.2 Automatic drift compensation algorithm**

With the beam position fully stabilized there still can be a mechanical drift at the level of the sample itself, caused by thermal or biological drift. The main technical sources of this drift can be the following:

- Stability problems or thermal drift of the sample chamber or animal holder.
- Thermal fluctuation of the animal heating plate. – Most of the regulated heating pads works with a closed loop control system, thus repeatedly changes its temperature, it heats up the plate until reaches a certain high threshold, than

turns of until it cools down to the lower threshold. In some cases and with some holder this effect can be visible even at the sample level.

- Floating or drifting of the brain slice.

It can be also caused by biological effects:

- Swelling of the brain in *in vivo* preparation
- Degradation of the brain slice in *in vitro* preparation

To perform the drift compensation first we selected a reference cell or object and scanned it in 3D (**Figure 34**). The reference point cell should be an object with relatively stable fluorescence, that can be for example a fluorescent bead injected in the brain, or a bright cell with stable fluorescence, for example a cell labeled with a structure dye or protein (SR-101, mCherry, etc.), or an overexpressed GCaMP6 labeled cell which in practice usually shows no calcium responses over a certain level of labeling. We defined the 3D origin [(0, 0, 0) coordinate] of our recording as the center of this cell. To compensate for tissue drift, we rescanned the “origin-cell” and, using the profiles of the scan, we localized its center. We repositioned the center of the origin-cell to the (0, 0, 0) coordinate by moving the motorized shifting table (for XY compensation) and the objective (for Z compensation); this way all cells were shifted back to the (microscope-fixed) 3D location where they were selected for measurement. This tissue drift compensation was automated and performed after each plane when obtaining a reference z-stack, or between 3D random-access scans.

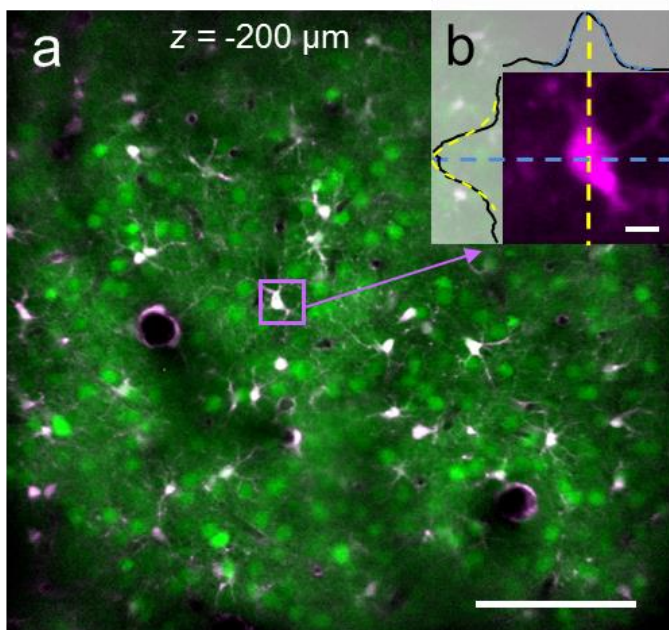


**Figure 34. Automatic drift compensation.** (a) Example of an image plane at 200  $\mu\text{m}$  depth showing neurons (green) and glial cells (magenta and white). Scale bar, 100  $\mu\text{m}$ . (b) Image and intensity profiles of a pre-selected bright glial cell used to establish the coordinate system. Scale bar, 5  $\mu\text{m}$ .

To test the performance of the drift scanning method I determined the largest residual error, or in another word, the largest non-compensated tissue displacement. For this I tested the algorithm during real experimental conditions where I have measured the same animal over several hours, and, as during a regular measurement, compensated for the slow tissue drift in every 4 minute, that is the time needed to run the eight different moving grating stimulation at different directions, and regularly we run a compensation cycle after a set of these stimulations. Then I extracted the shifts that should be made during this compensation cycles. The largest coordinate shift for compensation in this representation shows the largest non-compensated error, since that is the largest displacement of the measurement points right before we run the compensation cycle. As it can be seen in **Figure 35** the largest displacement I found was around 2.7  $\mu\text{m}$  at the XY plane. This is much smaller than the size of a soma, so during the whole measurement that should not affect our result significantly.

However if we measure smaller structures, or measure subregions of the somata, this displacement is larger that we should accept. There are two solutions to this problem. Either we can run the compensation cycle after every measurement unit, that is decreasing the residual error to 1.1  $\mu\text{m}$ , but that can still be large and also that would sufficiently increase our measurement time. The second option is to measure a small regions (which is at least 3  $\mu\text{m}$  large) around the region of interest and use online of offline motion correction methods to compensate for this error using this spatial information. This second option will be detailed in the next chapters.

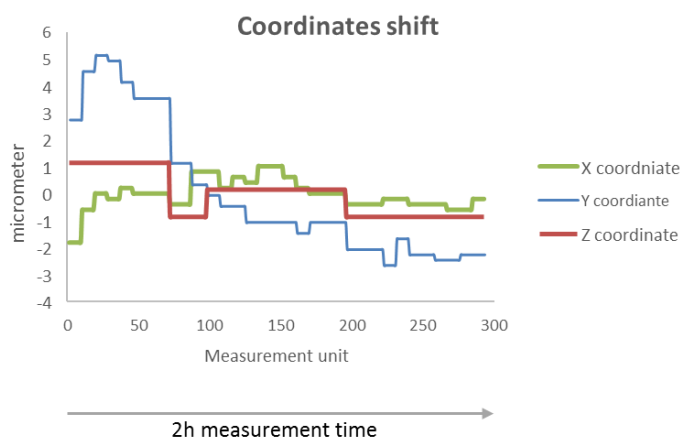


*Figure 35. Demonstratory displacements during a long in vivo measurement. Different colors show the displacement that had to be compensated along the three axes, Each measurement unit was around 30s long.*

### **6.5.3 Offline motion correction using AO DRIFT scanning**

The third source of motion is coming directly from the sample. For example in the case of *in vivo* measurement, respiration, locomotion and heart beat all cause motion of the brain even with precise surgery and stabilization of both the optical pathway and the headholder. Usually this movements occurred by the motion of the brain relative to the skull, so cannot be better stabilized with better surgery technique. Compensation of this artifact can be performed as the combination of AO DRIFT scanning detailed in the previous chapter, which allows us to measure small surface or volume elements around out region of interest coupled with offline motion correction algorithms, applied during post processing of the measurement's data since spatial information is available for this compensation. These surface and volume elements can be drawn around our ROIs depending on the details and to scope of the measurement, for example the extend or inhomogeneity of the movements.

## 6.6 Scanning methods for motion correction

Here I will demonstrate six new scanning methods based on 3D DRIFT AO scanning for *in vivo* measurements. For all six the basic concept is to measure a portion of the surrounding background area, so we have the information acquired even if its moved to this given area. These methods are 3D ribbon scanning; multi-3D line scanning; snake scanning; multi-layer, multi-frame imaging; chessboard scanning; and multi-cube scanning. They are differing the size and shape of the scanning field, so the shape of the background area we are recording besides the ROIs, thus each of them is optimal for a different neurobiological aim. For example, the first three are optimal for different dendritic measurements while the last two are best for somatic recordings; the surface scanning methods are optimized for speed while the methods based on volume imaging are optimized for large amplitude movements. Volume or area scanning used in these methods allows motion artifact correction on a fine spatial scale and, hence, the *in vivo* measurement of fine structures in behaving animals.

### 6.6.1 3D ribbon scanning to compensate *in vivo* motion artifacts

To achieve 3D ribbon scanning, the first step is to select guiding points along a dendritic segment (or along any cellular structure) based on the z-stack taken at the beginning of the experiment. The second step is to fit a 3D trajectory to these guiding points using piecewise cubic Hermite interpolation. We can use two main strategies to form ribbons along the selected 3D trajectory: we can generate drifts either parallel to the trajectory (longitudinal drifts), or orthogonal to the trajectory (transverse drifts) (**Figure 36**). In both cases, we chose to maximize how parallel these surface elements lie to the plane of brain motion or to the nominal focal plane of the objective. The basic idea behind the latter is that the point spread function is elongated along the z axis: fluorescence measurements are therefore less sensitive to motion along the z axis. Therefore, we can also follow this second strategy and generate multiple x-y frames for neuronal network and neuropil measurements.

To demonstrate 3D ribbon scanning we labeled a small number of pyramidal neurons in the V1 region of the visual cortex with a  $\text{Ca}^{2+}$  sensor, GCaMP6f, using an AAV vector for delivery. Then, according to the z-stack taken in advance, we selected guiding points

and fitted the 3D trajectory which covered a spiny dendritic segment of a labeled pyramidal cell. (**Figure 36A**)

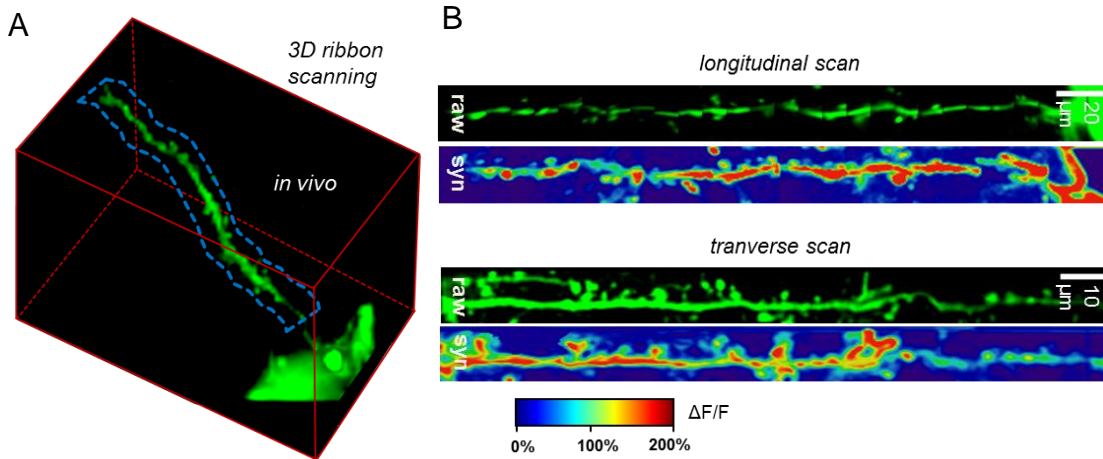


**Figure 36. Drift scanning methods.** (A) 3D image of a dendritic segment of a selected GCaMP6f-labeled neuron. Cre-dependent GCaMP6f-expressing AAV vectors were used to induce sparse labeling. A 3D ribbon (blue dashed lines) was selected for fast 3D DRIF scanning within the red cuboid. (D) Fast 3D ribbon scanning was performed at 139.3 Hz and 70.1 Hz along the blue ribbon indicated in C using either the longitudinal (left) or the transversal (right) scanning modes, respectively. Raw fluorescence data (raw) were measured along the selected 3D ribbon and were projected into 2D along the longitudinal and transversal axes of the ribbon following elimination of motion artifacts. Average  $\text{Ca}^{2+}$  responses along the ribbon during spontaneous activity (syn.) are color-coded.

We used transversal drifts to scan along the selected 3D ribbons to measure the selected 140  $\mu\text{m}$  dendritic segment and spines at 70.1 Hz (**Figure 36B**). Using longitudinal drifts allowed a much faster measurement (between 139.3 Hz and 417.9 Hz) of the same dendritic segment because fewer (but longer) 3D lines were required to cover the same ROI. In the next step, 3D recorded data were projected into 2D as a function of perpendicular and transverse distances along the surface of the ribbon. Note that this way, the dendritic segment was straightened to a frame (**Figure 36B**) to record its activity in 2D movies. This projection also allowed the use of an adapted version of previous methods developed for motion artifact elimination in 2D scanning<sup>47,54</sup>.

### 6.6.2 Recording of spiny dendritic segments with multiple 3D ribbon scanning

It has been reported that for many cortical neurons, synaptic integration occurs not only at the axon initial segment but also within the apical and basal dendritic tree<sup>7,55,56,57</sup>.

Here, dendritic segments form non-linear computational subunits which also interact with each other, for example through local regenerative activities generated by non-linear voltage-gated ion channels<sup>5,58,59</sup>. However, in many cases, the direct result of local dendritic computational events remains hidden in somatic recordings<sup>7,57,60</sup>. Therefore, to understand computation in neuronal networks we also need novel methods for the simultaneous measurement of multiple spiny dendritic segments. Although previous studies have demonstrated the simultaneous recording of multiple dendritic segments under *in vitro* conditions<sup>14,54</sup>, *in vivo* recording over large z-scanning ranges has remained an unsolved problem because the brain movement generated by heartbeat, breathing, or physical motion has inhibited the 3D measurement of these fine structures. Therefore, we implemented 3D ribbon scanning to simultaneously record the activity of multiple dendritic segments (**Figure 37**).

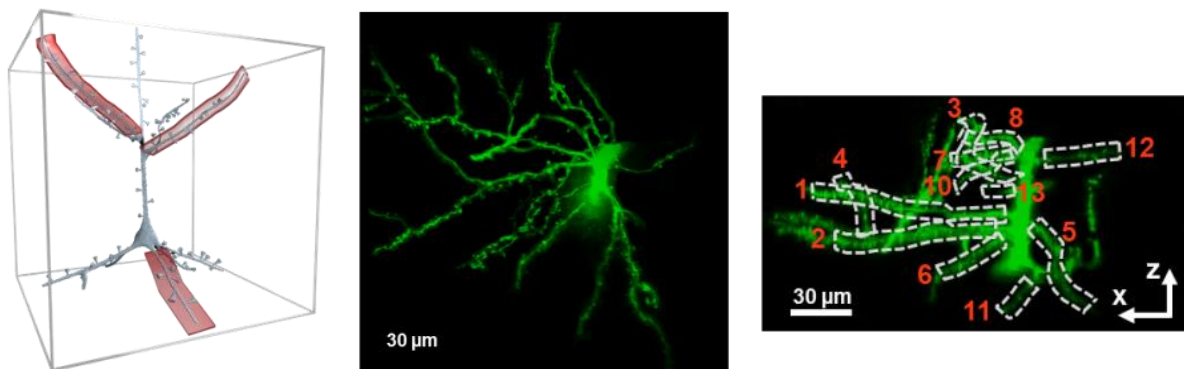


**Figure 37. Imaging of multiple spiny dendritic segments with 3D ribbon scanning in behaving animals. Schematic of the measurement.** (right) Schematic of the measurement alignment. (middle) Maximal intensity projection in the *x-y* and *x-z* planes of a GCaMP6f-labeled layer II/III pyramidal neuron. (right) White numbered frames indicate the twelve 3D ribbons used to simultaneously record twelve spiny dendritic segments using 3D ribbon scanning.

As in the 3D measurement of single dendritic segments, we took a z-stack in advance, selected guiding points in 3D along multiple dendritic segments, and fitted 3D trajectories and, finally, 3D ribbons to each of the selected dendritic segments (**Figure 37**). As above, the surface of the ribbons was set to be parallel to the average motion vector of the brain to minimize the effect of motion artifacts. We selected 12 dendritic segments from a GCaMP6f-labeled V1 pyramidal neuron for fast 3D ribbon scanning.

In the next step, 3D data recorded along each ribbon were 2D projected as a function of distance perpendicular to the trajectory and along the trajectory of the given ribbon. Then, these 2D projections of the dendritic segments were ordered as a function of their length and were placed next to each other. Note that, in this way, all the dendritic segments are straightened and visualized in parallel. In this way we were able to transform and visualize 3D functional data in real-time as a standard video movie. The 2D projection used here allows fast motion artifact elimination and simplifies data storage, data visualization, and manual ROI selection (**Figure 37**).

Since each ribbon can be oriented differently in 3D space, the local coordinate system of measurements varies as a function of distance along a given ribbon, and also between ribbons covering different dendritic segments. To resolve this issue we needed a motion compensation method that is taking in account not only the displacement calculated from the recorded videos but also the position of this segment in the original 3D space. I will detail this method in section **6.6.8**.

For the measurement on **Figure 37** we repeated the algorithm separately in each and every segment to let the algorithm correct for local inhomogeneity in displacement. This allowed, for example, the depth-, vasculature-, and distance-dependent inhomogeneities in displacement to be eliminated. After motion correction we could reveal the activity from over 130 spines and dendritic regions from this experiment and detected spontaneous and visual stimulation-induced activities (**Figure 38**).

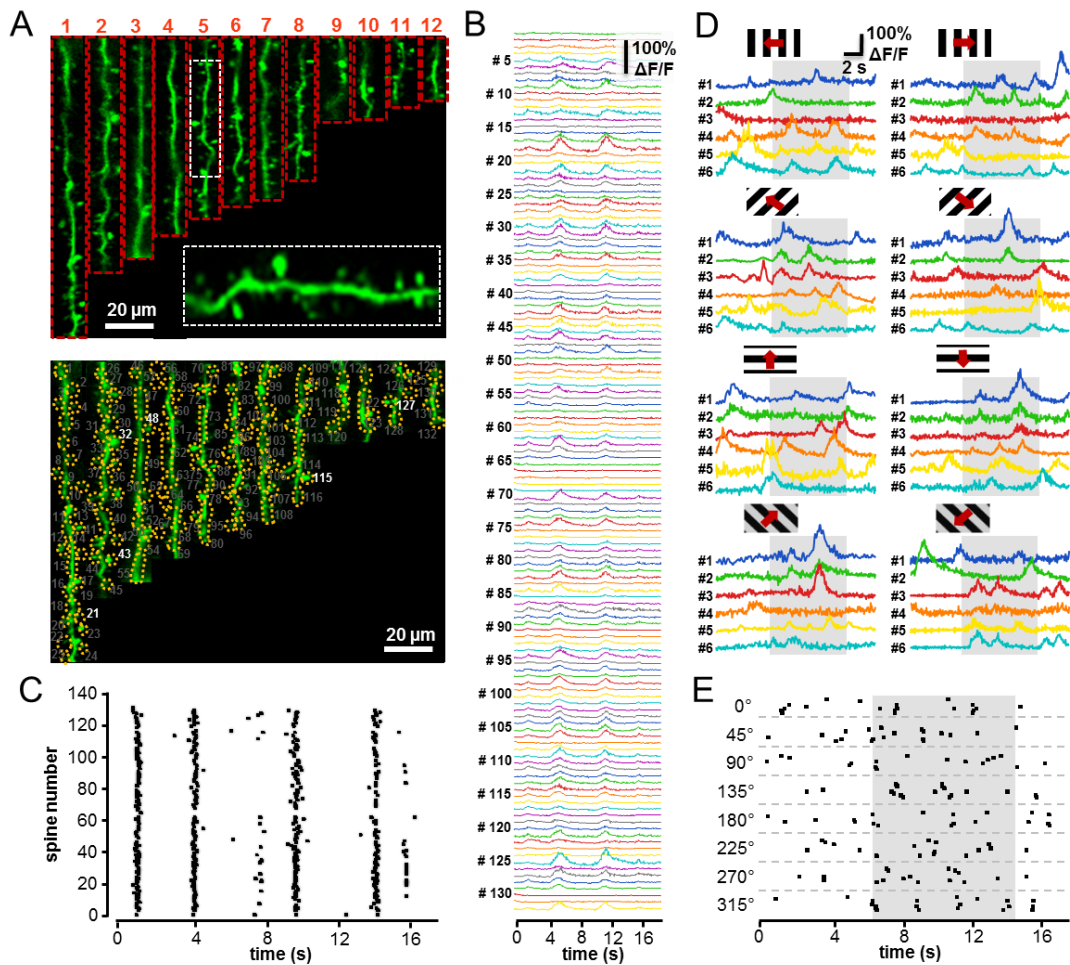


**Figure 38. Imaging of multiple spiny dendritic segments with 3D ribbon scanning in behaving animals.** (A) Top, fluorescence was recorded simultaneously along the 12 dendritic regions measured. (Same 12 segments shown in **Figure 37**.) Fluorescence data were projected into a 2D image as a function of the distance along the longitudinal and transverse directions of each ribbon, then all images were ordered next to each other. This transformation allowed the simultaneous recording, successive motion artifact elimination, and visualization of the activity of the 12 selected dendritic regions as a 2D movie. The image is a single frame from the movie recorded at 18.4 Hz. Inset, enlarged view of dendritic spines shows the preserved two-photon resolution. Bottom, numbers indicate 132 ROIs: dendritic segments and spines selected from the video. (B)  $Ca^{2+}$  transients derived from the 132 numbered regions indicated in A. (C) Raster plot of activity pattern of the dendritic spines indicated in C. (D)  $Ca^{2+}$  transients from the six exemplified dendritic spines indicated with white numbers in A. Transients were induced by moving grating stimulation. Note the variability in spatial and temporal timing of individual spines. (E) Raster plot of the activity pattern of the six dendritic spines from F. Time of moving grating stimulation in eight different directions is indicated with a gray bar.

### 6.6.3 Multi-layer, multi-frame imaging of neuronal networks: chessboard scanning

To understand neuronal computation, it is important to record not only assemblies of spines and dendrites, but also populations of somata. Random-access point scanning is a fast method which provides good SNR for population imaging in *in vitro* measurements and in anesthetized mouse models<sup>2,14,34</sup>. However, motion artifacts are generated when using point scanning during recording in awake, behaving animals, for two reasons. First, the amplitude of motion artifacts is at the level of the diameter of the soma. Second, baseline and relative fluorescence is not homogeneous at the soma, especially when GECIs are used for labeling. Therefore, we need to detect fluorescence information not only from a single point from each soma, but also from surrounding the area, in order to preserve somatic fluorescence information during movement. To achieve this, we extended each scanning point to small squares (and, in other sets of measurements below, to small cubes). We can use the two main strategies described above to set the orientation of squares to be optimal for motion correction: namely, we can set the squares to be either parallel to the direction of motion, or to be parallel to the nominal focal plane of the objective (**Figure 39A**). This second strategy will be demonstrated here. Similarly to 3D ribbon scanning, we can generate a 2D projection of the 3D data during multi-layer, multi-frame recording, even during image acquisition, by simply arranging all the squares, and hence each soma, into a “chessboard” pattern for better visualization and movie recording (this version of multi-layer, multi-frame imaging is called “chessboard” scanning, **Figure 39B**).

Similarly to the 3D ribbon scanning, here we calculated the average brain displacement vector as a function of time, and subtracted it from all frames to correct motion artifacts. Finally, we could select sub-regions from the 2D projection and calculate the corresponding  $\text{Ca}^{2+}$  transients as above (**Figure 39C and D**) and detect orientation- and direction-sensitive neurons with moving grating stimulation (**Figure 40**).

Chessboard scanning combines the advantage of low photo-toxicity of low-power temporal oversampling (LOTOS)<sup>15</sup> with the special flexibility of the 3D scanning capability of AO microscopy by allowing simultaneous imaging along multiple small frames placed in arbitrary locations in the scanning volume with speeds exceeding than resonant scanning.

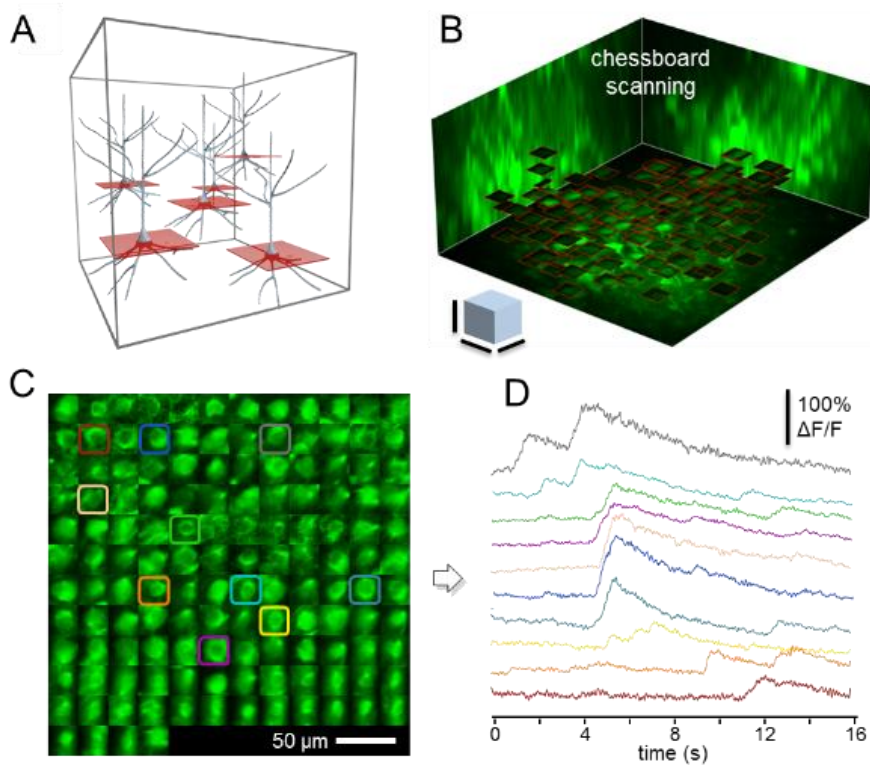


**Figure 39. Chessboard scanning of dendritic activity of a layer V pyramidal neuron in behaving animals.** (A) Schematic of chessboard scanning. (B) Neurons from a mouse V1 region were labeled with GCaMP6f sensor. Neuronal somata and surrounding background areas (small horizontal frames) were selected according to a z-stack taken at the beginning of the measurements. Scale bars 50  $\mu\text{m}$ . (C) Selected frames are “transformed” into a 2D “chessboard”, where the “squares” correspond to single somata. Therefore, the activity can be recorded as a 2D movie. The image is a single frame from the video recording of 136 somata during visual stimulation. (D) Representative somatic  $\text{Ca}^{2+}$  responses derived from the color-coded regions in C following motion-artifact compensation.



**Figure 40. Raster plot of average  $\text{Ca}^{2+}$  responses induced with moving grating stimulation into eight different directions from the color-coded neurons shown in Figure 39.**

#### 6.6.4 Multi-layer, multi-frame imaging of long neuronal processes

Multi-layer, multi-frame scanning can also be used to measure neuronal processes (Figure 41A). Because the total z-scanning range with GECIs was extended to over 650  $\mu\text{m}$ , we can, for example, simultaneously image apical and basal dendritic arbors of

layer II/III or V neurons, or follow the activity of dendritic trees in this z-scanning range. To demonstrate the large dendritic imaging range, we selected a GCaMP6f-labeled layer V neuron from a sparsely labeled V1 network (**Figure 41B**). Visual stimulation-induced dendritic and somatic  $\text{Ca}^{2+}$  responses were simultaneously imaged at 30 Hz in multiple frames situated at 41 different depth levels over a 500  $\mu\text{m}$  z range in an awake animal (**Figure 41C**). Motion artifacts along the x and y axes were eliminated from frames as above by subtracting the time-dependent net displacement vector. Finally, we derived the  $\text{Ca}^{2+}$  transients for each ROI (**Figure 41D**).

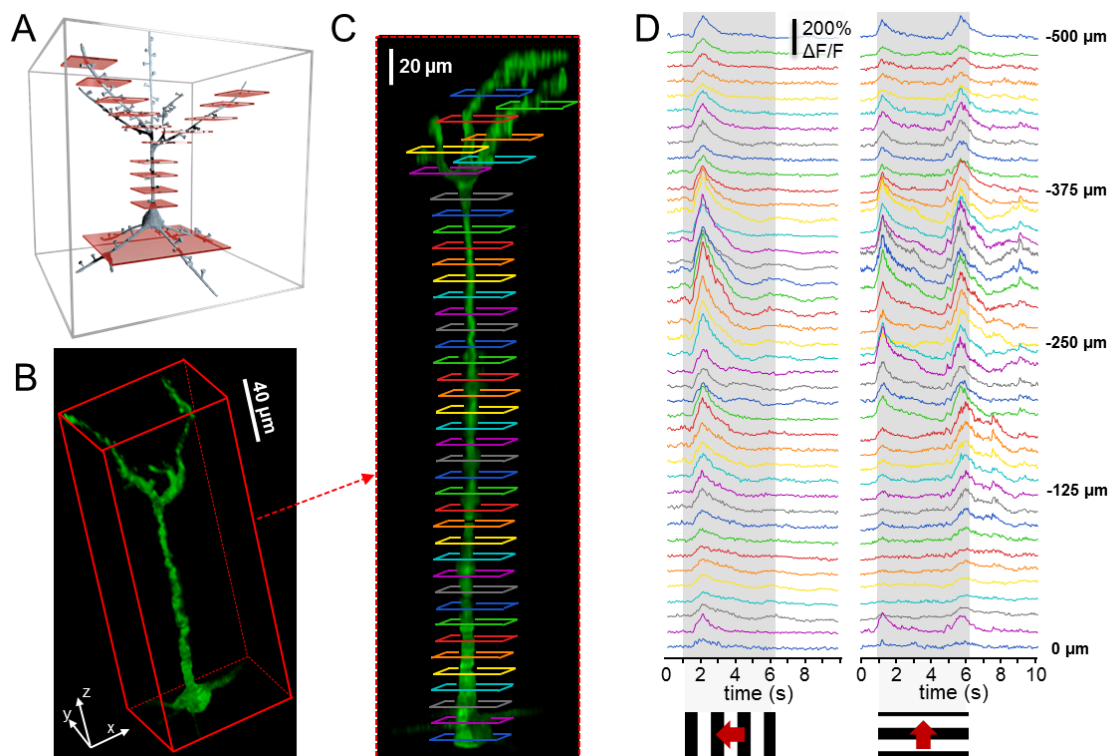


**Figure 41. Multi-layer, multi-frame imaging of dendritic activity of a layer V pyramidal neuron in behaving animals.** (A) Schematic of the measurements: multiple frames of different sizes and at any position in the scanning volume can be used to capture activities. (B) A GCaMP6f-labeled layer V pyramidal neuron selected for the measurements. (C) Side view of the neuron shown in G. Color-coded frames indicate the position of the simultaneously imaged squares. (D)  $\text{Ca}^{2+}$  transients calculated from the color-coded frames indicated in G are shown following motion correction with subpixel resolution. Transients were induced by moving gratings stimulation in time periods shown in gray.

Naturally, the multi-layer, multi-frame scanning method is not limited to a single dendrite of a single neuron, but rather we can simultaneously image many neurons with their dendritic (or axonal) arbor. To show this, we selected four layers of neuropil

labeled with the GCaMP6f sensor using a nonspecific AAV vector, and recorded activity at 101 Hz simultaneously in four layers (Figure 42). Following motion artifact elimination, the relative fluorescence changes were overlaid on the background fluorescence images (Figure 42D). To show an alternative quantitative analysis, we also calculated  $\text{Ca}^{2+}$  transients (Figure 42C) from some exemplified somatic and dendritic ROIs (Figure 42B).

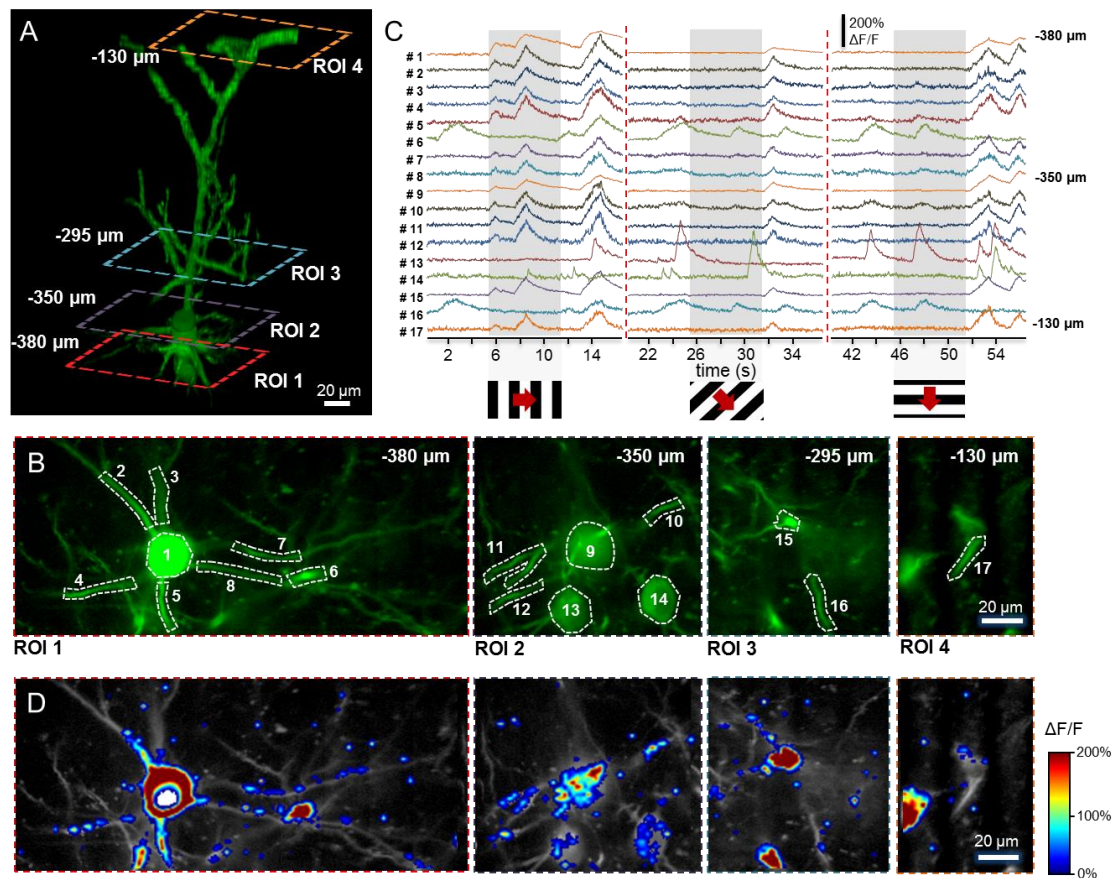


**Figure 42 Multi-layer imaging of layer II/III pyramidal neurons and their dendritic arbor during visual stimulation.** (A) 3D view of a layer II/III neuron labeled with the GCaMP6f sensor. Rectangles indicate four simultaneously imaged layers (ROI 1-4). Numbers indicate distances from the pia mater. Neurons were labeled in the V1 region using sparse labeling. Somata and neuronal processes of the three other GCaMP6f-labeled neurons situated in the same scanning volume were removed from the z-stack for clarity. (B) Average baseline fluorescence in the four simultaneously measured layers shown in A. Numbers in the upper right corner indicate imaging depth from the pia matter. (C) Representative  $\text{Ca}^{2+}$  transients were derived from the numbered sub-regions shown in B following motion artifact elimination. Responses were induced by moving grating stimulation into three different directions at the temporal intervals indicated with gray shadows. (D) The averaged baseline fluorescence images from B are shown on gray scale and were overlaid with the color-coded relative  $\text{Ca}^{2+}$  changes ( $\Delta F/F$ ).

### 6.6.5 Volume scanning with snake scanning and multi-cube

Our data demonstrated that, even though the brain moves along all three spatial dimensions, we could still preserve fluorescence information and effectively eliminate motion artifacts by scanning at reduced dimensions, along surface elements, in 3D. However, under some circumstances, for example in larger animals or at certain surgery or behavioral protocols, the amplitude of motion can be larger than the z dimension of the PSF and the missing third scanning dimension cannot be compensated for. To sufficiently preserve fluorescence information even in these cases, we may regain the missing scanning z dimension by extending the surface elements to volume elements by using an automatic algorithm until we reach the required noise elimination efficiency for measurements. To demonstrate this in two examples, we extended 3D ribbons to folded cuboids (called “snake scanning”, **Figure 43A**) and multi-frames to multi-cuboids (called “multi-cube scanning”).

#### *Snake scanning*

A spiny dendritic segment of a GCaMP6f-labeled layer II/III neuron was selected from a sparsely labeled V1 region of the cortex for snake scanning (**Figure 43B**). According to the z-stack taken at the beginning, we selected guiding points, interpolated a 3D trajectory, and generated a 3D ribbon which covered the whole segment as described above. Then we extended the ribbon to a volume, and performed 3D snake scanning from the selected folded cuboid. Three dimensional  $\text{Ca}^{2+}$  responses were induced by moving grating stimulation, and were projected into 2D as a function of distances along the dendrite and along one of the perpendicular directions (**Figure 43C**). Finally, data were maximal-intensity-projected along the second (and orthogonal) perpendicular axis to show average responses for three moving directions separately and together, following motion correction. Alternatively, we were able to avoid maximal intensity projection to a single plane by transforming the folded snake form into a regular cube. In this representation,  $\text{Ca}^{2+}$  transients could be calculated from different sub-volumes (**Figure 43D**). Note that, due to the preserved good spatial resolution, we can clearly separate each spine from each other and from the mother dendrite in moving animals. Therefore, we can simultaneously record and separate transients from spines even when

they are located in the hidden and overlapping positions which are required to precisely understand dendritic computation (**Figure 43D**).

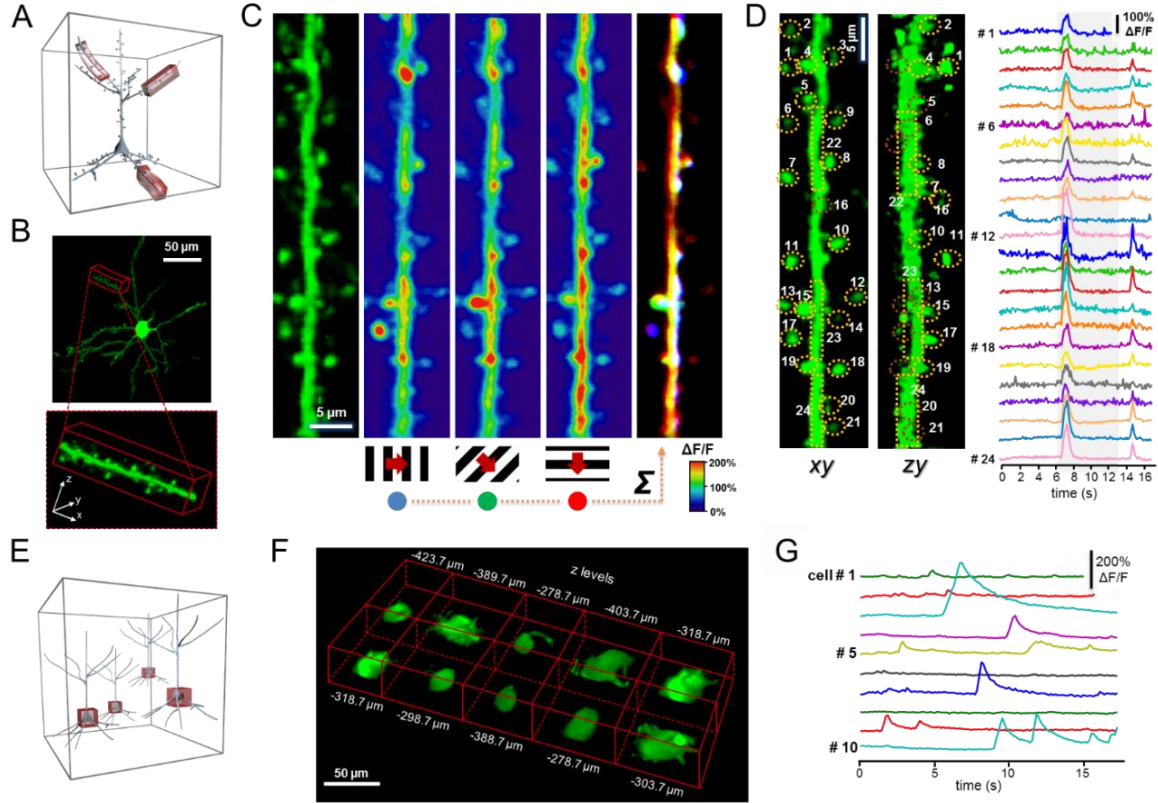


**Figure 43. Fast 3D volume imaging of dendritic and somatic activity in behaving animals.** (A) Schematic of the 3D measurement. 3D ribbons selected for 3D scanning can be extended to 3D volume elements (3D “snakes”) to completely involve dendritic spines, parent dendrites, and the neighboring background volume to fully preserve fluorescence information during brain movement in awake, behaving animals. (B) Top, z projection of a pyramidal neuron in the V1 region labeled with GCaMP6f sensor using sparse labeling. Bottom, selected dendritic segment is shown at an enlarged scale. (C) Fast snake scanning was performed at 10 Hz in the selected dendritic region shown in B. Fluorescence data were projected as a function of the distance along the longitudinal and the transverse directions, then data were projected at maximal intensity along the second transverse direction. Left, average of 30 frames from the recorded video. Middle, peak  $Ca^{2+}$  responses following visual stimulation with periodic gratings moving in three different directions. Right, relative fluorescence responses for each of the three different stimuli were transformed to either red, green, or blue and summed: the result is shown as an RGB image. (D) The same dendritic segment as in C, but the 3D volume is shown as x-y and z-y plane projections. z-y projection is shown after 3D deconvolution from a 3D stack of the volume for better visualization of the dendritic spines. Right, representative spontaneous  $Ca^{2+}$  responses derived from the coded sub-volume elements correspond to dendritic spines and two dendritic regions. Transients were derived from the sub-volume elements following 3D motion correction at subpixel resolution. (E-G) Multi-cube scanning. (E) Schematic of the 3D multi-cube measurements. (F) Volume-rendered image of 10 representative cubes selecting individual neuronal somata for simultaneous 3D volume imaging. (G) Following 3D motion correction,  $Ca^{2+}$  transients were derived from the 10 cubes shown in F.

### Multi-cube scanning

To demonstrate the second volume scanning method, multi-cube imaging, we simply extended frames to small cubes (**Figure 43E**) and added a slightly larger  $z$  dimension than the sum of the  $z$  diameter of somata and the peak  $z$  movement to preserve all somatic fluorescence points during motion. Simultaneous measurements of ten GCaMP6f-labeled somata were performed from 8.2 Hz up to 25.2 Hz using relatively large cubes (each cube was between  $46 \times 14 \times 15$  voxels and  $46 \times 32 \times 20$  voxels, where one voxel was  $1.5 \mu\text{m} \times 3 \mu\text{m} \times 4 \mu\text{m}$  and  $1.5 \mu\text{m} \times 1.5 \mu\text{m} \times 4 \mu\text{m}$ ). This spatial and temporal resolution made it possible to resolve the sub-cellular  $\text{Ca}^{2+}$  dynamic. We can further increase the scanning speed or the number of recorded cells inversely with the number of 3D drifts used to generate the cubes. For example, 50 somata can be recorded at 50 Hz when using cubes made of  $50 \times 10 \times 5$  voxels. Similarly, to multi-frame recordings, ROIs can be ordered next to each other for visualization (**Figure 43F**). Transients were derived from each cube using small sub-volumes (**Figure 43G**). As above, here we calculated the net displacement vector and corrected sub-volume positions at each time point during calculation of the  $\text{Ca}^{2+}$  transient in order to eliminate motion. We found that the use of volume scanning reduced the amplitude of motion artifacts in  $\text{Ca}^{2+}$  transients by  $19.28 \pm 4.19$ -fold during large-amplitude movements in behaving animals (**Figure 44**).

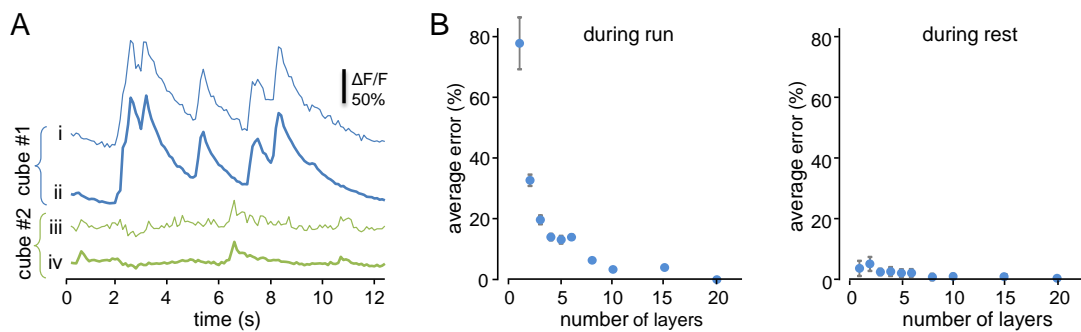


**Figure 44. The efficiency of motion correction during multi-cube volume scanning.** Activity of 10 neurons was recorded with multi-cube scanning. Each cube had a  $30 \mu\text{m} \times 30 \mu\text{m}$  base with  $30 \times 30$  pixels resolution and the  $z$  dimension of each cube (the number of  $z$  layers used) was varied during the 3D measurements from 1 to 20 ( $z$  layers were evenly distributed in the total of  $40 \mu\text{m}$   $z$  range) to compare SNR of the 3D measurements and motion artefact compensation as a function of the  $z$  layers. (A) Exemplified transients were derived from recording cubes consisting of one (i and iii) and twenty (ii and iv)  $z$  layers. Note the improvement in the SNR when twenty layers were used. (B)  $\text{Ca}^{2+}$  transients derived from recording cubes consisting of variable numbers of  $z$  layers (from 1 to 20) were subtracted from the  $\text{Ca}^{2+}$  transient recorded simultaneously with a cube of twenty layers. Then the absolute value of the relative error was averaged over time during running and rest and is shown on the y axes as mean  $\pm$  SD.

These data demonstrate that multi-cube and snake scanning can effectively be used for the 3D measurement of neuronal networks and spiny dendritic segments in multiple sub-volumes distributed over the whole scanning volume. Moreover, these methods are capable of completely eliminating even large-amplitude motion artifacts.

### 6.6.6 Multi-3D line scanning

In the previous sections, we discussed how we extended 1D scanning points to 2D or 3D objects. In this section, we will discuss how to extend scanning points along only one dimension to perform measurements at a higher speed (**Figure 45**).

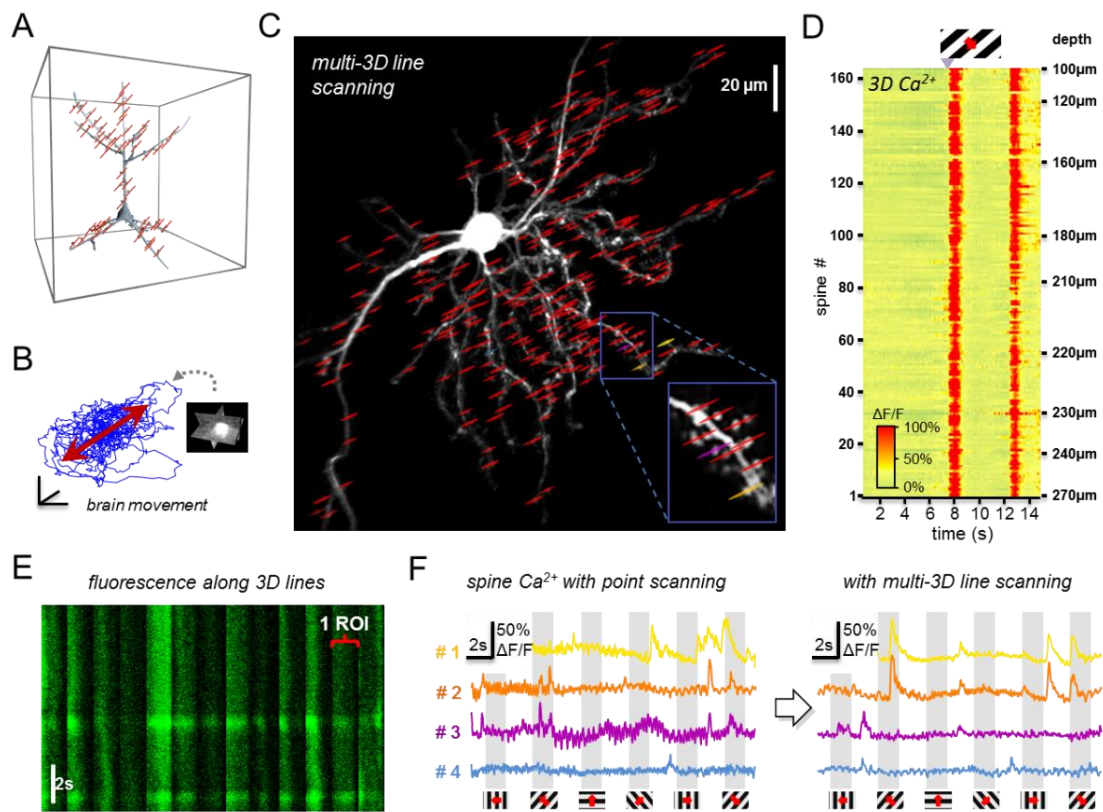


**Figure 45. Multi-3D line scanning of spine assemblies in behaving animals.** (A) Schematic of the measurement. Each scanning line is associated with one spine. (B) Amplitude of brain motion (blue) was recorded by the fast 3D motion-detection method by using three perpendicular imaging planes of a bright fluorescent object. Average motion direction is shown in red. The scale bars are 50 nm. (C) Z-projection of a layer 2/3 pyramidal cell, labeled with GCaMP6f. Red lines indicate the scanning lines running through 164 pre-selected spines. All scanning lines were set to be parallel to the average motion shown in B. (D) Corresponding 3D Ca<sup>2+</sup> responses recorded simultaneously along the 164 spines. (E) Exemplified individual raw Ca<sup>2+</sup> transients recorded along 14 spines using multi-3D line scanning. Note the movement artifacts in the raw fluorescence. (F) Exemplified Ca<sup>2+</sup> transients measured using point scanning (left) and multi-3D line scanning (right). Note the improvement in the SNR when multi-3D line scanning was used. Transients were induced with moving grating stimulation.

We found that, in many experiments, sample movement is small, and brain motion can be approximated with a movement along a single 3D trajectory (**Figure 45B**). In this case, we can extend each point of 3D random-access point scanning to only multiple short 3D lines instead of multiple surface and volume elements (**Figure 45A**).

In the first step we selected points from the z stack. Next, we recorded brain motion to calculate the average trajectory of motion, as above. In the third step, we generated short 3D lines with 3D DRIFT AO scanning to each pre-selected point in such a way that the center of the lines coincided with the pre-selected points, and the lines were set to be parallel to the average trajectory of motion. Finally, we simultaneously detected the activity of 169 spines along the 3D lines (**Figure 45C and E**). If we switched back from the multi 3D line scanning mode to the classical 3D point-by-point scanning mode, oscillations induced by heartbeat, breathing, and physical motion immediately appeared in transients (**Figure 45F**). These data showed that, in cases when the amplitude of the movement is small and mostly restricted to a 3D trajectory, we can effectively use multi 3D line scanning to rapidly record over 160 dendritic spines in behaving animals.

### **6.6.7 Advantage of the different scanning modes**

We have described six novel laser scanning methods for 3D imaging using drift AO scanning. These methods have different application fields based on how they are suited to different brain structures and measurement speed. The fastest method is multi-3D line scanning, which is as fast as random-access point-by-point scanning and can be used to measure spines or somata at 53 kHz per ROI (**Figure 46**). The number of ROIs is only limited by MATLAB and the memory of the PC (could be  $>10^5$ ). In the second group, multi-layer, multi-frame imaging, chessboard scanning, and 3D ribbon scanning can measure up to about 5.3 kHz per ROI along long neuronal processes and somata. Finally, the two volume scanning methods, multi-cube scanning and snake scanning, allow measurement of up to about 1.3 kHz per volume element, and are ideal for measuring somata and spiny dendritic segments, respectively. The two volume scanning methods provide the best noise elimination capability because fluorescence information can be maximally preserved.

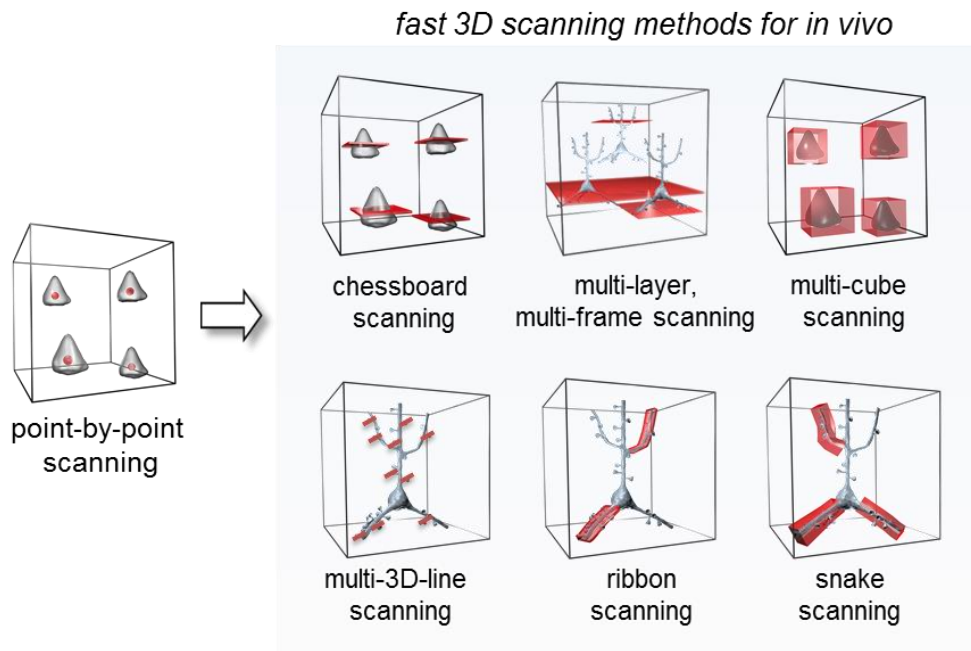


**Figure 46.** Summary of fast 3D scanning methods developed for in vivo imaging in behaving mice. Schematics comparing the currently used 3D random-access point-by-point scanning method with the new 3D scanning methods developed for imaging the moving brain of behaving animals. Red points, lines, surface and volume elements illustrate the ROIs selected for measurements.

### 6.6.8 Motion correction in 3D

Data resulting from the 3D ribbon scanning, multi-layer, multi-frame scanning, and chessboard scanning methods are stored in a 3D array as time series of 2D frames. The 2D frames are sectioned to bars matching the AO drifts to form the basic unit of our motion correction method. Since each ribbon, frame or volume can be oriented differently in 3D space, the local coordinate system of measurements varies as a function of distance along a given ribbon, and also between the ROIs covering different regions. **Figure 47** shows motion correction during ribbon scanning. Here, brain motion generates artifacts with different relative directions in each ribbon, so the 2D movement correction methods used previously<sup>54</sup> cannot be directly used for the flattened 2D movie generated from ribbons. To solve this issue, we divided the recordings of each dendritic region into short segments (**Figure 47A**). Then the displacement of each 3D ribbon segment was calculated by cross-correlation, using the brightest image as a reference (**Figure 47B**). Knowing the original 3D orientation of each segment, the 3D displacement vector for each ribbon segment could be calculated (**Figure 47C**). Then

we calculated the median of these displacement vectors to estimate the net displacement of the recorded dendritic tree (**Figure 47D**). The displacement vector for each frame and for each bar is transformed to the Cartesian coordinate system of the sample, knowing the scanning orientation for each bar. Noise bias is avoided by calculating the displacement vector of a frame as the median of the motion vectors of its bars. This common displacement vector of a single frame is transformed back to the data space. The resulting displacement vector for each bar in every frame is then used to shift the data of the bars using linear interpolation for subpixel precision. In other words, each dendritic segment backshift with the required displacement vector corresponding to different shift directions on the final 2D videos, since each ROI represent a different 3D orientation (**Figure 47E**). Gaps are filled with data from neighboring bars, whenever possible.

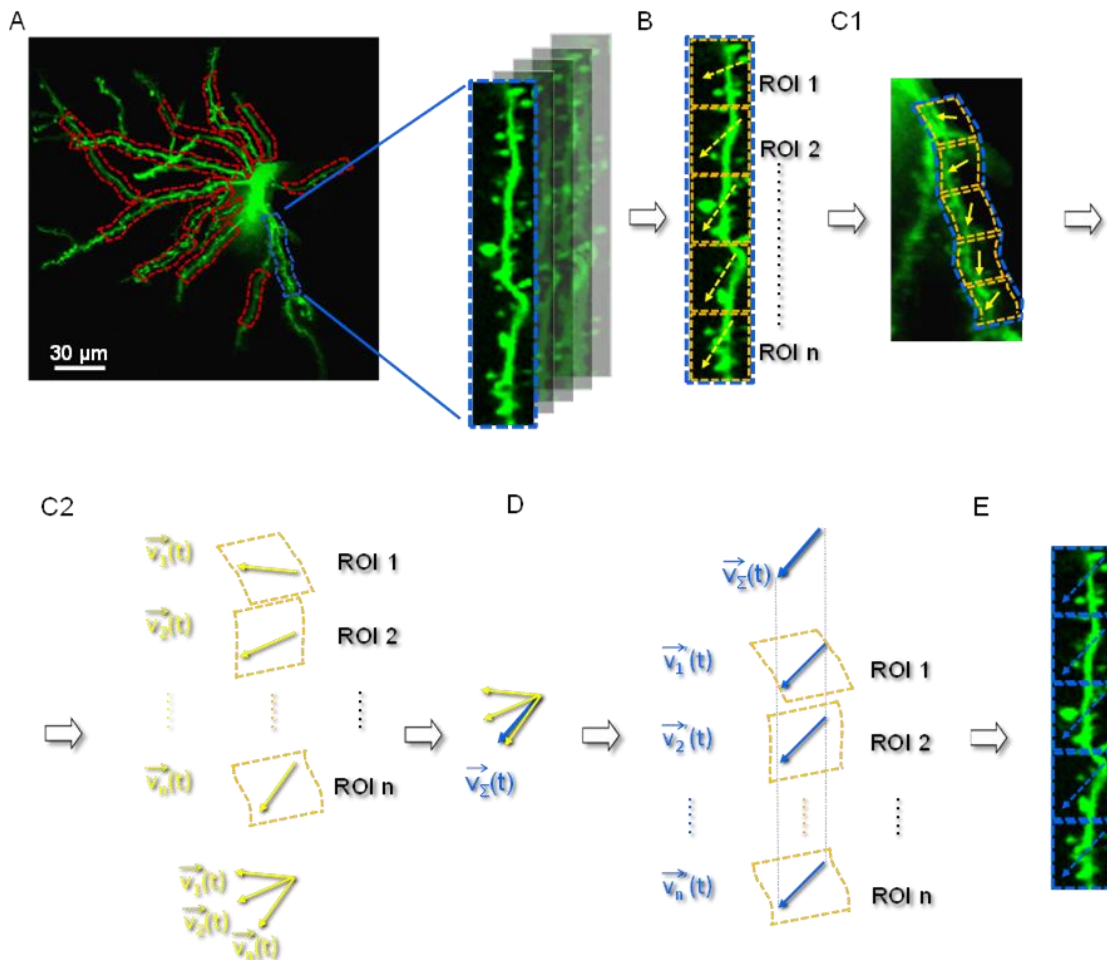


**Figure 47. Motion correction in 3D.** (A) The results of scanned ribbons are stored in time series of 2D frames in each dendritic region (dashed red boxes). (B) The 2D frames of each ribbon are further sectioned to segments (ROIs) which are oriented parallel to the direction of

the local AO drifts. Displacement vectors (dashed yellow arrows) are calculated separately for each segment as a function of time with autocorrelation. (C1-C2) The displacement vectors are transformed to the original 3D Cartesian coordinate system of the sample (yellow arrows). (D) The net displacement vector of a frame is taken as the median of the local displacement vectors of its ROIs, then this net displacement vector is transformed back to the 2D data array of segments. (E) Finally, data were shifted in each segment with subpixel precision by the projection of the median displacement vector (blue dashed arrows).

The typical execution time was about a minute. For example, for the four-layer raster scan with 133 frames and 200 x 253 pixels / layer, the motion correction algorithm ran in  $66.4 \pm 0.25$  seconds. For the ribbon scanning of 300 frames with 30 x 1633 pixels for the entire measured region, the motion correction took  $80.8 \pm 0.15$  s. For the chessboard scanning with 136 ROIs and 25 x 25 pixels per ROI for 154 frames, the run time of the motion correction was  $67.21 \pm 0.13$  seconds using a PC with an i7 processor and 12 GB of memory.

To quantify the efficiency of our methods for motion correction during *in vivo* measurements, as before, I labeled neurons and their processes with GCaMP6f sensor, used 3D ribbon scanning, and projected the recorded fluorescence data to movie frames. We got the best results when each frame of the video recorded along 3D ribbons was corrected by shifting the frames at subpixel resolution to maximize the fluorescence cross correlation between the successive frames (

**Figure 48**). Ribbon scanning and the successive frame shifts at subpixel resolution in running animals increased SNR by  $7.56 \pm 3.14$ -fold ( $p > 0.000015$ ,  $n = 10$ ) when compared to 3D random-access point scanning (**Figure 49**).

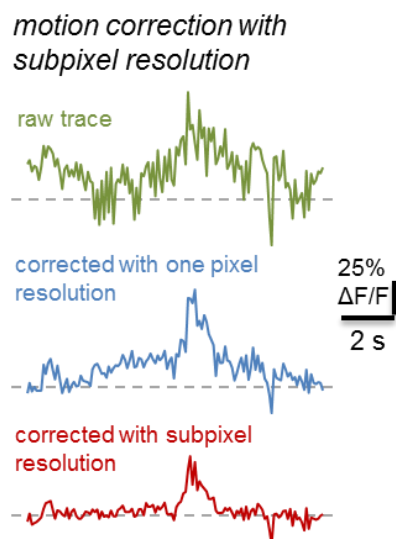
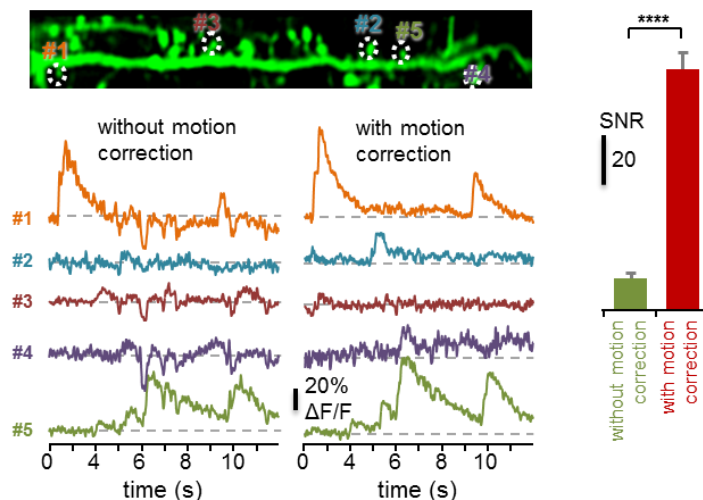
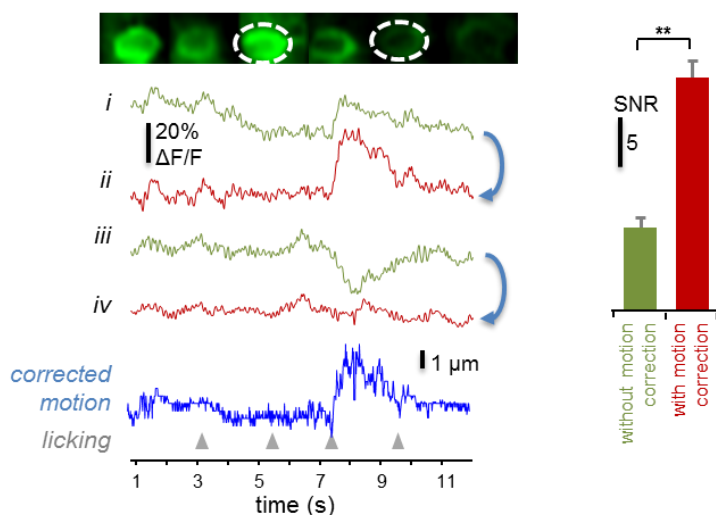


**Figure 48. Comparison of motion correction resolution.** Exemplified individual  $\text{Ca}^{2+}$  transient from a single dendritic spine derived from the movie which was recorded with 3D ribbon scanning along a  $49.2 \mu\text{m}$  spiny dendritic segment in a behaving mouse (green). When  $\text{Ca}^{2+}$  transients were derived following motion-artifact correction performed at pixel (blue) and sub-pixel resolution (red), the motion-induced artifacts were eliminated and SNR was improved.

### A elimination of motion artifacts at spines



### B elimination of motion artifacts at somata



amplitude. Note that motion-induced and neuronal  $\text{Ca}^{2+}$  transients overlap. Moreover, transients could have a negative amplitude without motion correction. Right, SNR of the transients with (red) and without (green) motion correction (mean  $\pm$  SEM,  $n = 3$ ).

### Figure 49. Quantitative analysis of the motion artifact elimination capability of 3D DRIFT AO scanning.

(A) Examples of motion-artifact correction. Top, single frame from the movie recorded with 3D ribbon scanning from an awake mouse. Bottom, exemplified  $\text{Ca}^{2+}$  transients derived from the recorded movie frames from the color-coded regions. Note the improved SNR of the transients when they were derived following motion-artifact correction at subpixel resolution. Right, SNR of spine  $\text{Ca}^{2+}$  transients calculated (100 transients,  $n = 5/5$  spines/mouse). Transients are shown without and with motion correction at subpixel resolution.

(B) Left, simultaneous 3D imaging of VIP neuron somata during a classical behavior experiment where conditioned stimulus (water reward) and unconditioned stimulus (air puff, not shown) were given for two different sounds. Exemplified somatic transients are shown with (red) and without motion correction at subpixel resolution (green). Blue trace shows motion

#### 6.6.9 Simulation of the quality increment with drift scanning

To quantify motion-induced errors and the efficiency of motion artifact correction during ribbon scanning, I simulated motion correction with an artificial scan images where the noise, motion and the activity were all known factors. For that I have acquired images from  $n = 5$  somata and 5 dendritic segment with resolution similar to those we

used during the in vivo measurement. Then a known motion, known Ca<sup>2+</sup> activity and noise with defined characteristic were added to these videos.

For this, to add the artificial movement, I measured brain movement by rapidly scanning a bright, compact fluorescent object which was surrounded by a darker background region. To do this, I centered three orthogonal squares (in the xy, xz, and yz planes), on the fluorescent object, recorded fluorescence, and displacement was calculated from the x, y, and z projections of the recorded fluorescence (defined as “fast 3D motion-detection” method) while the mouse was running in a linear virtual track (**Figure 50**; **Figure 51**). I separated resting and moving periods according to the simultaneously recorded locomotion information (for resting periods n = 42 from 3 mice with the average length of 7.2 s; for moving periods n = 31 from 3 mice with the average length of 4.9 s) (**Figure 50A** and **B**). Brain motion can induce fluorescence artifacts, because there is a spatial inhomogeneity in baseline fluorescence and also in the relative fluorescence signals (**Figure 50C**). The amplitude of motion-generated fluorescence transients can be calculated by substituting the average peak-to-peak motion error into the histogram of the relative fluorescence change (**Figure 50C**). The average  $\Delta F/F(x)$  histogram was relatively sharp for dendrites (average of 150 cross sections from n = 3, 100  $\mu\text{m}$  long dendritic segments, **Figure 50C**), therefore the average motion amplitude during running corresponds to a relatively large ( $80.1 \pm 3.1\%$ ) drop in the fluorescence amplitude, which is about  $28.6 \pm 7.74$ -fold higher than the average amplitude of a single AP-induced Ca<sup>2+</sup> response (**Figure 56** and **Figure 57**). These data indicate the need for motion artifact compensation.

Next, I investigated separately the effect of post-hoc frame shifts on the SNR following ribbon scanning. Low-amplitude spine Ca<sup>2+</sup> transients were barely visible when transients were derived from the raw video. For a precise analytical analysis I added the same 1, 2, 5, and 10 AP-induced average transients to the images of a soma (**Figure 51A**) using the data from the in vitro measurements presented on **Figure 5**. Then I generated a series of frames by shifting each frame with the amplitude of brain motion recorded in advance (similarly to **Figure 50A**). Finally, I recalculated Ca<sup>2+</sup> transients from the frame series with and without using the motion-correction algorithm, using ROIs of the same size to compare the SNR of point-by-point scanning and the motion-corrected 3D ribbon scanning on the same area (**Figure 51B**).

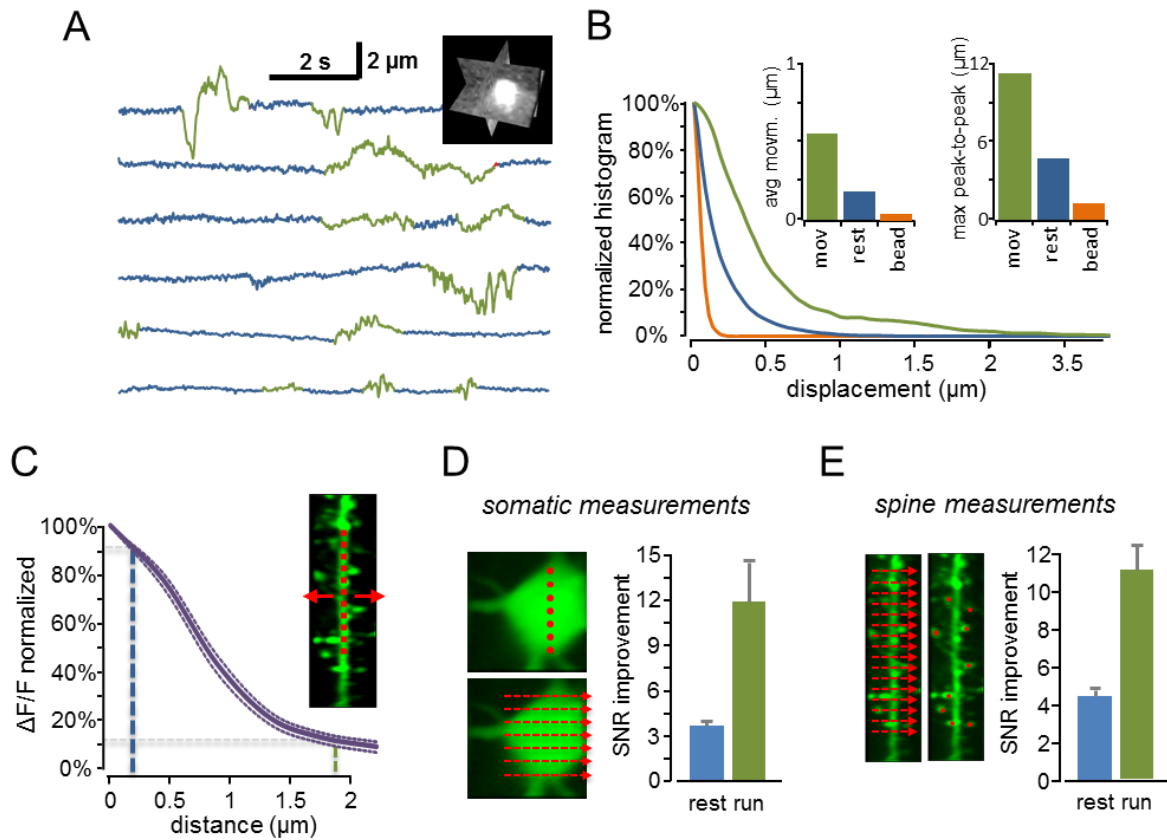


**Figure 50. Simulation for quantifying motion artifact elimination capability of 3D DRIFT AO scanning.** (A) Brain motion was recorded at 160 Hz by imaging a bright, compact fluorescent object with three orthogonal,  $xy$ ,  $xz$ , and  $yz$  planes (fast 3D motion-detection method, Figure S16). Exemplified transient of brain displacement projected on the  $x$  axis from a 60 s measurement period when the mouse was running (green) or resting (blue) in a linear maze. Movement periods of the head-restrained mice were detected by using the optical encoder of the virtual reality system. (B) Displacement data were separated into two intervals according to the recorded locomotion information (running in green and resting in blue) and a normalized amplitude histogram of brain motion was calculated for the two periods. Inset shows average and average peak-to-peak displacements in the resting and running periods. Red bars are control fluorescent data with fixed beads. (C) Normalized change in relative fluorescence amplitude as a function of distance from the center of GCaMP6f-labeled dendritic segments ( $\Delta F/F(x)$ , mean  $\pm$  SEM,  $n = 3$ ). Blue and green dashed lines indicate average peak-to-peak displacement values calculated for the resting and running periods, respectively. Note the  $>80\%$  drop in  $\Delta F/F$  amplitude for the average displacement value during running. Inset, dendritic segment example.  $\Delta F/F$  was averaged along a dashed red line and then the line was shifted and averaging was repeated to calculate  $\Delta F/F(x)$ . (D) Left, image of a soma of a GCaMP6f-labeled neuron. Red points and dashed arrows indicate scanning points and scanning lines, respectively. Right, normalized increase in SNR calculated for resting (blue) and running (green) periods in awake animals when scanning points were extended to scanning lines in somatic recordings, as shown on the left. SNR with point-by-point scanning is indicated with red dashed line (ctr.). Calculations are detailed in Figure S3. (E) Similar calculations as in D, but for dendritic recordings. Signal-to-noise ratio of point-by-point scanning of dendritic spines was compared to 3D ribbon-scanning during resting (blue) and running (green) periods. Note the more than 10-fold improvement when using 3D ribbon scanning.

Data indicates that 3D ribbon scanning which, in contrast to point-by-point scanning, allows motion correction, can largely improve the SNR in the case of small, 1-5 AP-associated signals recorded most frequently during *in vivo* measurements ( $11.72 \pm 2.59$ -fold,  $p > 0.025$ ,  $n = 4$  somata;  $n = 44$  repeats for 1-10 APs; **Figure 50D** and **Figure 51C**). I repeated the entire process on dendritic spines (**Figure 51E-G**). The method also significantly improved the SNR of single spine  $\text{Ca}^{2+}$  responses ( $11.64 \pm 1.25$  fold,  $n = 4$  spines,  $n = 44$  repeats; **Figure 50E** and **Figure 51G**). The average difference between the original motion trajectory and the movement artifact correction, which indicates the error of the method more directly, was  $0.139 \pm 0.106 \mu\text{m}$  for somatic and  $0.118 \pm 0.094 \mu\text{m}$  for dendritic measurements (**Figure 51D** and **H**). There was only a small increase in the error (to  $0.154 \pm 0.120 \mu\text{m}$ ) when the simulated videos were down sampled from 160 Hz to 40 Hz frame rate (**Figure 51D**). The sum of the FWHM of the PSF and the average diameter of dendrites or spines were much larger than the average residual error, indicating that the special precision of motion correction is appropriate for dendritic and spine measurements.

Note that the increase in the signal to noise ratio calculated from the simulation (**Figure 50D and E**) well met the improvement I calculated from the experimental data (**Figure 49**) indicating that our modeling can be sufficient to determine the maximum movement that can be compensated with our method as well as the amplitude of the smallest  $\text{Ca}^{2+}$  event which we can still detect with the combination of 3D AO DRIFT scanning and 3D motion correction.

However, the result of this section is assuming that we can precisely determine the movement of the brain by recording the x-y-z coordinates of a bright fluorescent object. This presumption is verified in the next section.

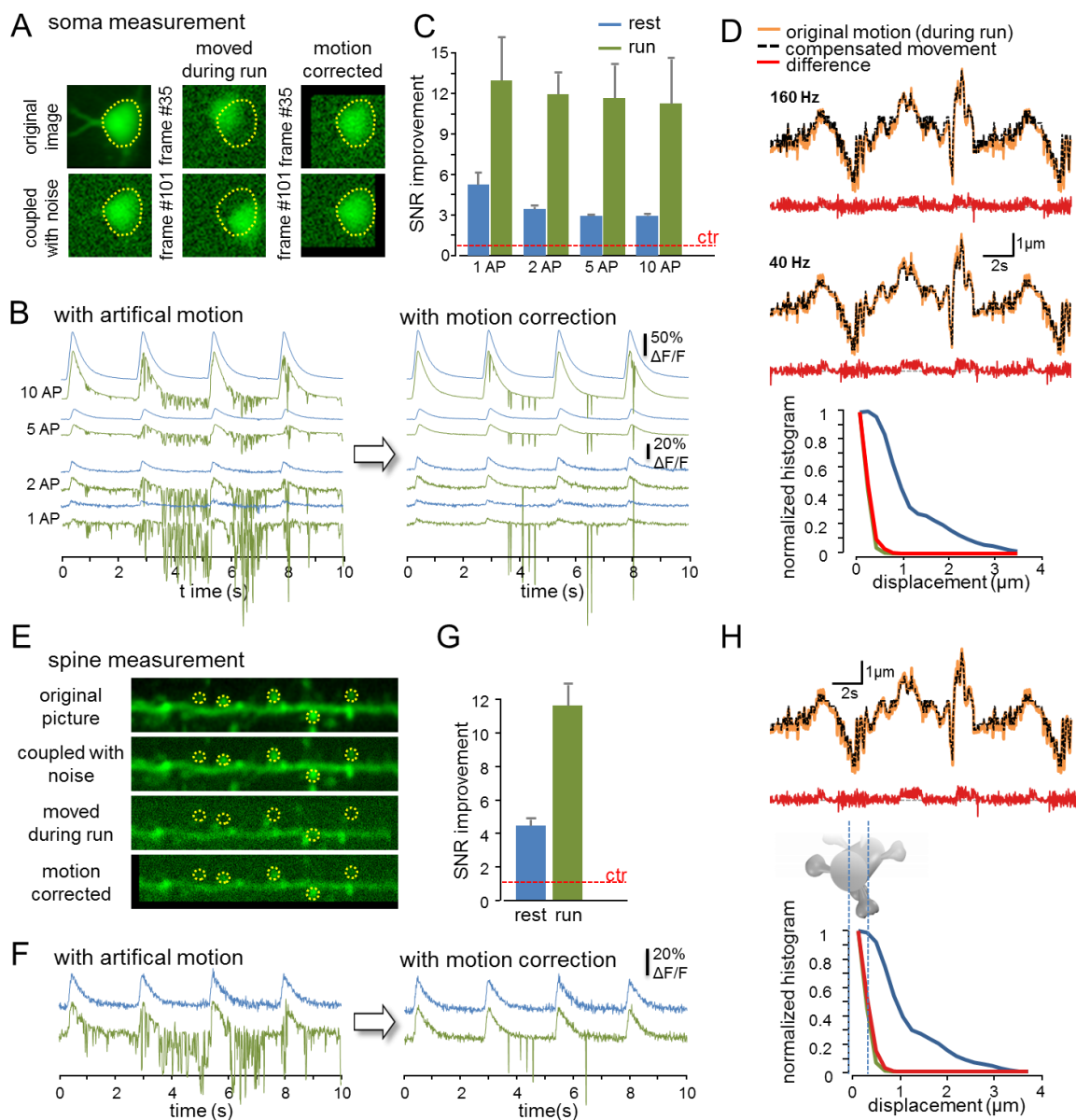


**Figure 51. Estimating SNR improvement following the elimination of motion artifacts in multi-layer, multi-frame imaging, chessboard scanning, and ribbon scanning methods.** (A) Top left, smoothed image of an exemplified neuronal soma (original image). Bottom left, SD of the raw fluorescent pixel values was measured and averaged for multiple regions with no somatic or dendritic structure from the original raw videos, then white noise with the same SD ( $485.26 \pm 88.66$  DAC unit;  $n = 10$ ) was added to each frame of the simulated video. Middle column, displacement by brain movement was measured in advance as a function of time using the fast 3D motion-detection method (at 160 Hz) and also added to the soma images at every time point to generate a time-lapse movie. In this way, we generated artificial videos for a more quantitative analysis. The two images are two example frames from the movie with different displacement amplitudes (moved during run). Yellow dotted lines indicate the initial location of the soma. Right column, the same two example frames following the elimination of motion artifacts (motion corrected). (B) Left, time-lapse movies were generated as in A, adding white noise, and brain displacement measured in advance to the original image, but here we also added ten, five, two, and one AP-generated responses and calculated somatic  $\text{Ca}^{2+}$  transients (green traces) from the somatic ROI. Control transients (blue traces) were generated without

adding the brain displacement to the frames of the video. Right, the same ten, five, two, and one AP-generated responses, but transients were generated following motion artifact elimination. Note that the manual detection of one or two AP-induced transients is virtually impossible without the elimination of motion artifacts. (C) Averaged improvement in SNR of  $Ca^{2+}$  transients following the elimination of motion artifacts was plotted as a function of the number of APs for resting (blue) and running (green) periods (mean  $\pm$  SEM). Red dashed (ctr.) line indicates the SNR of  $Ca^{2+}$  transients without compensation. (D) Top, exemplified transients. The original brain motion trajectory (green) recorded with the fast 3D motion-detection method (160 Hz) was overlaid with the movement derived from the images (at 160 Hz imaging rate) during the off-line 3D motion-correction method (orange, dashed line). The difference between the two trajectories shows the error of the 3D motion-correction method (red). Note the small error ( $0.139 \mu\text{m} \pm 0.106 \mu\text{m}$ ) following motion artifact compensation. Middle, the same, but imaging rate was decreased to 40 Hz. As the 40 Hz imaging speed is about at the cut-off frequency of brain movement the reduced imaging speed did not significantly increase the error of the method. Bottom, normalized amplitude histogram of the motion during resting (green), and before (blue) and after (red) motion artifact correction during running periods. (E-G) Similar to panels A-B, but for dendritic measurements. Calculations were made on dendritic spine responses (yellow circles). For these calculations we used the average spontaneous  $Ca^{2+}$  responses of dendritic spines, recorded in advance, instead of 1, 2, 5, and 10 AP-induced responses. (H) Same as D but for dendrites. Note that the error following motion artifact compensation (red) is smaller than the average diameter of dendrites and spines. The average amplitude of the residual displacement error was small ( $0.118 \pm 0.095 \mu\text{m}$ ). The sum of the FWHM of the PSF ( $\approx 0.4 \mu\text{m}$ ) and the average diameter of dendrites or spines (dendrite: 0.5-1.75  $\mu\text{m}$ ; spine:  $0.42 \pm 0.1 \mu\text{m}$ ; see Holthoff et al., 2002, Konur et al., 2003) were larger than this average residual error, indicating that the special precision of motion correction is proper for dendritic and spine measurements.

#### 6.6.10 Validation of the fast 3D motion-detection method and recording brain movement

The results of section 6.6.9 are based on the assumption that we can follow the position of a fluorescent object at high speed with sub micrometer precision. To validate this fast 3D motion-detection method with an independent technique, I moved fluorescent beads along the x, y, or z axes by using fast piezo actuators (ASM003 Thorlabs) driven by sine wave in the 0-160 Hz frequency range (**Figure 52A**). The high resonant frequency (2 kHz) of the piezo actuator provided a flat mechanical transmission in the 0-160 Hz frequency range. I recorded the position of the fluorescent beads by imaging them with the fast 3D motion-detection method by using small xy and xz frames (xy:  $15 \mu\text{m} \times 15 \mu\text{m}$ ; xz:  $15 \mu\text{m} \times 30 \mu\text{m}$ ) which were centered to the beads. To determine the position of the moving beads along a given axis, the recorded fluorescence was projected onto that particular axis and the maximum was determined by Gaussian fitting at each time point (**Figure 52B**).

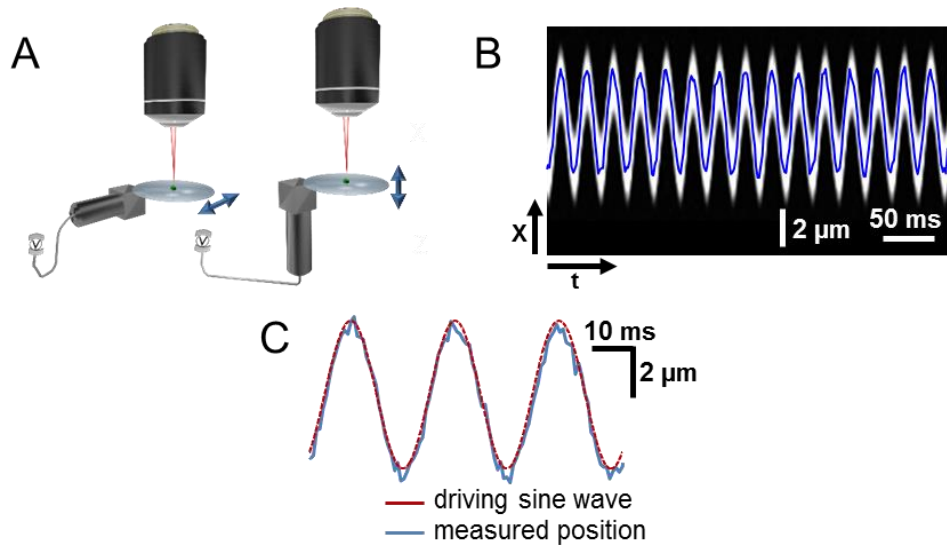


**Figure 52. Validation of the fast 3D motion-detection method.** (A) The amplitude and phase transfer function of the fast 3D motion-detection method was measured in the 0-160 Hz bandwidth by using fluorescent beads and a fast piezo actuator. Fluorescent beads (diameter 6 μm) were fixed through a small cover glass onto the fast piezo actuator, which had a high resonant frequency (up to 2 kHz). This provided smooth mechanical transmission in the 0-160 Hz frequency range. The piezo actuator oscillated either along the horizontal or the perpendicular directions by being driven with sine waves of 0-160 Hz frequency. The movement of a selected bead was detected by recording the position of its fluorescence using the fast 3D motion-detection method along the xy and xz planes. (B) Example, fluorescence of the bead oscillating (at 40 Hz) along the x axis was projected to the x axis and plotted as a function of time and distance. The blue trace is the position of the maximum fluorescence, determined by Gaussian fitting for each time point. (C) Maximal fluorescence was plotted as a function of time and distance and was fitted with a sine wave to measure amplitude transmittance and phase shift relative to the driver signal.

Then I plotted the position of the maximums as a function of time and fitted it with a sine curve to determine amplitude and phase shifts as a function of the driver frequency (**Figure 52C**). The standard deviation of the difference between the recorded bead position and the fitted sine wave was small ( $SD_{\text{moving pos. err.}} = 0.109 \pm 0.004 \mu\text{m}$ ), being similar to the standard deviation of the position of the beads which were fixed to the animal holders ( $SD_{\text{fixed bead pos.}} = 0.075 \pm 0.031 \mu\text{m}$ ). These low standard deviations, and the flat amplitude and phase transfer functions of the position measurements (**Figure 53**) demonstrated that the fast 3D motion-detection method can be used to record brain motion in the 0-160 Hz range during *in vivo* recordings.

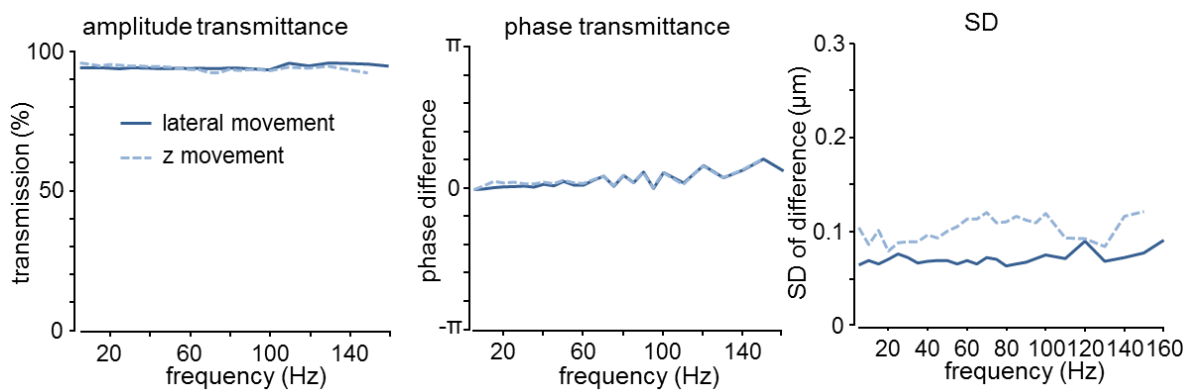


**Figure 53. Quantifying the measured signal accuracy.** Amplitude and phase transmittance was measured according to **Figure 52**. Transmittance and phase shifts plotted against the frequency showed only modest changes in the 0-160 Hz range. The SD of the difference between the recorded bead position and the fitted sine wave was also less than  $0.12\ \mu\text{m}$  in the entire range for both axis movements. These data indicate that the transfer function of the fast 3D motion-detection allows measurement of brain movement with high spatial resolution in the 0-160 Hz range.

Next I recorded the position of small fluorescent objects during *in vivo* recordings by imaging them using the fast 3D motion-detection method by using small xy and yz frames (xy:  $15\ \mu\text{m} \times 15\ \mu\text{m}$ ; xz:  $15\ \mu\text{m} \times 20\ \mu\text{m}$ ) which were centered to the small fluorescent objects. To calculate movement along a given axis, fluorescence data were projected to that particular axis and the position of the object was determined by Gaussian fitting at each time point as before (**Figure 54A**). In parallel, I recorded movement of mice on the virtual reality wheel to separate periods of movement and rest (**Figure 54B**). Then I calculated the average Fourier spectra of the movement of bright objects during the running and rest periods (30 s long transients, n=15-17 per case) and compared it to the spectrum of fixed fluorescent beads. Motion artifacts in awake animals contributed only to the 0-50 Hz range of the Fourier spectra (**Figure 54C**). In summary, these data showed that the fast 3D motion-detection method has the required bandwidth to detect *in vivo* motion with about  $0.1\ \mu\text{m}$  accuracy; therefore, it was used to detect motion trajectories from behaving animals. The data recorded by the fast 3D motion-detection method were then used to quantify the motion elimination capability of the new scanning methods of the 3D DRIFT AO microscopy.

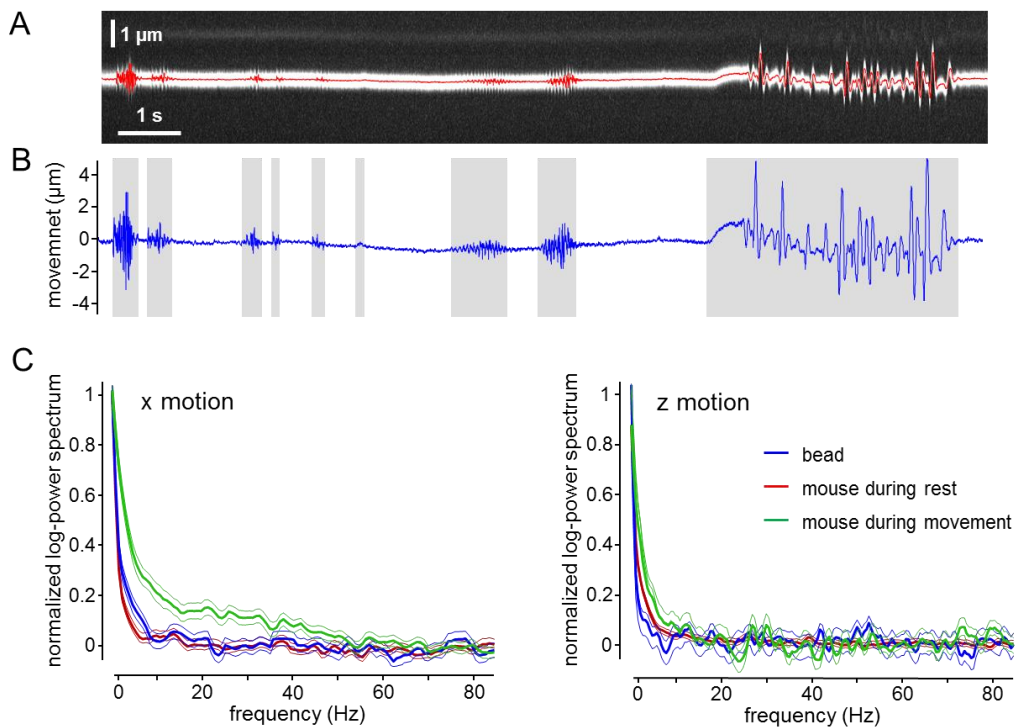


**Figure 54. Fast 3D motion-detection method was used to detect fast brain motion in awake mice.** (A) Position of a bright compact fluorescent object in the brain was recorded with the fast 3D motion-detection method at 160 Hz and plotted as a function of time. The red trace is the location of the maximum fluorescence determined by Gaussian fitting. (B) Locomotion was simultaneously detected in the one dimensional virtual reality. Gray bands indicate periods of motion. (C) Fourier spectra of the movement of bright fluorescent objects were averaged (mean  $\pm$  SEM) during rest (red) and running (green) periods ( $n=17$  measurements) and were compared to the motion spectrum of fluorescent beads which were fixed to the animal holder (blue). Note that the spectral amplitude of brain movement was not significantly larger above 40-50 Hz from the spectral amplitude of the movement of fixed fluorescent beads, indicating that the 0-160 Hz bandwidth of the fast 3D motion-detection method is sufficient. As the SD of the movement of the fixed fluorescent beads was also small ( $0.075 \pm 0.031 \mu\text{m}$ ), these data indicate that the fast 3D motion-detection method can reliably capture in vivo brain movement.

### 6.6.11 Single action potential measurement

To quantify if the increased SNR of our new scanning strategies can be sufficient for single AP resolution from individual  $\text{Ca}^{2+}$  transients recorded in the moving brain of behaving animals I compared SNR of different measurement paradigms. First I calculated standard deviation for measurement segments with no activity present and after motion correction (if the measurement type made it possible), thus the residual error should indicate the noise coming from not controlled sources. With this calculation standard deviation of the  $\text{Ca}^{2+}$  responses were as indicated on **Figure 55** ( $n = 20$  measurement segments with at least 5s length for each measurement type).

According to this result the SD improvement for chessboard scanning, multi-cube scanning, or multi-layer, multi-frame imaging in behaving animals is improved the factor of  $14.89 \pm 1.73$ ,  $14.38 \pm 1.67$ , and  $5.55 \pm 0.65$ , respectively as compared to 3D random-access point scanning (**Figure 55**).

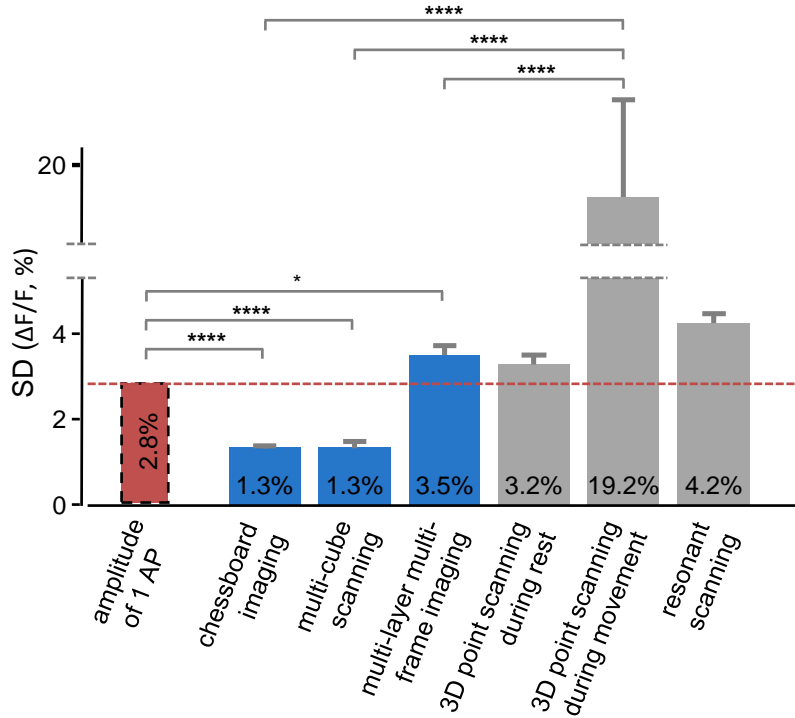


**Figure 55. Multi-layer, multi-frame imaging, chessboard scanning, and multi-cube imaging have better single AP resolution in behaving animals than 3D random-access AO scanning or raster scanning.** In this figure we compare the single AP resolution of six different scanning methods (multi-layer, multi-frame imaging, chessboard scanning, multi-cube imaging, 3D random-access scanning, and raster scanning). Neurons in the V1 region of the brain were labeled with GCaMP6f sensor using AAV vector and recorded at 880 nm. Standard deviation of individual  $Ca^{2+}$  transients recorded with the different scanning methods is compared to the average amplitude of single APs in the moving brain of behaving mice. Simultaneous scanning of over 100 neurons using chessboard scanning generated  $Ca^{2+}$  transients with a much smaller standard deviation than the average amplitude of single APs, indicating an excellent single AP resolution in behaving animals. Similarly, multi-cube scanning also has good single AP resolution. The standard deviation of  $Ca^{2+}$  transients, generated by multi-layer, multi-frame imaging, was just at the limit of single AP resolution. However, raster scanning or 3D random-access AO scanning in behaving animals cannot provide single AP resolution with the currently available GCaMP6f labeling. Although precise comparison of 2D and 3D scanning methods is not possible, we can conclude that the three new scanning strategies developed for somatic measurements provide much better signal-to-noise ratio, hence better single AP resolution, than previously used methods. P values are from left to right: 0,  $1.04 \times 10^{-10}$ ,  $2.24 \times 10^{-1}$ ,  $3.02 \times 10^{-14}$ ,  $6.01 \times 10^{-11}$ ,  $3.15 \times 10^{-9}$

Then I compared these values with the average  $\text{Ca}^{2+}$  responses amplitudes (**Figure 56**). For these I have performed simultaneous cell attached electrophysiological measurement with Ca imaging from in vivo behaving animals. Activity was recorded during visual stimulation (**Figure 56B**). (Note the difference of the  $\text{Ca}^{2+}$  amplitude measured in vitro **Figure 5** and **Figure 57**. This is caused by the wavelength difference between the two setups, while GCaMP6 sensors itself function similarly in both scenario.) For chessboard and multi-cube scanning the standard deviation of the motion artifact corrected  $\text{Ca}^{2+}$  responses became smaller than the average amplitude of single APs, which can indicate that single action potential detection can possible in neuronal network measurements in behaving animals. (**Figure 56B** show single AP induced  $\text{Ca}^{2+}$  responses recorded in vivo.)

However single AP detection was not possible with 3D random-access AO microscopy during running, because the standard deviation of  $\text{Ca}^{2+}$  responses was  $4.85 \pm 0.11$ -fold higher than the amplitude of single APs (**Figure 55**).

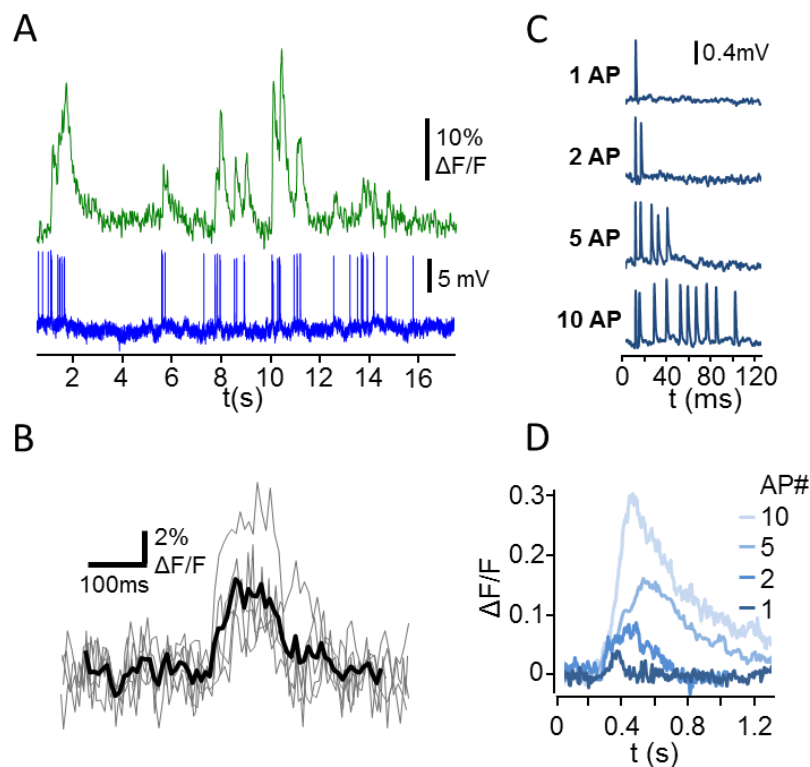


**Figure 56. Simultaneous electro-physiological recording and 3D DRIFT AO imaging of APs in vivo.** (A)  $\text{Ca}^{2+}$  responses were recorded with chessboard scanning in an anesthetized mouse. Exemplified  $\text{Ca}^{2+}$  response (green) from the neuron recorded simultaneously with cell-attached pipette (voltage signal: blue). (B) Individual single AP-induced  $\text{Ca}^{2+}$  responses (gray) and average of five responses (black). (C) Exemplified cell-attached voltage signals with 1,2,5 and 10 APs recorded during in vivo conditions. (D) Corresponding somatic  $\text{Ca}^{2+}$  responses.

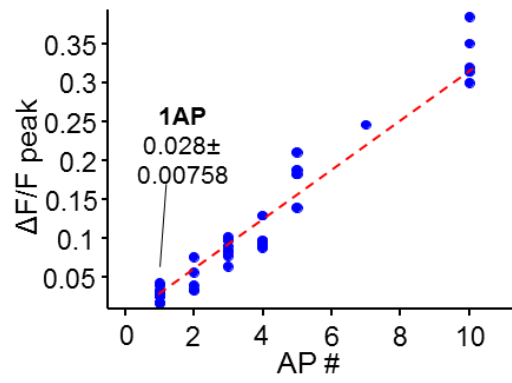


*Figure 57. Simultaneous electro-physiological recording in vivo for calibration. Amplitude of the somatic  $Ca^{2+}$  response as a function of the number of APs.*

### ***6.7 Random equivalent-time sampling, selection of the fluorescent dye***

However 3D AO DRIFT Scanning has an increased scanning speed compared to random access point scanning, its maximum speed is still limited by physical constraints such as the AO cycle or minimum pixel dwell time, the latter is limited both by sampling rate of the electronics and the biological sample since we need certain amount of time to acquire enough fluorescent information. According to these limitations there are biological questions which cannot be sufficiently addressed even with the increased scanning speed of 3D AO DRIFT scanning. Generally speaking drift scanning is a great tool to investigate regenerative events of cellular or subcellular compartments during traces of action potentials, but it cannot resolve the genuine temporal pattern of the actual action potential pattern. In addition, it is not sufficient to retrace the propagation properties of the calcium transients along the neuronal arbors or to investigate calcium inhomogeneity during regenerative events. This limitation can be overcome if the event under investigation is repeated several times with very precise timing, for example action potentials triggered by somatic voltage injection. Under these special circumstances reconstruction of the mean timecourse of transients is possible by adopting random equivalent-time sampling mode of oscilloscopes<sup>29</sup> for 3D fluorescence measurements. Namely, in random-access fluorescence measurements the recording system acquires samples while sequentially jumping through a predefined set of 3D locations, sampling the same location with a defined frequency (sampling rate). One way of determining the mean signal at a given location is simply by averaging each trial using the trigger signal of the optical recording start time. Another way is to use the time of the peak of the somatic AP as time zero (“AP trigger”). When the AP-triggered average of transients is calculated, each trial is shifted “randomly” relative to the others on a very fine time scale due to the biological variability of the trigger (**Figure 58**). Therefore, samples in successive trials are added into equally distributed sub-intervals of the sampling time (**Figure 58A and B**). By plotting the mean $\pm$ SEM values of samples gathered in the sub-intervals as a function of time, the mean waveform of the event can be reconstructed with a higher temporal resolution than that dictated by the sampling rate (74.4 kHz instead of 7.44 kHz, **Figure 58C and D**). Note that if the jitter of the biological signal (here that of the APs) is not enough to generate an efficient random trigger, Ca<sup>2+</sup> measurements can be started randomly to yield a similar result.

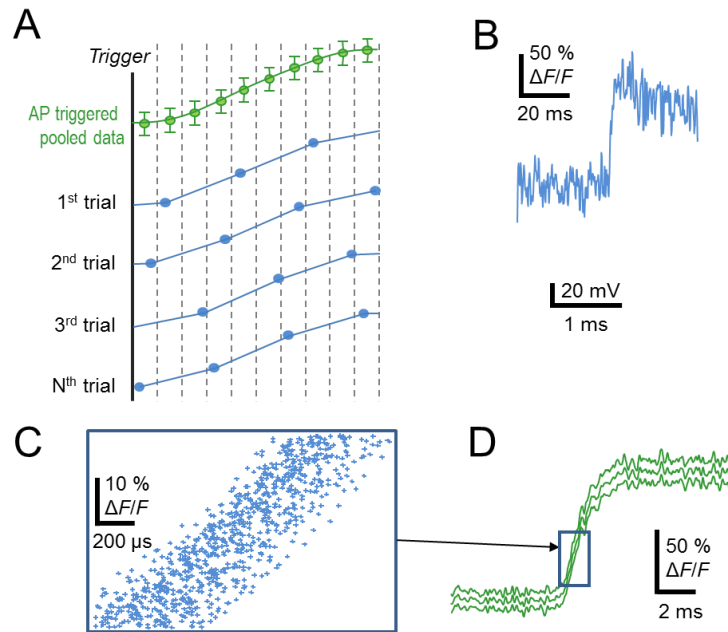


**Figure 58. Method of reconstructing average fluorescence transient curves by adopting a "random equivalent-time sampling mode" from oscilloscope technology.** (A) The temporal phase delay in successive single trials (blue traces) generates measurement points in temporal sub-intervals of the sampling time (sub-intervals are indicated by dotted lines). Temporal sub-intervals were four times smaller than the sampling time in this example. Therefore, the average transient (green trace), calculated as the mean  $\pm$  s.e.m. of the measurement data in the sub-intervals, has a four times higher temporal discretization. The temporal shift of the transients required to generate temporal sub-intervals can be generated both randomly and sequentially. (B) Single Ca<sup>2+</sup> transient measured at 7.44 kHz (top). Somatic APs recorded via the patch pipette (bottom). Their peak time serves as a random trigger for averaging. Ca<sup>2+</sup> transients were shifted backward with the time of the AP peak before averaging. (C) Magnified view of backward-shifted Ca<sup>2+</sup> transient data points gathered in successive trials during the rising phase of the AP. (D) Mean Ca<sup>2+</sup> transient (mean, mean  $\pm$  s.e.m.) was reconstructed with 74.4 kHz and filtered at 32 kHz using a Bessel filter.

I tested the temporal resolution of the 3D microscope further by measuring the propagation speed of bAPs. A somatic AP was evoked in a pyramidal cell held under current clamp while scanning in 3D along its dendrite. Extracellular cell-attached electric recordings were correlated with the acquired optical recordings of the matching dendritic locations (**Figure 59C**). The bAP-evoked Ca<sup>2+</sup> transients showed increasing latency along the dendrite away from the cell body (**Figure 59D and F**). Note the sensitivity of the extracellular voltage signal to the first derivative peak of the local membrane voltage. The temporal delays between the onset of somatic versus dendritic Ca<sup>2+</sup> transients ( $\Delta t'$ , **Figure 59D**) were similar to the delays measured by extracellular recording ( $\Delta t$ ) in the same locations (*t*-test,  $P > 0.3$ ,  $n = 5$  cells), validating the optical measurements. I could also follow the bAP by detecting the peak of the first derivative

of the  $\text{Ca}^{2+}$  transients at different spatial positions (**Figure 59E**). The velocity of the bAP was calculated from the slope of the optical transient onset versus dendritic distance curve (**Figure 59G**). Average propagation speed was different at 23°C and 33°C ( $164 \pm 13 \mu\text{m}/\text{ms}$  vs.  $227 \pm 14 \mu\text{m}/\text{ms}$ ;  $n = 9$ ,  $n = 13$ , respectively;  $P < 0.05$ ,  $t$ -test, **Figure 59H**).

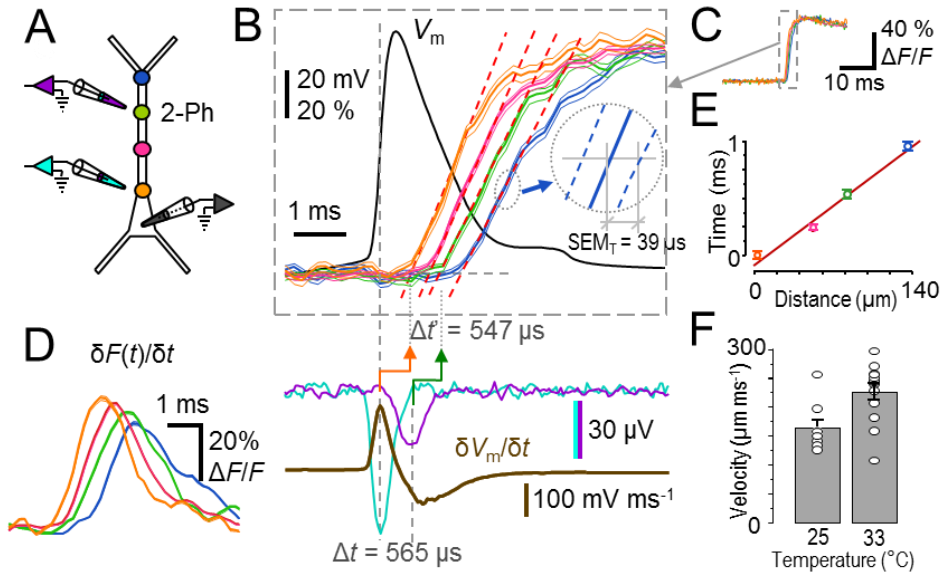


**Figure 59. Signal propagation speed measurements** (A) *Experimental arrangement.* Speed signal propagation was measured by somatic whole-cell current-clamp ( $V_m$ , black), cell-attached current-clamp (cyan, purple) and 3D two-photon (2-Ph) calcium imaging (orange, pink, green, blue). The same color-coding is used in A-E. (B) *Top, Triggered AP peak and averaged and normalized back-propagating calcium transients (mean  $\pm$  s.e.m.;  $n = 54$ ). Linear fits (red dashed lines) define onset latency times. Maximal temporal resolution achieved:  $39 \mu\text{s}$  ( $\text{SEM}_T$ , Inset). Bottom, Cell-attached somatic voltage recording (cyan) peaked at the maximum of the derivate ( $\delta V_m / \delta t$ ) of  $V_m$  (brown trace). Somatic (orange) versus dendritic (green)  $\text{Ca}^{2+}$  transients and position-matched cell-attached signals (dendritic: magenta; somatic: cyan). Arrows point to the lag of the  $\text{Ca}^{2+}$  signals. (D) First derivatives of the  $\text{Ca}^{2+}$  transients shown in B. (E) Onset latency times (mean  $\pm$  s.e.m.) of  $\text{Ca}^{2+}$  transients in B as a function of dendritic distance. Linear fit: average propagation speed. (F) Dendritic propagation speeds at different temperatures ( $n = 5$  cells).*

Next I investigated whether the maximal temporal resolution can be reached by the system. For example if it allows the investigation of rapid action potential backpropagation at a spatial resolution of a few micrometers. This spatial dimension matches the scale of small dendritic computational subunits that have an important function in dendritic integration<sup>2,19,27</sup>. Here, I defined the temporal resolution as the smallest significantly resolvable x-axis delay between two bAP-induced  $\text{Ca}^{2+}$  transients

occurring during the rising period, when the transients were measured simultaneously in two different dendritic locations (**Figure 60**). According to the theoretical prediction, measurements for the highest temporal resolution were performed in two points situated as close as 6-14  $\mu\text{m}$  in the main apical tuft of CA1 pyramidal cells (**Figure 60C**). The best temporal resolution attained when two transients remained significantly different ( $P < 0.05$ ,  $t$ -test) in a temporal interval during the rising phase was 54.7  $\mu\text{s}$  (**Figure 60D**). Not only can temporal latency be measured, but reconstructions of the mean time course of transients is possible by adopting a "random equivalent-time sampling mode" of the oscilloscopes<sup>29</sup> in fast 3D fluorescent measurements (**Figure 58**). The 54.7  $\mu\text{s}$  temporal resolution demonstrated here even allows the measurement of fast regenerative activity at the scale of small dendritic segments.

### 6.7.1 Spatial distance estimate corresponding to the highest temporal resolution in bAP measurements.

Theoretical calculation showed that temporal delay between two transients can be estimated by the  $x$  axis projection of *s.e.m.* (defined as  $\text{SEM}_T$ ). Short, repeated measurements (60 ms,  $n = 100$  traces) were used to improve the  $\text{SEM}_T$  value of transients in the 3D bAP measurements shown in **Figure 59D**, using a fluorescent dye with a high  $\text{Ca}^{2+}$  on-rate constant (Fluo 5F,  $k_{\text{on}} = 2.36 \times 10^8 \mu\text{M}^{-1}\text{ms}^{-1}$ )<sup>1,2</sup>. In this configuration, the best  $\text{SEM}_T$  value achieved was 15.8  $\mu\text{s}$  (**Figure 60B**) which, using

$s.e.m. < \frac{\bar{y}_1 - \bar{y}_2}{2.81}$ , (see detailed calculation below) indicates a  $2.81 \times 15.8 \mu\text{s} = 44.39 \mu\text{s}$

theoretical temporal resolution for  $n = 100$  repeats (see the previous section). In order to be capable of resolving temporal delays between two transients in this range, I measured bAP-induced transients at two points situated as close as 6-14  $\mu\text{m}$  in the main apical tuft of CA1 pyramidal cells (**Figure 60C**). Here, the spatial distance range of the two points was selected according to the speed of bAP in these dendrites.

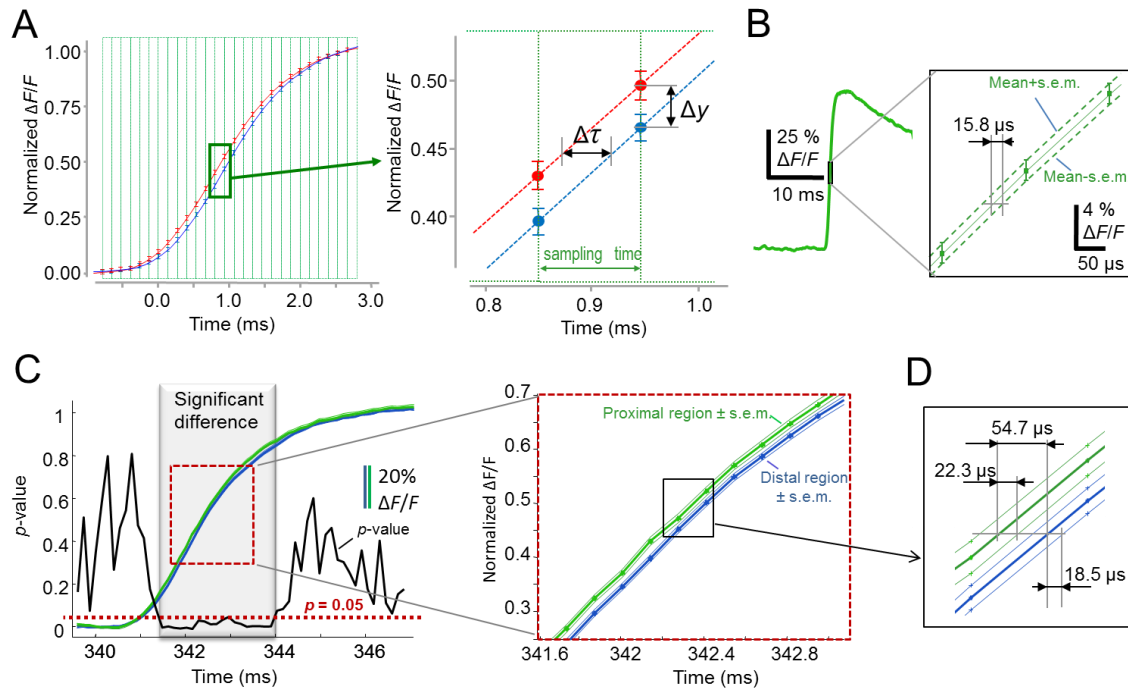


**Figure 60. Visualization of the method to resolve temporal differences in  $\text{Ca}^{2+}$  transients with high temporal resolution** (A) The temporal shift between two transients ( $\Delta\tau$ ) can be calculated

$$\Delta\tau \approx \frac{1}{\tan(\alpha)} \Delta y$$

from the amplitude difference ( $\Delta y$ ) as: , where  $\alpha$  denotes the angle between the  $x$  axis and the linear fit to the transient's rising edge at the given time point. This type of temporal separation requires at least two sampling time points during the rising phase of the transients and, thus, the sampling time should be shorter than the rise time of the fluorescent dye. There is no theoretical limit to the extent of amplitude differentiation, namely  $\Delta y$  could converge to zero at a given time point with increasing trial number; therefore,  $\Delta\tau$  could also converge to zero. But what is the shortest achievable  $\Delta\tau$  value?

(B) The smallest significantly resolvable  $\Delta y$  value ( $\bar{y}_1 - \bar{y}_2$ ) ( $P < 0.05$ , Student's  $t$ -test) can be estimated from the corresponding  $s.e.m.$  values. As  $\Delta y$  can be projected onto the  $x$  axis, the smallest significantly resolvable  $\Delta\tau$  value could be estimated from the temporal difference for mean versus mean +  $s.e.m.$  (or mean versus mean -  $s.e.m.$ ) traces. Left, Recording of bAP-induced  $\text{Ca}^{2+}$  transient with the smallest  $s.e.m.$  value was performed as given in **Figure 59A, B**, but with increased laser energy and trial number (average of  $n = 100$  transients, green traces are mean, mean  $\pm s.e.m.$ ). Enlarged view (right) showing a  $15.8 \mu\text{s}$  temporal difference for mean versus mean -  $s.e.m.$  trace. Therefore, the best temporal resolution achievable for 3D two-photon measurements is estimated as  $2.81 \times 15.8 \mu\text{s} = 44.39 \mu\text{s}$ . (C) In order to measure the best temporal resolution more directly, single bAP-induced  $\text{Ca}^{2+}$  transients were measured simultaneously with  $7.44 \text{ kHz}$  in two dendritic locations situated  $9 \mu\text{m}$  apart in the main apical dendrite of a CA1 pyramidal cell. Black trace shows  $P$  value of the Student's paired  $t$ -test. Note that the two transients measured in proximal (green traces, mean and mean  $\pm s.e.m.$ ) and distal (blue traces, mean and mean  $\pm s.e.m.$ ) dendritic locations are significantly different ( $P < 0.05$ ) in the time interval shown in gray, which coincides with the rising phase of the transients. Enlarged view from the interval of significance shows a temporal delay between the two transients (right, red dotted box). (D) A further magnification shows  $54.7 \mu\text{s}$  temporal delay between the two transients, and  $18.5 \mu\text{s}$  and  $22.3 \mu\text{s}$  temporal differences between mean and mean -  $s.e.m.$  traces

### 6.7.2 Theoretical calculation of the maximal temporal resolution.

In order to determine the maximal temporal resolution of the 3D measurements, I calculated the theoretical value of the temporal resolution, and also performed validating two-photon measurements.

Let's define

$$y_{11}, y_{12}, y_{13}, \dots, y_{1n_1}$$

and

$$y_{21}, y_{22}, y_{23}, \dots, y_{2n_2}$$

as fluorescent data measured within a single sampling period, whose length is characterized by the acquisition rate, in two separate spatial locations (1 and 2). The  $y_{ij}$  values are elements of two normal (or Gaussian) distributions characterized with  $\mu_1, \sigma_1^2$  and  $\mu_2, \sigma_2^2$ , respectively, where parameter  $\mu$  is the mean and  $\sigma^2$  is the variance. For simplicity I calculate for  $\sigma_1 = \sigma_2$ .

Let's have

$$\bar{y}_1 = \frac{1}{n_1} \sum_{i=1}^{n_1} y_{1i}, \quad (\text{Equation 29})$$

$$\bar{y}_2 = \frac{1}{n_2} \sum_{i=1}^{n_2} y_{2i}, \quad (\text{Equation 30})$$

$$s_1^2 = \frac{1}{n_1} \sum_{i=1}^{n_1} (y_{1i} - \bar{y}_1)^2, \quad (\text{Equation 31})$$

$$s_2^2 = \frac{1}{n_2} \sum_{i=1}^{n_2} (y_{2i} - \bar{y}_2)^2, \quad (\text{Equation 32})$$

$$t = \sqrt{\frac{n_1 n_2 (n_1 + n_2 - 2)}{n_1 + n_2}} \times \frac{\bar{x}_1 - \bar{x}_2 - (\mu_1 - \mu_2)}{\sqrt{n_1 s_1^2 + n_2 s_2^2}}, \quad (\text{Equation 33})$$

where  $t$  is a Student's distribution with  $n_1+n_2-2$  degrees of freedom<sup>15</sup>. In our simultaneous measurements  $n_1 = n_2$ , and the standard error of the mean is calculated as

$$s.e.m._i = \frac{s_i}{\sqrt{n}}, \text{ therefore}$$

$$t = \sqrt{\frac{n-1}{n}} \times \frac{\bar{y}_1 - \bar{y}_2}{\sqrt{s.e.m._1^2 + s.e.m._2^2}}, \quad (\text{Equation 34})$$

which can be estimated at relatively large  $n$  as

$$t = \underbrace{\sqrt{\frac{n-1}{n}}}_{1} \times \frac{\bar{x}_1 - \bar{x}_2}{\underbrace{\sqrt{(s.e.m._1)^2 + (s.e.m._2)^2}}_{\sqrt{2} \cdot s.e.m.}} \approx \frac{1}{\sqrt{2}} \frac{\bar{y}_1 - \bar{y}_2}{s.e.m.} \quad (\text{Equation 35})$$

where  $s.e.m.$  denotes the average standard error of the mean fluorescence provided by the system in a given sampling period in a given spatial location.

In Student's  $t$ -test the  $\mu_1 \neq \mu_2$  hypothesis is accepted significant if

$$|t| > t_p, \quad (\text{Equation 36})$$

where  $t_p$  is defined as  $P(|t| > t_p) = p$ , where  $P$  denotes probability. The Student's distribution defines  $t_p$  at the given  $p$  and degree of freedom ( $2n - 2$ ). The **Equation 35** takes shape as

$$\sqrt{2} \times t_p \times s.e.m. < \bar{y}_1 - \bar{y}_2, \quad (\text{Equation 37})$$

therefore  $s.e.m.$  can be used as an indicator for statistical significance in our measurements. If  $n$  is larger than 10,  $t_p$  is typically about 2, ranging between 2.101 and 1.98 in biologically relevant  $n$  values ( $n = 10$  and  $n = 100$ , respectively)

For example,

$$s.e.m. < \frac{\bar{y}_1 - \bar{y}_2}{2.81}, \quad (\text{Equation 38})$$

is required for statistical significance at  $n = 100$  measurements.

I defined the highest temporal resolution as the smallest significantly resolvable  $x$  axis delay between two transients during the rising phase period, when the transients were measured simultaneously in two different dendritic locations (**Figure 60A**). If two traces measured at location 1 and 2 are significantly different (namely,  $P$  value of  $t$ -test was less than 0.05) in amplitudes in a given time interval, the significant amplitude difference  $\Delta y = \bar{y}_1 - \bar{y}_2$  and the corresponding  $s.e.m.$  values can be "transformed" (projected) to temporal difference using **Equation 38**, therefore the temporal delay between two transients can be estimated by the  $x$  axis projection of  $s.e.m.$  (defined as  $SEM_T$ ).

Using this equation for  $n = 100$  measurement and Fluo 5F the shortest measurable temporal delay is  $44.39 \mu\text{s}$  that, by the propagation speeds indicated on **Figure 59**, means that we can resolve temporal delays between two transients in this range, we measured bAP-induced transients at two points situated as close as  $6\text{-}14 \mu\text{m}$  in the main apical tuft of CA1 pyramidal cells. This well met the experimental data represented on **Figure 60**, where we see temporal differences at point  $9 \mu\text{m}$  apart.

The use of random-equivalent time sampling method is not exclusive to AO scanning and could increase temporal resolution also for other scanning methods, however the increase in scanning speed would be as larger as for AO scanning since we although we can have better temporal resolution we still have to follow a fix scanning line for example with galvo scanning.

## 7 CONCLUSION

---

With the optical developments detailed here, including material dispersion compensation, motorizing the prism compressor, the application of the angular dispersion compensation lens, optimization of AO deflectors for longer wavelength replacement of multiple optical elements for higher transmittance efficiency and stabilization of the laser beam's position, we have improved the optical resolution and transmittance efficiency of the system, also made it possible to image at longer wavelengths, required for imaging of genetically encoded indicators. With these improvements the field or volume of view to  $500\ \mu\text{m} \times 500\ \mu\text{m} \times 650\ \mu\text{m}$  with GCaMP6 sensor from behaving animals, which allows the measurement of hundreds of cells simultaneously while the elimination of angular and material dispersion made the somatic measurement reliable through the entire volume.

With random equivalent-time sampling method using 100 repeats from a given event, we can measure the propagation of a calcium transient along  $10\text{-}20\ \mu\text{m}$  along a single dendritic segment, allowing the study of signal integration on the subcellular domains. Using this technology, we were able to show the difference of  $\text{Ca}^{2+}$  signal propagation between room temperature and physiological conditions. The traceable different indicating that the selection of the proper bath temperature might have an influence of the integration properties measured on a dendritic segment.

With the presented novel 3D DRIFT AO scanning technology, we have generated novel 3D scanning methods: 3D ribbon scanning; chessboard scanning; multi-layer, multi-frame imaging; snake scanning; multi-cube scanning; and multi-3D line scanning in large scanning volumes (See **Figure 46** for summary of the scanning methods). Our methods allow, for the first time, high-resolution 3D measurements of neuronal networks at the level of tiny neuronal processes, such as spiny dendritic segments, in awake, behaving animals, even under conditions when large-amplitude motion artifacts are generated by physical movement.

### 7.1 *Benefits of the new 3D methods in neuroscience*

We demonstrate several further technical advances over previous 3D methods in the present work, i) it enables a scanning volume with GECIs which is more than two orders of magnitude larger than previous realizations, while the spatial resolution remains preserved; ii) it offers a method of fast 3D scanning in any direction, with an arbitrary velocity, without any sampling rate limitation; iii) it is free of mechanical and electrical inertias which makes it possible to flexibly select surface and volume elements matching multiple somatic and dendritic locations, thereby effectively focusing measurement time to the ROIs; iv) it compensates fast motion artifacts in 3D to preserve high spatial resolution, characteristic to two-photon microscopy, during 3D surface scanning and volume imaging even in behaving animals; and v) it enables generalization of the low-power temporal oversampling (LOTOS) strategy of 2D raster scanning (Chen et al., 2011) in fast 3D AO measurements to reduce phototoxicity.

When raster scanning of the entire cubature is replaced with 3D DRIFT AO scanning, the  $v_{gain} * (SNR_{gain})^2$  is proportional to the ratio of the overall cubature versus the volume covered by the scanned ROIs, and this ratio can be very high (up to  $10^6$ ). Therefore, the flexibility in selection of ROIs results in an increase in speed and/or SNR of several orders of magnitude. For example, the measurement of 136 neurons with 25 x 25 frames, instead of imaging the entire cubature, results in an  $SNR_{gain}$  that is about 25-fold higher when the measurement speed is constant and, vice versa, the measurement speed is about 600-fold higher while keeping the SNR constant.

These technical achievements enabled the realization of the following fast 3D measurements and analysis methods in awake, behaving animals: i) simultaneous functional recording of over 150 spines; ii) fast parallel imaging of activity in over 12 spiny dendritic segments; iii) precise separation of fast signals in space and time from each individual spine (and dendritic segment) from the recorded volume, in which signals overlap with the currently available methods; iv) simultaneous imaging of large parts of the dendritic arbor and neuronal networks in a z scanning range of over 650  $\mu\text{m}$ ; v) imaging a large network of over 100 neurons at subcellular resolution in a scanning volume of up to 500  $\mu\text{m} \times 500 \mu\text{m} \times 650 \mu\text{m}$  with the SNR more than an order of magnitude larger than for 3D random-access point scanning; and vi) more than 10-fold better single AP resolution during motion in neuronal network measurements.

The limits of our understanding of neural processes lie now at the fast dendritic and neuronal activity patterns occurring in living tissue in 3D, and their integration over larger network volumes. Until now, these aspects of neural circuit function have not been measured in awake, behaving animals. Our new 3D scanning methods, with preserved high spatial and temporal resolution, provide the missing tool for these activity measurements. Among other advantages, it will be possible to use these methods to investigate spike-timing-dependent plasticity and the underlying mechanisms during *in vivo* conditions<sup>61,62,63</sup>, the origin of dendritic regenerative activities<sup>55,57</sup>, the propagation of dendritic spikes<sup>2,14,58</sup>, receptive field structures<sup>64</sup>, dendritic computation between multiple spiny and aspiny dendritic segments<sup>6,58</sup>, spatiotemporal clustering of different input assemblies<sup>2,65</sup>, associative learning<sup>66</sup>, multisensory integration<sup>67</sup>, the spatial and temporal structure of the activity of spine, dendritic, and somatic assemblies<sup>68,69,70</sup>, and function and interaction of sparsely distributed neuronal populations, such as parvalbumin-, somatostatin-, and vasoactive intestinal polypeptide-expressing neurons<sup>71,72</sup>. These 3D scanning methods may also provide the key to understanding synchronization processes mediated by neuronal circuitry locally and on a larger scale: these are thought to be important in the integrative functions of the nervous system<sup>73</sup> or in different diseases<sup>74</sup>. Importantly, these complex functional questions can be addressed using our methods at the cellular and sub-cellular level, and simultaneously at multiple spiny (or aspiny) dendritic segments, and at the neuronal network level in behaving animals.

## **7.2 *Imaging brain activity during motion***

Two-dimensional *in vivo* recording of spine  $\text{Ca}^{2+}$  responses have already been realized in anaesthetized animals<sup>75</sup> and even in running animals, but in these papers only a few spines were recorded with a relatively low SNR<sup>76,77</sup>. However, fast 2D and 3D imaging of large spine assemblies and spiny dendritic segments in awake, running, and behaving animals has remained a challenge. Yet this need is made clear by recent work showing that the neuronal firing rate more than doubles in most neurons during locomotion, suggesting a completely altered neuronal function in behaving animals<sup>44,46</sup>. Moreover, the majority of neuronal computation occurs in distant apical and basal dendritic segments which form complex 3D arbors in the brain<sup>55,56,57,78,79,80</sup>. However, none of the

previous 2D and 3D imaging methods have been able to provide access to these complex and thin (spiny) dendritic segments during running periods, or in different behavioral experiments, despite the fact that complex behavioral experiments are rapidly spreading in the field of neuroscience<sup>81,82</sup>. One reason is that, in a typical behavioral experiment, motion-induced fluorescence transients have similar amplitude and kinetics as behavior-related  $\text{Ca}^{2+}$  transients. Moreover, these transients typically appear at the same time during the tasks, making their separation difficult. Therefore, the 3D scanning methods demonstrated here, alone or in different combinations, will add new tools that have long been missing from the toolkit of neurophotonic for recording dendritic activity in behaving animals.

### ***7.3 Compensation of movement of the brain***

Although closed-loop motion artifact compensation, with three degrees of freedom, has already been developed at low speed ( $\approx 10$  Hz)<sup>34</sup>, the efficiency of the method has not been demonstrated in awake animals, or in dendritic spine measurements, or at higher speeds characteristic of motion artifacts. Moreover, due to the complex arachnoidal suspension of the brain, and due to the fact that blood vessels generate spatially inhomogeneous pulsation in their local environment, the brain also exhibits significant deformation, not merely translational movements and, therefore, the amplitude of displacement could be different in each and every sub-region imaged. This is crucial when small-amplitude somatic responses (for example single or a few AP-associated responses) or small structures such as dendritic spines are measured. Fortunately, our 3D imaging and the corresponding analysis methods also allow compensation with variable amplitude and direction in each sub-region imaged, meaning that inhomogeneous displacement distributions can therefore be measured and effectively compensated in 3D.

The efficiency of our 3D scanning and motion artifact compensation methods is also validated by the fact that the standard deviation of individual somatic  $\text{Ca}^{2+}$  transients was largely reduced (up to 20-fold), and became smaller than the amplitude of a single AP-induced transient, especially when multi-cube or chessboard scanning was used. This allows single AP resolution in the moving brain of behaving animals using the currently favored GEPI, GCaMP6f. The importance of providing single AP resolution

for neuronal network imaging has also been validated by recent works which have demonstrated that in many systems neuronal populations code information with single APs instead of bursts<sup>82</sup>.

#### **7.4 Simultaneous 3D imaging of apical and basal dendritic arbor**

Recent data have demonstrated that the apical dendritic tuft of cortical pyramidal neurons is the main target of feedback inputs, where they are amplified by local NMDA spikes to reach the distal dendritic  $\text{Ca}^{2+}$  and, finally, the somatic sodium integration points where they meet basal inputs also amplified by local NMDA spikes<sup>6,57</sup>. Therefore, the majority of top-down and bottom-up input integration occurs simultaneously at local integrative computational subunits separated by distances of several hundred micrometers, which demands the simultaneous 3D imaging of neuronal processes in a z range of several hundred micrometers. The maximal, over 1000  $\mu\text{m}$  z-scanning range of AO microscopy<sup>2</sup>, which is limited during *in vivo* measurements with GECIs to about 650  $\mu\text{m}$  by the maximal available power of the currently available lasers, already permitted the simultaneous measurement of apical and basal dendritic segments of layer II/III neurons and dendritic segments of layer V neurons in a range of over 500  $\mu\text{m}$ .

Although 2D imaging in anesthetized animals can capture long neuronal processes<sup>75</sup>, the location of horizontally oriented long segments is almost exclusively restricted to a few layers (for example to layer I), and in all other regions we typically see only the cross-section or short segments of obliquely or orthogonally oriented dendrites. Moreover, even in cases when we luckily capture multiple short segments with a single focal plane, it is impossible to move the imaged regions along dendrites and branch points to understand the complexity of spatiotemporal integration. The main advantage of the multi-3D ribbon and snake scanning methods is that any ROI can be flexibly selected, shifted, tilted, and aligned to the ROIs; this means that complex dendritic integration processes can be recorded in a spatially and temporally precise manner.

#### **7.5 Deep imaging**

Although there are many effective methods for fast volume scanning such as SPIM<sup>83</sup>, DSLM-SI, SimView<sup>19</sup>, SCAPE<sup>84</sup>, and OPLUL<sup>23</sup>, which have broad application spectra,

the z-scanning range of *in vivo* functional measurements in mice is currently limited to about 130  $\mu\text{m}$  in case of these technologies. Imaging deep layer neurons is possible only by either causing mechanical injury<sup>85</sup> or using single-point two-photon or three-photon excitation which allows fluorescent photons scattered from the depth to be collected<sup>31,86</sup>. One of the main advantages of 3D DRIFT AO scanning is that it is based on whole-field detection, and the extended fast z-scanning range is over 1100  $\mu\text{m}$  in transparent samples and about 650  $\mu\text{m}$  during functional *in vivo* imaging in mouse brain (limited by the power of the laser). Using adaptive optics and regenerative amplifiers can improve resolution and SNR at depth<sup>87,88</sup>. Moreover, using GaAsP photomultipliers installed directly in the objective arms (travelling detector system) can itself extend the *in vivo* scanning range to over 800  $\mu\text{m}$ . One of the main perspectives of the 3D scanning methods demonstrated here is that the main limitation to reach the maximal scanning ranges of over 1.6 mm<sup>32,33,86</sup> is the relatively low laser intensity of the currently available lasers. Supporting this over a 3 mm z-scanning range has already been demonstrated with 3D AO imaging in transparent samples, where intensity and tissue scattering is not limiting<sup>2</sup>. Therefore with future high-power lasers, combined with fast adaptive optics and new red-shifted sensors, may allow a much larger 3D scanning range to be utilized which will, for example, permit the measurement of the entire arbor of deep-layer neurons or 3D hippocampal imaging, without removing any tissue from the cortex.

Although there are several different arrangements of passive optical elements and the four AO deflectors with which it is possible to build microscopes for fast 3D scanning<sup>2,14,34,58</sup>, all of these microscopes use drift compensation with counter-propagating AO waves at the second group of deflectors. The scanning methods demonstrated here can therefore easily be implemented in all 3D AO microscopes. Moreover, at the expense of a reduced scanning volume, 3D AO microscopes could be simplified<sup>14</sup> and used as an upgrade in any two-photon system. Hence we anticipate that our new methods will open new horizons in high-resolution *in vivo* imaging in behaving animals.

### ***Credit assignment***

I have adopted the methods used in our lab with the help of Daniel Hillier, Attila Kaszás, Linda Judák, Zoltán Szadai and Zoltán Farkas. Pál Maák worked out the design of the acousto optical deflectors, me, Pál Maák, Máté Veress and András Fehér are contributed to the optical design and assemble. I made all calculation and optical design for material dispersion compensation. Calculation for angular dispersion compensation are performed by Pál Maák, realization was performed by all who contributed in the optical assemble. Software and motion correction is written by Gergely Katona and Katalin Ócsai. I have performed all type of measurement listed through the work with the help of Linda Judák, Attila Kaszás and Balázs Chiovini and Balázs Rózsa. Balázs Rózsa, Maák Pál, Gergely Katona and Linda Judák helped me with analysis. Novel scanning method for in vivo motion corrections are designed by me, Gergely Katona and Balázs Rózsa. I have designed and performed both quality increment and motion-detection simulations. In vivo patch clamp measurements were performed by me, Linda Judák and Gábor Juhász.

## 8 SUMMARY

---

With the optical developments detailed in this work we have improved the optical resolution and transmittance efficiency of the system, also made it possible to image at longer wavelengths, required for imaging of genetically encoded indicators from a field or volume of view up to  $500\ \mu\text{m} \times 500\ \mu\text{m} \times 650\ \mu\text{m}$  from behaving animals.

With random equivalent-time sampling method using 100 repeats from a given event, we can measure the propagation of a calcium transient along 10-20  $\mu\text{m}$  along a single dendritic segment, allowing the study of signal integration on the subcellular domains. Using this technology, we were able to show the difference of  $\text{Ca}^{2+}$  signal propagation between room temperature and physiological conditions. The traceable difference indicating that the selection of the proper bath temperature might have an influence of the integration properties measured on a dendritic segment.

With the presented novel 3D DRIFT AO scanning technology, we have generated novel 3D scanning methods: 3D ribbon scanning; chessboard scanning; multi-layer, multi-frame imaging; snake scanning; multi-cube scanning; and multi-3D line scanning in large scanning volumes. Our methods allow, for the first time, high-resolution 3D measurements of neuronal networks at the level of tiny neuronal processes, such as spiny dendritic segments, in awake, behaving animals, even under conditions when large-amplitude motion artifacts are generated by physical movement.

## 9 ÖSZEFOGLALÁS

---

A 3D véletlen elérésű AO mikroszkóp kézenfekvő előnyei mellett ennek a szkennelési módnak van néhány korlátja, amikor éber, viselkedő egerekből szeretnénk hosszú időn keresztül méréseket végezni, mivel ezeknél a kísérleteknél a hosszú távú stabilitásnak kiemelt jelentősége van. Munkám során meghatároztam ezeket a korlátozó tényezőket és a dolgozatban lehetséges megoldási módszert kínáltam mindegyikre.

## 10 REFERENCES

---

1. Scanziani M, Hausser M (2009) Electrophysiology in the age of light. *Nature* 461:930-939.
2. Katona G, Szalay G, Maak P, Kaszas A, Veress M, Hillier D, Chiovini B, Vizi ES, Roska B, Rozsa B (2012) Fast two-photon in vivo imaging with three-dimensional random-access scanning in large tissue volumes. *Nature methods* 9:201-208.
3. Khodagholy D, Gelinas JN, Thesen T, Doyle W, Devinsky O, Malliaras GG, Buzsaki G (2015) NeuroGrid: recording action potentials from the surface of the brain. *Nature neuroscience* 18:310-315.
4. Poirazi P, Brannon T, Mel BW (2003) Pyramidal neuron as two-layer neural network. *Neuron* 37:989-999.
5. Polsky A, Mel BW, Schiller J (2004) Computational subunits in thin dendrites of pyramidal cells. *Nature neuroscience* 7:621-627.
6. Losonczy A, Magee JC (2006) Integrative properties of radial oblique dendrites in hippocampal CA1 pyramidal neurons. *Neuron* 50:291-307.
7. Johnston D, Narayanan R (2008) Active dendrites: colorful wings of the mysterious butterflies. *Trends in neurosciences* 31:309-316.
8. Danilatos GD (1991) Review and outline of environmental SEM at present. *Journal of microscopy* 162:391-402.
9. Kerr JN, Denk W (2008) Imaging in vivo: watching the brain in action. *Nat Rev Neurosci* 9:195-205.
10. Kherlopian AR, Song T, Duan Q, Neimark MA, Po MJ, Gohagan JK, Laine AF (2008) A review of imaging techniques for systems biology. *BMC systems biology* 2:74.
11. Nikolenko V, Watson BO, Araya R, Woodruff A, Peterka DS, Yuste R (2008) SLM Microscopy: Scanless Two-Photon Imaging and Photostimulation with Spatial Light Modulators. *Front Neural Circuits* 2:5.
12. Grewe BF, Voigt FF, van 't Hoff M, Helmchen F (2011) Fast two-layer two-photon imaging of neuronal cell populations using an electrically tunable lens. *Biomedical optics express* 2:2035-2046.
13. Duemani Reddy G, Kelleher K, Fink R, Saggau P (2008) Three-dimensional random access multiphoton microscopy for functional imaging of neuronal activity. *Nat Neurosci* 11:713-720.
14. Fernandez-Alfonso T, Nadella KM, Iacaruso MF, Pichler B, Ros H, Kirkby PA, Silver RA (2014) Monitoring synaptic and neuronal activity in 3D with synthetic and genetic indicators using a compact acousto-optic lens two-photon microscope. *J Neurosci Methods* 222:69-81.
15. Cheng A, Goncalves JT, Golshani P, Arisaka K, Portera-Cailliau C (2011) Simultaneous two-photon calcium imaging at different depths with spatiotemporal multiplexing. *Nature methods* 8:139-142.
16. Holekamp TF, Turaga D, Holy TE (2008) Fast three-dimensional fluorescence imaging of activity in neural populations by objective-coupled planar illumination microscopy. *Neuron* 57:661-672.
17. Botcherby EJ, Smith CW, Kohl MM, Debarre D, Booth MJ, Juskaitis R, Paulsen O, Wilson T (2012) Aberration-free three-dimensional multiphoton imaging of neuronal activity at kHz rates. *Proceedings of the National Academy of Sciences of the United States of America* 109:2919-2924.
18. Gobel W, Kampa BM, Helmchen F (2007) Imaging cellular network dynamics in three dimensions using fast 3D laser scanning. *Nature methods* 4:73-79.
19. Tomer R, Khairy K, Amat F, Keller PJ (2012) Quantitative high-speed imaging of entire developing embryos with simultaneous multiview light-sheet microscopy. *Nature methods* 9:755-763.

20. Wolf S, Supatto W, Debregeas G, Mahou P, Kruglik SG, Sintès JM, Beaurepaire E, Candelier R (2015) Whole-brain functional imaging with two-photon light-sheet microscopy. *Nature methods* 12:379-380.
21. Rozsa B, Katona G, Vizi ES, Varallyay Z, Saghy A, Valenta L, Maak P, Fekete J, Banyasz A, Szipocs R (2007) Random access three-dimensional two-photon microscopy. *Applied optics* 46:1860-1865.
22. Prevedel R, Yoon YG, Hoffmann M, Pak N, Wetzstein G, Kato S, Schrodell T, Raskar R, Zimmer M, Boyden ES, Vaziri A (2014) Simultaneous whole-animal 3D imaging of neuronal activity using light-field microscopy. *Nature methods* 11:727-730.
23. Kong L, Tang J, Little JP, Yu Y, Lammermann T, Lin CP, Germain RN, Cui M (2015) Continuous volumetric imaging via an optical phase-locked ultrasound lens. *Nature methods* 12:759-762.
24. Quirin S, Jackson J, Peterka DS, Yuste R (2014) Simultaneous imaging of neural activity in three dimensions. *Frontiers in neural circuits* 8:29.
25. Amos WB, White JG, Fordham M (1987) Use of confocal imaging in the study of biological structures. *Appl Opt* 26:3239-3243.
26. Minsky M (1988) Memoir on inventing the confocal scanning microscope. *Scanning* 10:128-138.
27. Petráň M, Hadravský M, Egger MD, Galambos R (1968) Tandem-Scanning Reflected-Light Microscope. *J Opt Soc Am* 58:661-664.
28. Denk W, Svoboda K (1997) Photon upmanship: why multiphoton imaging is more than a gimmick. *Neuron* 18:351-357.
29. Goepfert-Mayer M (1931) Ueber Elementarakte mit zwei Quantenspruengen. *Ann Phys* 9:273.
30. Denk W, Strickler JH, Webb WW (1990) Two-photon laser scanning fluorescence microscopy. *Science* 248:73-76.
31. Helmchen F, Denk W (2005) Deep tissue two-photon microscopy. *Nat Methods* 2:932-940.
32. Kobat D, Horton NG, Xu C (2011) In vivo two-photon microscopy to 1.6-mm depth in mouse cortex. *J Biomed Opt* 16:106014.
33. Theer P, Hasan MT, Denk W (2003) Two-photon imaging to a depth of 1000 microm in living brains by use of a Ti:Al<sub>2</sub>O<sub>3</sub> regenerative amplifier. *Opt Lett* 28:1022-1024.
34. Cotton RJ, Froudarakis E, Storer P, Saggau P, Tolia AS (2013) Three-dimensional mapping of microcircuit correlation structure. *Front Neural Circuits* 7:151.
35. Katona Gergely (2014) Fast three-dimensional two-photon scanning methods for studying neuronal physiology on cellular and network level. Doctoral dissertation
36. Kaplan A, Friedman N, Davidson N (2001) Acousto-optic lens with very fast focus scanning. *Opt Lett* 26:1078-1080.
37. Kirkby PA, Srinivas Nadella KM, Silver RA (2010) A compact Acousto-Optic Lens for 2D and 3D femtosecond based 2-photon microscopy. *Opt Express* 18:13721-13745.
38. Reddy GD, Saggau P (2005) Fast three-dimensional laser scanning scheme using acousto-optic deflectors. *J Biomed Opt* 10:064038.
39. Iyer V, Hoogland TM, Saggau P (2006) Fast functional imaging of single neurons using random-access multiphoton (RAMP) microscopy. *J Neurophysiol* 95:535-545.
40. Chen TW, Wardill TJ, Sun Y, Pulver SR, Renninger SL, Baohan A, Schreiter ER, Kerr RA, Orger MB, Jayaraman V, Looger LL, Svoboda K, Kim DS (2013) Ultrasensitive fluorescent proteins for imaging neuronal activity. *Nature* 499:295-300.
41. Hillier D., Fiscella M., Drinnenberg A, Trenholm S, Rompani SB., Raics Z, Katona G, Juetter J, Hierlemann A, Rozsa B, Roska B. (2017) Causal evidence for retina-dependent and -independent visual motion computations in mouse cortex. *Nature Neuroscience* 20, 960–968.
42. Horton N, Wang K, Kobat D, Clark CG, Wise FW, Schaffer C, Xu C (2013) In vivo three-photon microscopy of subcortical structures within an intact mouse brain. *Nature Photonics* 7, 205–209.

43. Nimmerjahn, A., Kirchhoff, F., Kerr, J. N. & Helmchen, F. (2004) Sulforhodamine 101 as a specific marker of astroglia in the neocortex in vivo. *Nat Methods* 1, 31-37.
44. Niell CM, Stryker MP (2010) Modulation of visual responses by behavioral state in mouse visual cortex. *Neuron* 65:472-479.
45. Barth AL, Poulet JF (2012) Experimental evidence for sparse firing in the neocortex. *Trends in neurosciences* 35:345-355.
46. Fu Y, Tucciarone JM, Espinosa JS, Sheng N, Darcy DP, Nicoll RA, Huang ZJ, Stryker MP (2014) A cortical circuit for gain control by behavioral state. *Cell* 156:1139-1152.
47. Greenberg DS, Kerr JN (2009) Automated correction of fast motion artifacts for two-photon imaging of awake animals. *Journal of neuroscience methods* 176:1-15.
48. Cang J, Kalatsky VA, Lowel S, Stryker MP (2008) Optical imaging of the intrinsic signal as a measure of cortical plasticity in the mouse. *Visual Neuroscience* 22:685-691.
49. Goldey GJ, Roumis DK, Glickfeld LL, Kerlin AM, Reid RC, Bonin V, Schafer DP, Andermann ML (2014) Removable cranial windows for long-term imaging in awake mice. *Nature protocols* 9:2515-2538.
50. Tang S, Krasieva TB, Chen Z, Tempea G, Tromberg BJ (2006) Effect of pulse duration on two-photon excited fluorescence and second harmonic generation in nonlinear optical microscopy. *J Biomed Opt.* 2006 Mar-Apr;11(2).
51. Proctor, B. & Wise, F. Quartz prism sequence for reduction of cubic phase in a mode-locked Ti:Al(2)O(3) laser. *Opt Lett* 17, 1295-1297 (1992).
52. Mecseki Katalin (2009) Impulzusformáló eszközök diszperziójának valósidejű kontrollja spektrális interferometriával, TDK dolgozat
53. Mihajlik G, Barocsi A, Maak P (2014) Complex, 3D modeling of the acousto-optical interaction and experimental verification. *Optics express* 22:10165-10180.
54. Kaifosh P, Zaremba JD, Danielson NB, Losonczy A (2014) SIMA: Python software for analysis of dynamic fluorescence imaging data. *Frontiers in neuroinformatics* 8:80.
55. Schiller J, Major G, Koester HJ, Schiller Y (2000) NMDA spikes in basal dendrites of cortical pyramidal neurons. *Nature* 404:285-289.
56. Magee JC, Johnston D (2005) Plasticity of dendritic function. *Current opinion in neurobiology* 15:334-342.
57. Larkum ME, Nevian T, Sandler M, Polsky A, Schiller J (2009) Synaptic integration in tuft dendrites of layer 5 pyramidal neurons: a new unifying principle. *Science* 325:756-760.
58. Chiovini B, Turi GF, Katona G, Kaszas A, Palfi D, Maak P, Szalay G, Szabo MF, Szabo G, Szadai Z, Kali S, Rozsa B (2014) Dendritic spikes induce ripples in parvalbumin interneurons during hippocampal sharp waves. *Neuron* 82:908-924.
59. Tran-Van-Minh A, Caze RD, Abrahamsson T, Cathala L, Gutkin BS, DiGregorio DA (2015) Contribution of sublinear and supralinear dendritic integration to neuronal computations. *Frontiers in cellular neuroscience* 9:67.
60. Araya R (2014) Input transformation by dendritic spines of pyramidal neurons. *Frontiers in neuroanatomy* 8:141.
61. Bloodgood BL, Sabatini BL (2007) Ca(2+) signaling in dendritic spines. *Current opinion in neurobiology* 17:345-351.
62. Harvey CD, Yasuda R, Zhong H, Svoboda K (2008) The spread of Ras activity triggered by activation of a single dendritic spine. *Science* 321:136-140.
63. Sjostrom PJ, Rancz EA, Roth A, Hausser M (2008) Dendritic excitability and synaptic plasticity. *Physiological reviews* 88:769-840.
64. Ohki K, Chung S, Ch'ng YH, Kara P, Reid RC (2005) Functional imaging with cellular resolution reveals precise micro-architecture in visual cortex. *Nature* 433:597-603.
65. Larkum ME, Nevian T (2008) Synaptic clustering by dendritic signalling mechanisms. *Current opinion in neurobiology* 18:321-331.
66. Kastellakis G, Cai DJ, Mednick SC, Silva AJ, Poirazi P (2015) Synaptic clustering within dendrites: an emerging theory of memory formation. *Progress in neurobiology* 126:19-35.

67. Olcese U, Iurilli G, Medini P (2013) Cellular and synaptic architecture of multisensory integration in the mouse neocortex. *Neuron* 79:579-593.
68. Ikegaya Y, Aaron G, Cossart R, Aronov D, Lampl I, Ferster D, Yuste R (2004) Synfire chains and cortical songs: temporal modules of cortical activity. *Science* 304:559-564.
69. Takahashi N, Kitamura K, Matsuo N, Mayford M, Kano M, Matsuki N, Ikegaya Y (2012) Locally synchronized synaptic inputs. *Science* 335:353-356.
70. Villette V, Malvache A, Tressard T, Dupuy N, Cossart R (2015) Internally Recurring Hippocampal Sequences as a Population Template of Spatiotemporal Information. *Neuron* 88:357-366.
71. Klausberger T, Somogyi P (2008) Neuronal diversity and temporal dynamics: the unity of hippocampal circuit operations. *Science* 321:53-57.
72. Kepecs A, Fishell G (2014) Interneuron cell types are fit to function. *Nature* 505:318-326.
73. Womelsdorf T, Valiante TA, Sahin NT, Miller KJ, Tiesinga P (2014) Dynamic circuit motifs underlying rhythmic gain control, gating and integration. *Nature neuroscience* 17:1031-1039.
74. Engel J, Jr., Thompson PM, Stern JM, Staba RJ, Bragin A, Mody I (2013) Connectomics and epilepsy. *Current opinion in neurology* 26:186-194.
75. Jia H, Rochefort NL, Chen X, Konnerth A (2010) Dendritic organization of sensory input to cortical neurons in vivo. *Nature* 464:1307-1312.
76. Marvin JS, Borghuis BG, Tian L, Cichon J, Harnett MT, Akerboom J, Gordus A, Renninger SL, Chen TW, Bargmann CI, Orger MB, Schreier ER, Demb JB, Gan WB, Hires SA, Looger LL (2013) An optimized fluorescent probe for visualizing glutamate neurotransmission. *Nature methods* 10:162-170.
77. Cichon J, Gan WB (2015) Branch-specific dendritic Ca(2+) spikes cause persistent synaptic plasticity. *Nature* 520:180-185.
78. Smith SL, Smith IT, Branco T, Hausser M (2013) Dendritic spikes enhance stimulus selectivity in cortical neurons in vivo. *Nature* 503:115-120.
79. Phillips WA (2015) Cognitive functions of intracellular mechanisms for contextual amplification. *Brain and cognition*.
80. Shai AS, Anastassiou CA, Larkum ME, Koch C (2015) Physiology of layer 5 pyramidal neurons in mouse primary visual cortex: coincidence detection through bursting. *PLoS computational biology* 11:e1004090.
81. Harvey CD, Coen P, Tank DW (2012) Choice-specific sequences in parietal cortex during a virtual-navigation decision task. *Nature* 484:62-68.
82. Hangya B, Ranade SP, Lorenc M, Kepecs A (2015) Central Cholinergic Neurons Are Rapidly Recruited by Reinforcement Feedback. *Cell* 162:1155-1168.
83. Mickoleit M, Schmid B, Weber M, Fahrbach FO, Hombach S, Reischauer S, Huisken J (2014) High-resolution reconstruction of the beating zebrafish heart. *Nature methods* 11:919-922.
84. Bouchard MB, Voleti V, Mendes CS, Lacefield C, Grueber WB, Mann RS, Bruno RM, Hillman EM (2015) Swept confocally-aligned planar excitation (SCAPE) microscopy for high speed volumetric imaging of behaving organisms. *Nature photonics* 9:113-119.
85. Andermann ML, Gilfoy NB, Goldey GJ, Sachdev RN, Wolfel M, McCormick DA, Reid RC, Levene MJ (2013) Chronic cellular imaging of entire cortical columns in awake mice using microprisms. *Neuron* 80:900-913.
86. Horton NG, Wang K, Kobat D, Clark CG, Wise FW, Schaffer CB, Xu C (2013) three-photon microscopy of subcortical structures within an intact mouse brain. *Nature photonics* 7.
87. Mittmann W, Wallace DJ, Czubyko U, Herb JT, Schaefer AT, Looger LL, Denk W, Kerr JN (2011) Two-photon calcium imaging of evoked activity from L5 somatosensory neurons in vivo. *Nature neuroscience* 14:1089-1093.
88. Wang K, Milkie DE, Saxena A, Engerer P, Misgeld T, Bronner ME, Mumm J, Betzig E (2014) Rapid adaptive optical recovery of optimal resolution over large volumes. *Nature methods* 11:625-628.

## 11 REFERENCES BY THE AUTHOR

---

### 11.1.1 Publications connected to the Thesis

1. Balázs Rózsa, Gergely Szalay, Gergely Katona. Acousto-optical Scanning-Based High-Speed 3D Two-Photon Imaging In Vivo. *Neuronomethods* 2016;113:213-245.
2. Szalay G\*, Judák L\*, Katona G\*, Ócsai K, Juhász G, Veress M, Szadai Z, Fehér A, Tompa T, Chiovini B, Maák P, Rózsa B. Fast 3D Imaging of Spine, Dendritic, and Neuronal Assemblies in Behaving Animals. *Neuron*. 2016 Nov 23;92(4):723-738. doi: 10.1016/j.neuron.2016.10.002. PubMed PMID: 27773582.
3. Szalay G, Judák L, Szadai Z, Chiovini B, Mezey D, Pálfi D, Madarász M, Ócsai K, Csikor F, Veress M, Maák P, Katona G. [Fast three-dimensional two-photon scanning methods for studying neuronal physiology on cellular and network level]. *Orv Hetil.* 2016 May 1;157(18):724. doi: 10.1556/650.2016.30457. Hungarian. PubMed PMID: 27106729.
4. Katona G\*, Szalay G\*, Maák P\*, Kaszás A\*, Veress M, Hillier D, Chiovini B, Vizi ES, Roska B, Rózsa B. Fast two-photon in vivo imaging with three-dimensional random-access scanning in large tissue volumes. *Nat Methods*. 2012 Jan 8;9(2):201-8. doi: 10.1038/nmeth.1851. PubMed PMID: 22231641.

*\* these authors contributed evenly to the publication*

### 11.1.2 Other publications

1. Deneux T, Kaszas A, Szalay G, Katona G, Lakner T, Grinvald A, Rózsa B, Vanzetta I. Accurate spike estimation from noisy calcium signals for ultrafast three-dimensional imaging of large neuronal populations in vivo. *Nat Commun*. 2016 Jul 19;7:12190. doi: 10.1038/ncomms12190. PubMed PMID: 27432255.
2. Szalay G\*, Martinecz B\*, Lénárt N, Környei Z, Orsolits B, Judák L, Császár E, Fekete R, West BL, Katona G, Rózsa B, Dénes Á. Microglia protect against brain injury and their selective elimination dysregulates neuronal network activity after stroke. *Nat Commun*. 2016 May 3;7:11499. doi: 10.1038/ncomms11499. PubMed PMID: 27139776; PubMed Central PMCID: PMC4857403.
3. Kerekes BP, Tóth K, Kaszás A, Chiovini B, Szadai Z, Szalay G, Pálfi D, Bagó A, Spitzer K, Rózsa B, Ulbert I, Wittner L. Combined two-photon imaging, electrophysiological, and anatomical investigation of the human neocortex in vitro. *Neurophotonics*. 2014 Jul;1(1):011013. doi: 10.1117/1.NPh.1.1.011013. Epub 2014 Sep 11. PubMed PMID: 26157969; PubMed Central PMCID: PMC4478968.

4. Wertz A, Trenholm S, Yonehara K, Hillier D, Raics Z, Leinweber M, Szalay G, Ghanem A, Keller G, Rózsa B, Conzelmann KK, Roska B. PRESYNAPTIC NETWORKS. Single-cell-initiated monosynaptic tracing reveals layer-specific cortical network modules. *Science*. 2015 Jul 3;349(6243):70-4. doi: 10.1126/science.aab1687. PubMed PMID: 26138975.
5. Chiovini B, Turi GF, Katona G, Kaszás A, Pálfı D, Maák P, Szalay G, Szabó MF, Szabó G, Szadai Z, Káli S, Rózsa B. Dendritic spikes induce ripples in parvalbumin interneurons during hippocampal sharp waves. *Neuron*. 2014 May 21;82(4):908-24. doi: 10.1016/j.neuron.2014.04.004. Erratum in: *Neuron*. 2014 Aug 6;83(3):749. PubMed PMID: 24853946.

## 12 ACKNOWLEDGEMENT

---

First of all I would like to thank for my scientific supervisor, Balázs Rózsa for the guidance and support through this wonderful adventure of becoming a scientist over the years. It was a fantastic opportunity to join his group and learn two-photon imaging and in vivo technology. Without his help and instructions I could not finished this work.

Many thanks go to co-authors and colleagues for their friendship, support and the amazing time we spent together, particularly Alexandra Bojdán, Attila Kaszás, Balázs Chiovini, Botond Roska, Dániel Hillier, Dénes Pálfi, Ferenc Csikor, Katalin Ócsai, Klaudia Spitzer, Linda Judák, Máté Veress, Maák Pál, Andárs Fehér, Tamás Tompa, Zoltán Szadai, Éva Jámber, Zsófi Morlin, Domonkos Pinke, Gergely Katona. Besides them I could not miss to say thank to all the college from the Two-photon laboratory in the Institute of the Experimental Medicine and from Femtonics Company for all the help and technical support.

Here I have to thank to students who dared to trust and follow to all my tiring thoughts on my views and how to improve. I was lucky to see them turn form students to college.

Last, but not least, I would like to thank my family to give me a great support by patient and tolerant for my many weeks and weekend what they have to spent without me.